Copyright

by

Samaresh Guchhait

2007

The Dissertation Committee for Samaresh Guchhait

certifies that this is the approved version of the following dissertation:

Strongly Correlated Systems: Magnetic Measurements of Magnesium Diboride and Group IV Magnetic Semiconductor Alloys

Committee:

John T. Markert, Supervisor

Sanjay K. Banerjee

Alejandro de Lozanne

Allan H. MacDonald

Michael P. Marder

Strongly Correlated Systems: Magnetic Measurements of Magnesium Diboride and Group IV Magnetic Semiconductor Alloys

by

Samaresh Guchhait, B.Sc., M.S.

Dissertation

Presented to the Faculty of the Graduate School of

The University of Texas at Austin

in Partial Fulfillment

of the Requirements

for the Degree of

Doctor of Philosophy

The University of Texas at Austin

December 2007

To them who believed I could do it even when I myself didn't.

Acknowledgments

This dissertation has been shaped by many people, including my teachers, collaborators, friends and family. This is a great opportunity to acknowledge the influence these people have had in my development as a person and as a physicist.

First and foremost, I would like to thank my advisor Prof. John T. Markert. He is an amazing advisor, a marvellous physicist, and an insightful researcher. He gave me just the right balance of freedom, encouragement, and direction to guide the course of my research. My stimulating discussions with him made the act of research an experience of pure enjoyment, and helped to pull me out of many difficult situations. Above all, he is truly a great human being. It was a great pleasure to work with him.

I am very thankful to Prof. Sanjay K. Banerjee for funding us to carry out some of the most crazy research ideas. Without his collaboration and guidance, I would not have been able to do any research on group IV magnetic semiconductor alloys. He is also very kind to offer me a position in his group. I am also grateful to Prof. Allan H. MacDonald for spending his valuable time to listen to my research ideas and also to teach me much wonderful physics.

I have been fortunate to come across several great teachers who taught me

things that added breadth to my knowledge. They include Mike Marder, Allan MacDonald, Sanjay Banerjee, Dietrich Belitz, Davison Soper, Michael Raymer, Michael Downer, Jack Swift, Takeshi Udagawa and, of course, John Markert.

I am thankful to Prof. Gan Liang of Sam Houston State University for collaborating with us on the doped MgB_2 superconductor project. I am also thankful to Prof. S. I. Lee (POSTECH, Korea) for giving us high quality MgB_2 single crystals with which to perform our experiments.

I am thankful to all members of our research group. All group members have helped me in many ways to create a collaborative research ambience in our laboratory. I am especially thankful to Dr. Jae-Hyuk Choi for teaching me the very difficult NMRFM experimental techniques. Thank you to Issac Manzanera for much really necessary and useful help. I am also thankful to Mark Monti and Rosa Cardenas for painfully proofreading my thesis and correcting my mistakes. Dr. Keeseong Park was always friendly and willing to help in anyway he could. In addition, I acknowledge with thanks the other present group members: Wei Lu, Han-Jong Chia, Theodore Cackowski and Sara Sharif.

During my graduate studies here at UT, I have met so many wonderful people. They have made my long student life a memorable learning experience. I probably won't be able to mention all of them here. Kavan Modi has taught me much quantum physics and we enjoy discussing anything. Marcus Torres has taught me how to dance like a Brazilian. Prof. Peter Antoniewicz has helped me with my teaching job. It is always a great pleasure to talk with Rafal Zgadzaj.

This acknowledgment will be incomplete without thanking our department workshop staff members. I am specially thankful to Jack Clifford, Allan Schroeder,

Lanny Sandefur, Ed Baez and Gary Thomas. Jack Clifford is probably the most acknowledged individual in all UT physics dissertations. He was always there whenever I needed any help at the machine shop.

I am very fortunate to know Dr. Nandita Chaudhuri and Prof. Bhaskar Dutta (both of them are at Texas A&M University now). They have constantly encouraged me to pursue my dreams. They have always treated me as a member of their family and that greatly helped me to overcome the pain of staying far from home. I am also very grateful to Dr. Chaudhuri for her teaching to improve my culinary skills.

My days in Austin have been made worth living because of lively interactions with a number of friends. It is hard to imagine how my student life would have been without these people. It was my great pleasure to meet Dr. Ayan Guha again here in Austin. I will always cherish the time I spent with Dr. Sagnik Dey, Subhadeep Chaudhury and Samarjit Chakraborty. I will always remember Dr. Sandip Ray for his help from the moment I came to Austin (in 2001) until today. Dr. Susanta Sarkar has constantly encouraged me to complete my graduate study soon. Others to mention are Shovan Kanjilal, Manashi Mukherjee, Dr. Sugato Basu, Shreyasee Dey, Dr. Debarshi Basu, Dr. Swaroop Ganguly, Trina Das, Dr. Joy Sarkar, Dipanjan Basu, Mustafa Jamil, Diptendu Ghosh, Arijit Das, Suranjana Das, Lincy Jacob, Sayantani Ghosh and Jacqueline Moses. In addition, my outlook on life and work has been influenced by my lifelong friends that include Dr. Satyaki Dutta, Dr. Sumit Nath, Sanchita Mitra, Dr. Partha Mitra, Prof. Saurya Das, Dr. Anirban Basu, Barun Dolui, Purnendu Mazi, Soumitra Bera, Swapan Pal, Jagadiswar Das and Suman Giri. I know that this is not a complete list and I have missed the names of many others.

Finally, I would like to thank my parents without whose patience, perseverence, and immense personal sacrifice this dissertation would not have seen the light of day. I am also fortunate to have a very loving brother (Alakes), sister (Shampa), uncle (Malaya Guchhait), aunts (Manju Guchhait and Chinmoyee Ghorai), cousins (Soumen and Mita) and all other family members. Thank you all.

Samaresh Guchhait

The University of Texas at Austin

December 2007

Strongly Correlated Systems: Magnetic Measurements of Magnesium Diboride and Group IV Magnetic Semiconductor Alloys

Publication No. _____

Samaresh Guchhait, Ph.D.

The University of Texas at Austin, 2007

Supervisor: John T. Markert

Nuclear Magnetic Resonance Force Microscopy (NMRFM) is a unique quantum microscopy technique, which combines the three-dimensional imaging capabilities of magnetic resonance imaging (MRI) with the high sensitivity and resolution of atomic force microscopy (AFM). It has potential applications in many different fields. This novel scanning probe instrument holds potential for atomic-scale resolution.

MgB_2 is a classic example of two-band superconductor. However, the behavior of these two bands below the superconducting transition temperature is not well understood yet. Also, the anisotropic relaxation times of single crystal MgB_2 have not been measured because it is not yet possible to grow large enough MgB_2 single crystals for conventional NMR. Using our homemade NMRFM probe, we have set out to measure the relaxation times of micron size MgB_2 single crystals to an-

swer several questions relating to the anisotropy, multiband behavior, and coherence effects in this unusual superconductor.

The goal of a second project is to study the effects of doping on the critical current of MgB_2 superconducting wires. Ti-sheathed MgB_2 wires doped with nano-size crystalline-SiC up to a concentration of 15 wt% SiC have been fabricated, and the effects of the SiC doping on the critical current density (J_c) and other superconducting properties studied. In contrast with the previously reported results, our measurements show that SiC doping decreases J_c over almost the whole field range from 0 to 7.3 tesla at all temperatures. Furthermore, it is found that the degradation of J_c becomes stronger at higher SiC doping levels. Our results indicate that these negative effects on J_c could be attributed to the absence of significant effective pinning centers (mainly Mg_2Si) due to the high chemical stability of the crystalline-SiC particles.

The principle goal of a third project, the study of magnetic semiconductors, is to investigate magnetic properties of Mn-implanted GeC thin films. 20 keV energy Mn ions were implanted in two samples: 1) bulk Ge (100) and 2) a 250 nm thick epitaxial GeC film, grown on a Si (100) wafer by UHV chemical vapor deposition using a mixture of germane (GeH_4) and methylgermane (CH_3GeH_3) gases. A SQUID magnetometer study shows granular ferromagnetism in both samples. While the Curie temperature for both samples is about 180 K, the in-plane saturated magnetic moment per unit area for the first sample is about 2.2×10^{-5} emu/cm^2 and that for the second sample is about 3.0×10^{-5} emu/cm^2. The external field necessary to saturate the magnetic moment is also larger for the second sample. These results show clear enhancement of magnetic properties of the Mn-implanted GeC thin film

over the identically implanted Ge layer due to the presence of a small amount of non-magnetic element carbon.

Contents

Acknowledgments **v**

Abstract **ix**

Contents **xii**

List of Figures **xvi**

I Magnetic Measurements of Magnesium Diboride **1**

Chapter 1 Overview of Magnetic Resonance Force Microscopy **2**

1.1 Nuclear Magnetic Resonance 3

1.1.1 Introduction 3

1.1.2 Theory of a Two-State Nucleus 4

1.1.3 Quantum Theory of Spin Precession in a Magnetic Field . . . 7

1.1.4 Semi-classical Theory of Nuclear Magnetic Resonance 10

1.1.5 Nuclear Spin Manipulation by RF Field 14

1.2 Nuclear Spin Relaxation Processes 15

1.2.1 Bloch Equations 15

1.2.2 Solutions of the Bloch Equations 17
1.2.3 Spin Echo and Spin-Spin Relaxation Times 19
1.2.4 Spin-Lattice Relaxation Time 22
1.3 Nuclear Magnetic Resonance Force Microscopy 24
1.3.1 Sensitivity of NMRFM 28
1.3.2 Cyclic Adiabatic Inversion 30

Chapter 2 MgB_2: A Unique Two-band Superconductor 33

2.1 A Basic Introduction to MgB_2 34
2.2 Spin-Lattice Relaxation in Superconductors 38
2.3 Spin-Lattice Relaxation in Polycrystalline MgB_2 41
2.4 ^{11}B NMR Spectrum of Single Crystal MgB_2 44

Chapter 3 Experimental Details and Results 46

3.1 Experiment Setup 47
3.1.1 Fiber Optic Interferometer 49
3.1.2 Lock-in Amplifier 52
3.1.3 Fringe Lock 53
3.1.4 Other Accessory Systems 55
3.2 Determining Cantilever Characteristics 56
3.2.1 Frequency Scan 56
3.2.2 Determining the Cantilever Spring Constant 58
3.3 NMRFM Experiment 61
3.3.1 Frequency Modulation Setup 61
3.3.2 RF Power Amplifier 62

3.3.3 Signal-to-Noise Ratio Calculation 63
3.4 Challenges of NMRFM Experiment 64
3.5 Results and Discussion 66
3.6 Future Studies 68

Chapter 4 Ti-sheathed Doped MgB_2 Superconducting Wires 69

4.1 Introduction 70
4.2 Experimental Details 71
4.3 Results and Discussion 73
4.4 Conclusions 82
4.5 Future Studies 83

II Magnetic Measurements of Group IV Magnetic Semiconductor Alloys 84

Chapter 5 Group IV Magnetic Semiconductor Alloys 85

5.1 Basic Introduction to Magnetic Semiconductors 86
5.2 Group IV Magnetic Semiconductors and Alloys 88
5.3 Experimental Details 89
5.4 Experimental Results 92
5.5 Discussion 96
5.6 Future Studies 98

Appendix A Program to Calculate 3D Magnetic Field Profile and Field Gradient 99

Appendix B C Program to Simulate 2D Image of NH_3 Molecule **106**

Bibliography **117**

Vita **122**

List of Figures

1.1 Zeeman energy levels of spin $S = 3/2$ nucleus in a uniform magnetic field $\vec{H}_0$. 5

1.2 Magnetic moment $\vec{\mu}$ precession in a uniform magnetic field along $\hat{z}$ direction. 11

1.3 Nuclear magnetic resonance (NMR) setup: a sample is placed inside a coil and a uniform magnetic field $\vec{H}_0$ is applied perpendicular to the coil axis. 11

1.4 Magnetic moment precession around the effective magnetic field $\vec{H}_{\text{eff}}$ in the rotating frame. 13

1.5 On resonance nuclear magnetic moment $\vec{\mu}$ precesses around the effective magnetic field $\vec{H}_1$ in the rotating frame. The directions of the nuclear magnetic moment at time $\tau = 0$, $\tau = \pi/2\omega_1$ and $\tau = \pi/\omega_1$ are shown. The RF pulse is on all the time. 14

1.6 Initially the saturated magnetization is along the $\hat{z}$ direction. After a $\pi/2$ pulse, the magnetization dephases in the $x'-y'$ plane with a characteristic time constant T_2^*. This happens due to inhomogeneity of the internal magnetic field. After waiting for long enough, the magnetization relaxes back to its thermal equilibrium value along the $\hat{z}$ direction, with a characteristic time constant T_1. 18

1.7 Spin-spin relaxation times: The free induction decay time constant is T_2^*, while the real magnetization decay rate time constant on the $x'-y'$ plane is T_2. 19

1.8 Initially the saturated magnetization is along the $\hat{z}$ direction. After a $\pi/2$ pulse along $\hat{x}'$ direction, it will be along the $\hat{y}'$ direction. However, it will decay due to field inhomogeneity. Another π pulse along $\hat{x}'$ after a time τ will rotate the moments in such a way that all of them will rephase along the $-\hat{y}'$ direction at time 2τ. That will give a large signal. This is known as spin echo. 20

1.9 Spin echo experiment pulse sequence schematic diagram. 20

1.10 The spin-spin relaxation time of ^{11}B nuclei in H_3BO_3 (100% concentration in water) is measured by the NMR spin echo experiment at room temperature. The measured value of spin-spin relaxation time is about 3.6 ms. 22

1.11 Pulse sequence to measure the spin-lattice relaxation time, T_1. . . . 23

1.12 The spin-lattice relaxation time of ^{11}B nuclei in H_3BO_3 (100% concentration in water) is measured by pulse NMR at room temperature. The pulse sequence used for this experiment is $\pi/2-\tau_1-\pi/2-\tau_2-\pi$, with τ_2=1 ms. The measured spin-lattice relaxation time is approximately 3.5 ms. 24

1.13 The $\vec{H}_{\text{eff}}$ field in the rotating frame. The time dependent $\hat{z}$ component is used to oscillate the nuclear spins. As the $\hat{z}$ component changes with time, $\vec{H}_{\text{eff}}$ also chages its direction. 26

1.14 The sample magnetization follows the effective field. 27

1.15 Here H_T is the total field created by the 8.067 tesla magnet and the field gradient producing magnet. All nuclei within $H_T \pm \Omega/\gamma$ field will contribute to force. 29

1.16 The magnetic moment precesses around the effective magnetic field. 31

1.17 The probability that spins will be locked after a rotation by an angle π is plotted against the quantity $(\gamma H_1)^2/\Omega\omega_{\text{osc}}$. This shows that the probability saturates when the value of that ration reaches about 10. After that P_π remains almost constant. The saturation below $P_\pi = 1$ may be due to magnetic field inhomogeneities [MM05]. 31

2.1 a. Crystal structure and b. π and σ bands of MgB_2. The orange atoms are Mg atoms and blue atoms are B atoms. The direction of c-axis is also shown. In the band structure, the σ band has brown color and π band has green color [CC03]. 35

2.2 Fermi energy levels of π and σ bands of MgB_2. The green section of columns on four corners are Fermi surface of σ band and red tunnel with caves is the Fermi surface of π electrons [CC03]. 35

2.3 The electronic part of specific heat data for MgB_2 [CC03]. The data shows clear deviation from one band BCS theory predicted curve (red curve). 36

2.4 Upper critical field anisotropy of MgB_2. The red lines are data from polycrystalline sample. The green and black lines are data from two different single crystals. The inset shows anisotropy ration, $\gamma = H_{C2}^{\perp c}/H_{C2}^{\parallel c}$, from each of these three data sets [CC03]. 37

2.5 Electronic density of states $\rho(E)$ in normal and superconducting states. In the superconducting state, an energy gap (Δ) opens up at E_F and two peaks appear on either side of E_F. 39

2.6 Superconductor energy gap (Δ) as a function of temperature. 40

2.7 The coherence peak of a superconductor. The dotted line is for normal state. 41

2.8 The spin-lattice relaxation time of polycrystalline MgB_2 is plotted as a function of temperature. There is no coherence peak below T_c. T^3 slope below T_c is expected for d-wave superconductor. The data shows relaxation times for two different applied magnetic fields [KIK+01]. . 42

2.9 ^{11}B NMR spectrum of the MgB_2 single crystal at 81 K ($H \perp c$) showing a dipolarly split central line and two satellite lines asymmetric in shape. [SRM+07]. 44

3.1 My NMRFM experiment setup. 47

3.2 SEM image of one cantilever used for NMRFM experiment. 48

3.3 Magnetic field created by a 2 micron radius, 180 nm thick cylindrical permalloy magnet. The second plot shows contours of constant magnetic field lines. The axis of this cylinder is along the z direction. This data is calculated by a C program that is given in Appendix A. Then the data is plotted by using Matlab. 50

3.4 Fiber optic interferometer and related circuits. 51

3.5 A picture of my probe. 54

3.6 Frequency scan of a cantilever with a MgB_2 crystal. Blue line is the measured signal and red line is the best fit curve. From the Lorentzian fitting we get the resonance frequency 721 Hz and the quality factor about 450. Pressure inside the probe: less than 1 millitorr and frequency step size: 0.5 Hz. 57

3.7 An example of RMS noise amplitude, power spectrum and corresponding integrated power spectrum of a cantilever at room temperature. The lock-in time constant is set at 3 second and the reference frequency increment step is 0.1 Hz between different time series [Mil03]. 60

3.8 The RF frequency modulation scheme is shown here. τ_{CAdI} is the duration of Cyclic Adiabatic Inversion or frequency modulation. . . 61

3.9 NMRFM signal of ^{11}B nuclei in MgB_2 sample. 67

4.1 XRD patterns for the core materials of the Ti-sheathed, SiC doped MgB_2 wires. For comparison, XRD patters of three reference compounds, SiC powder, MgB_2 powder and Ti powder, are shown [LFL$^+$07]. 72

4.2 (a) TEM imag of the powder of the 20 nm SiC-doped MgB_2 core with a doping level of 10 wt%. (b) The magnified bottom portion of image in (a). (c)-(e) The EDS spectra taken sites of the sample [LFL+07]. 73

4.3 SEM images of the cores of the Ti-sheathed MgB_2 wires which are (a) undoped, (b) doped with 5 wt% SiC, (c) doped with 10 wt% SiC and (d) doped with 15 wt% SiC. The surfaces of the cores were polished before taking the images. These SEM images show that a large number of holes/voids exist in the cores of the wires [LFL+07]. 76

4.4 Hysteresis of undoped and doped MgB_2 wires, measured by a vibrating sample magnetometer. This data is used to calculate J_c using the Bean model. Inset of (c): this data only was taken using a SQUID magnetometer [LFL+07]. 77

4.5 The field dependent magnetic J_c curves measured at temperatures of 5, 20 and 30 K for the undoped and SiC-doped MgB_2 wires [LFL+07]. 79

4.6 Temperature dependent dc magnetization, measured in both ZFC and FC modes in a field of 20 Oe and between 5 and 50 K, for the Ti-sheathed $MgB_2(SiC)_y$ wires. In the figure, only the sections of the curves in the temperature range between 15 and 40 K are shown. The inset shows the temperature dependent electrical resistivity curves in a temperature range between 33 and 42 K. The $T_{c,on}$ determined from these $\rho(T)$ curves is 35.9 K for all of three samples, which matches well with the values determined from the $M(T)$ curves [LFL+07]. . . 81

5.1 (Ga,Mn)As crystal structure: substitutional Mn_{Ga} and interstitial Mn_I in GaAs lattice [JSM+06]. 87

5.2 This is x-ray diffraction rocking curve of 200 nm GeC thin film, grown on Si (100) substrate. The S peak is from the substrate and the L peak is from the GeC layer. Source: Mustafa Jamil. 90

5.3 In plane saturated magnetization of Mn implanted Ge and GeC at different temperatures. Applied magnetic field is 1000 Gauss. 93

5.4 In plane magnetism of Mn implanted Ge and GeC (250 nm thick). . 94

5.5 Out of plane magnetism of Mn implanted Ge and GeC (250 nm thick). 94

5.6 In plane hysteresis of Mn implanted GeC (250 nm thick) at different temperatures. 95

5.7 In plane field-cooled and zero-field-cooled magnetization for Mn implanted GeC (250 nm thick) in a 500 gauss magnetic field. 95

A.1 The cylindrical magnetic tip and its coordinates. 100

B.1 The 2D force amplitude profile of a planer NH_3 molecule for three different sample-magnet distances. Here we are using a iron-tipped carbon nanotube as gradient-field-producing magnet. The force amplitude profile data is calculated by this program and then plotted by Matlab. Here I have assumed the magnet-on-cantilever NMRFM setup and we are scanning the cantilever to measure force amplitude at different points. It is also assumed that all three hydrogen atoms of NH_3 molecule lie on the same plane. 107

Part I

Magnetic Measurements of Magnesium Diboride

Chapter 1

Overview of Magnetic Resonance Force Microscopy

The important thing in science is not so much to obtain new facts as to discover new ways of thinking about them.

– Sir William Bragg (1862 - 1942)

Nuclear Magnetic Resonance Force Microscopy (NMRFM) is a unique quantum microscopy technique, which combines the three-dimensional imaging capabilities of magnetic resonance imaging (MRI) with the high sensitivity and resolution of atomic force microscopy (AFM). This chapter gives a basic overview of essential materials, including the theories of Nuclear Magnetic Resonance (NMR) and Magnetic Resonance Force Microscopy (MRFM). First, I will discuss general two-state systems. Then I will discuss NMR and NMRFM. Details of the experiment and our Nuclear Magnetic Resonance Force Microscope are given in following chapters.

1.1 Nuclear Magnetic Resonance

1.1.1 Introduction

The phenomenon of nuclear magnetic resonance is observed in magnetic systems with nuclei that possess magnetic dipole moments and, correspondingly, angular momentum. The term resonance implies that an externally applied RF field is in tune with the natural gyroscopic precession frequency of the magnetic moment in an external static magnetic field. Magnetic resonance frequencies fall typically within the radio frequency region of the electromagnetic spectrum. Magnetic resonance is one of the most accurate forms of atomic scale spectroscopy. It also provides information about magnetic susceptibility, magnetic moment, etc., for different nuclei.

In general, a nucleus may contain several protons and neutrons. For a given state, if the total angular momentum of a nucleus is $\vec{J}$ and it possesses a magnetic moment $\vec{\mu}$, then

$$\vec{\mu} = \gamma \, \vec{J}, \tag{1.1}$$

where the scalar γ is the "gyromagnetic ratio" of that nucleus [Sak00]. In quantum theory, both $\vec{J}$ and $\vec{\mu}$ are treated as vector operators. Now, let's define a dimensionless angular momentum $\vec{S}$ as

$$\vec{J} = \hbar \, \vec{S}, \tag{1.2}$$

where $\hbar = h/2\pi$ and h is Plank's constant. This angular momentum $\vec{S}$ is called the spin of the nucleus. Hence, we get

$$\vec{\mu} = \gamma \, \hbar \, \vec{S}. \tag{1.3}$$

1.1.2 Theory of a Two-State Nucleus

A detailed quantum mechanical description of a two-state atom/nucleus is given in all basic quantum mechanics books [Boh01, Sch68, Sak00]. Here I will give a very basic description of a two-state nucleus.

The interaction energy E of a magnetic moment $\vec{\mu}$ in an external magnetic field $\vec{H}$ is

$$E = -\vec{\mu} \cdot \vec{H}. \tag{1.4}$$

The Hamiltonian ($\mathcal{H}_e$) of an electron (with magnetic moment $|\vec{\mu}_e| = e\hbar/2m_e\,c$) in an external magnetic field $\vec{H}$ is

$$\mathcal{H}_e = -\vec{\mu}_e \cdot \vec{H} = -\frac{e\,\hbar}{m_e\,c}\,\vec{S}_e \cdot \vec{H}, \tag{1.5}$$

where e (-4.8×10^{-10} esu) is the electron charge, m_e is the mass of the electron, c is the speed of light, and $\vec{S}_e$ is the electron spin. Similarly, the Hamiltonian of any nucleus in an external magnetic field is

$$\mathcal{H} = -\vec{\mu} \cdot \vec{H} = -\frac{g_N\,e\,\hbar}{m\,c}\,\vec{S} \cdot \vec{H}, \tag{1.6}$$

where m is the mass of a nucleon (proton mass $= 1.673 \times 10^{-27}$ kg), e ($+4.8 \times 10^{-10}$ esu) is the proton charge, g_N is the *g-factor* of a nucleus and $\vec{S}$ is the nuclear spin. Here we define the nuclear g-factor (g_N) by analogy to the Landé g factor for an atom [Sch70]. For the most part, it is an experimental parameter characterizing the nuclear moment, since in most cases, nuclear theory is only able to provide a rough estimate of its magnitude. The energy of this Hamiltonian is

$$E = -\frac{g_N\,e\,\hbar}{m\,c}\,S_z\,H_0, \tag{1.7}$$

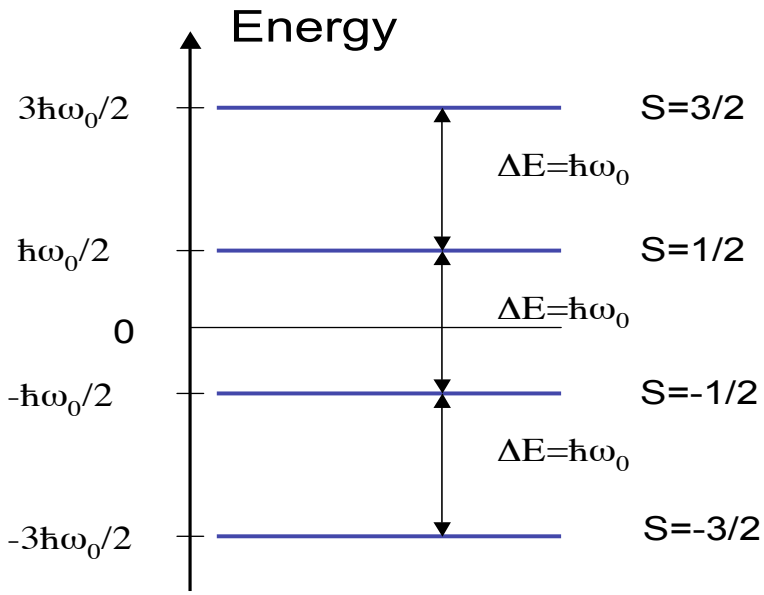

Figure 1.1: Zeeman energy levels of spin $S = 3/2$ nucleus in a uniform magnetic field $\vec{H}_0$.

where $\vec{H} = H_0\,\hat{z}$. The eigenvalues of this Hamiltonian are easy to calculate since $S_z = (S, S-1, ..., -S)$. We can calculate the allowed energies (E) from the spin, S, of the nucleus. These are called Zeeman energy levels (Fig. 1.1). For an $S = 1/2$ nucleus, there will be two energy levels, corresponding to $S_z = \pm 1/2$. So for $S = 1/2$ nucleus, we get

$$E_{\pm} = \mp \frac{g_N\, e\, \hbar\, H_0}{2\, m\, c}. \tag{1.8}$$

In general, a nucleus of spin S will have $2S+1$ equally spaced Zeeman energy levels.

We can measure these energy levels by performing absorption experiments. All we need is a time dependent interaction with an angular frequency ω_0 such that

$$\Delta E = \hbar\, \omega_0, \tag{1.9}$$

where ΔE is the difference between final and initial nuclear Zeeman energies. For

nuclear magnetic resonance, we apply an alternating magnetic field of amplitude H_x perpendicular to the static field. Then the time dependent perturbing Hamiltonian is written as

$$\hat{\mathcal{H}}_{\text{pert}} = -\,\gamma\,\hbar\,H_x\,\hat{S}_x\,\cos\,\omega_0\,t. \tag{1.10}$$

The operator $\hat{S}_x$ has matrix elements between states S_z and $S_z^{'}$ and $\langle S_z^{'}|\hat{S}_x|S_z\rangle$ vanishes unless $S_z^{'} = S_z \pm 1$. This condition allows transitions between adjacent levels only. Now by comparing Eqs. 1.7 and 1.9, we can write

$$\omega_0 \equiv \frac{g_N\,e\,H_0}{m\,c}. \tag{1.11}$$

Also by comparing Eqs. 1.3 and 1.6, the gyromagnetic ratio of any nucleus can be expressed as

$$\gamma = \frac{g_N\,e}{m\,c}. \tag{1.12}$$

Now by combining Eqs. 1.11 and 1.12 we get the very well known expression:

$$\omega_0 = \gamma\,H_0. \tag{1.13}$$

For $H_0 = 8.07$ T, and ^{11}B nucleus ($\gamma/2\pi = 13.66$ MHz/T), the angular frequency ($\omega_0/2\pi$) is about 110.23 MHz. This is also known as the Larmor frequency.

When we apply a radio frequency field, a nucleus in the ground state makes a transition to the excited state if the frequency of the RF field matches the Larmor frequency. For a spin 1/2 system, this means a transition from $S_z = -1/2$ to $S_z = 1/2$ state. However, the nucleus will not stay in the excited state for long and it will quickly decay to the ground state. This gives rise to nuclear relaxation, which I will talk more about later.

1.1.3 Quantum Theory of Spin Precession in a Magnetic Field

Let us assume there is a uniform magnetic field $\vec{H} = H_0\,\hat{z}$. For spin 1/2 systems, we can define the spin $S_z = \pm 1/2$ states as $|\pm\rangle$ base kets. We can express all three spin $\hat{\vec{S}}$ coordinate operators in terms of $|\pm\rangle$ states as follows:

$$\hat{S}_x = \frac{1}{2}\,(|+\rangle\langle-| \;+\; |-\rangle\langle+|), \tag{1.14a}$$

$$\hat{S}_y = \frac{i}{2}\,(|-\rangle\langle+| \;-\; |+\rangle\langle-|), \tag{1.14b}$$

$$\hat{S}_z = \frac{1}{2}\,(|+\rangle\langle+| \;-\; |-\rangle\langle-|). \tag{1.14c}$$

Defined in this way, they obey the *fundamental commutation relations of angular momentum*, $[\hat{S}_i,\,\hat{S}_j] = i\,\varepsilon_{ijk}\,\hat{S}_k$. The normalized eigenstates for $\hat{S}_x$, $\hat{S}_y$ and $\hat{S}_z$ operators are

$$|S_x\pm\rangle = (|+\rangle \;\pm\; |-\rangle)/\sqrt{2}, \tag{1.15a}$$

$$|S_y\pm\rangle = (|+\rangle \;\pm\; i\,|-\rangle)/\sqrt{2}, \tag{1.15b}$$

$$|S_z\pm\rangle = |\pm\rangle, \tag{1.15c}$$

respectively. Now we can write the nuclear spin Hamiltonian operator $\hat{\mathcal{H}}$ (Eq. 1.6) in the following way

$$\hat{\mathcal{H}} = \hbar\,\omega_0\,\hat{S}_z, \tag{1.16}$$

where $\omega_0 = \gamma\,H_0$. The corresponding unitary time evolution operator is

$$\hat{\mathcal{U}}(t, t_0 = 0) = \exp\left(\frac{-i\,\hat{\mathcal{H}}\,t}{\hbar}\right) = \exp\left(-i\,\omega_0\,\hat{S}_z\,t\right). \tag{1.17}$$

Let us assume that at $t_0 = 0$, the initial state of the system $\alpha(t)$ is

$$|\alpha(t_0 = 0)\rangle = c_+\,|+\rangle \;+\; c_-\,|-\rangle, \tag{1.18}$$

where $|c_\pm|^2$ is the probability of $\pm$ states respectively and the orthonormalization condition gives $|c_+|^2 + |c_-|^2 = 1$. The state of the system at any later time t is given by

$$\begin{aligned} |\alpha(t)\rangle &= \hat{\mathcal{U}}(t, t_0 = 0)\, |\alpha(t_0 = 0)\rangle \\ &= c_+\, e^{-i\,\omega_0\, t/2}\, |+\rangle \;+\; c_-\, e^{i\,\omega_0\, t/2}\, |-\rangle. \end{aligned} \tag{1.19}$$

The appearance of $\omega_0 t/2$ is very interesting. It means that after a 2π rotation, the nucleus picks up an overall phase of π or a negative sign. The nucleus returns back to its original state only after a 4π rotation. If the nucleus is initially in a spin up state, then $c_+ = 1$ and $c_- = 0$. The time evolution operator does not do anything to this state. The nucleus will remain in the spin up state for all time. The same is true if the initial state is a spin down state. These are called **stationary states**. However, if the initial state of the nucleus is $|\alpha(t_0 = 0)\rangle = |S_x+\rangle = \frac{1}{\sqrt{2}}\,|+\rangle + \frac{1}{\sqrt{2}}\,|-\rangle$, then after time t, the state of the nucleus will be

$$\begin{aligned} |\alpha(t)\rangle &= \frac{1}{\sqrt{2}}\, e^{-i\,\omega_0\, t/2}\, |+\rangle \;+\; \frac{1}{\sqrt{2}}\, e^{i\,\omega_0\, t/2}\, |-\rangle \\ &= \cos\omega_0\, t/2\; |S_x+\rangle + i\, \sin\omega_0\, t/2\; |S_x-\rangle. \end{aligned} \tag{1.20}$$

Unlike the previous cases, here the state of the nucleus (Eq. 1.20) changes with time. One can see that by calculating the probability of finding the nucleus in either of the states $|S_x\pm\rangle$, after time t. The probabilities of finding the nucleus in the states $|S_x\pm\rangle$ are

$$|\langle S_x + |\, \alpha(t)\rangle|^2 = \cos^2\omega_0\, t/2 \tag{1.21a}$$

$$\text{and } |\langle S_x - |\, \alpha(t)\rangle|^2 = \sin^2\omega_0\, t/2, \tag{1.21b}$$

respectively. Clearly, at any general time the nucleus is in a superposition state of $|S_x+\rangle$ and $|S_x-\rangle$. Even though the nuclear spin is initially in the positive x-

direction, the magnetic field in the z-direction causes it to rotate. As a result, there is a finite probability of finding the system in the negative x-direction at some other time. For this reason these are called the *superposition states* or **non-stationary states**.

Now we will study how the expectation value of an observable changes with time. We know the expectation value of any operator $\hat{\mathcal{O}}$ at some other time t is given by

$$\begin{aligned}
\langle \hat{\mathcal{O}}(t) \rangle &= \langle \alpha(t) | \, \hat{\mathcal{O}} \, | \alpha(t) \rangle \\
&= \langle \alpha(t_0 = 0) | \, \mathcal{U}^\dagger(t, t_0 = 0) \; \hat{\mathcal{O}} \; \mathcal{U}(t, t_0 = 0) \; | \alpha(t_0 = 0) \rangle \\
&= \langle \alpha(t_0 = 0) | \; \exp(i \, \omega_0 \, \hat{S}_z^\dagger \, t) \; \hat{\mathcal{O}} \; \exp(-i \, \omega_0 \, \hat{S}_z \, t) \; | \alpha(t_0 = 0) \rangle. \quad (1.22)
\end{aligned}$$

Suppose initially at $t = 0$, the nucleus is at one eigenstate of an observable that commutes with the spin Hamiltonian ($\mathcal{H}$). For example, the operator $\hat{S}_z$ commutes with the spin Hamiltonian and it has two eigenstates, $|\pm\rangle$. Then two examples of such initial states are $|\alpha(t_0 = 0)\rangle = |\pm\rangle$ and these states satisfy $\hat{\mathcal{H}} \, |\pm\rangle = \pm \hbar \, \omega_0 / 2 \, |\pm\rangle$. For these initial states, $\langle \hat{S}_i(t) \rangle$ at any given time t is

$$\begin{aligned}
\langle \hat{S}_i(t) \rangle &= \langle \pm | \; \exp(\pm \, i \, \omega_0 \, t/2) \; \hat{S}_i(t_0 = 0) \; \exp(\mp \, i \, \omega_0 \, t/2) \; | \pm \rangle \\
&= \langle \pm | \; \hat{S}_i(t_0 = 0) \; | \pm \rangle. \quad (1.23)
\end{aligned}$$

Clearly, $\langle \hat{S}_i(t) \rangle$ is independent of t for all i, i.e. the expectation values of the observables do not change with time. This is quite expected as these initial states are called **stationary states**, as we have explained before.

However, the situation is more interesting for a **superposition state**. If the initial state is $|\alpha(t_0 = 0)\rangle = |S_x +\rangle = \frac{1}{\sqrt{2}} \, |+\rangle \; + \; \frac{1}{\sqrt{2}} \, |-\rangle$, then (using Eq. 1.22) the

expectation values of the observables at any time are

$$\langle \hat{S}_x(t) \rangle = \frac{1}{2} \cos \omega_0 \, t, \tag{1.24a}$$

$$\langle \hat{S}_y(t) \rangle = \frac{1}{2} \sin \omega_0 \, t, \tag{1.24b}$$

$$\text{and } \langle \hat{S}_z(t) \rangle = 0. \tag{1.24c}$$

Physically this means the nuclear spin precesses in the xy-plane with angular frequency ω_0 [Sak00]. For any given initial spin state, we can generalize the above expression and the spin state at any other time is given by

$$\langle \hat{S}_x(t) \rangle = \langle \hat{S}_x(t=0) \rangle \, \cos \omega t \; - \; \langle \hat{S}_y(t=0) \rangle \, \sin \omega t, \tag{1.25a}$$

$$\langle \hat{S}_y(t) \rangle = \langle \hat{S}_x(t=0) \rangle \, \sin \omega t \; + \; \langle \hat{S}_y(t=0) \rangle \, \cos \omega t, \tag{1.25b}$$

$$\langle \hat{S}_z(t) \rangle = \langle \hat{S}_z(t=0) \rangle. \tag{1.25c}$$

If $\langle \hat{S}_z(t=0) \rangle \neq 0$, the precessing spin forms a cone around the uniform magnetic field. This is shown in Fig. 1.2.

1.1.4 Semi-classical Theory of Nuclear Magnetic Resonance

The rate of change of nuclear angular momentum $\vec{J}$ when a nucleus of magnetic moment $\vec{\mu}$ is placed inside a magnetic field $\vec{H}$ is

$$\frac{d\vec{J}}{dt} = \vec{\mu} \times \vec{H} = \vec{J} \times (\gamma \vec{H}), \tag{1.26}$$

since $\vec{\mu} = \gamma \, \vec{J}$. This equation is true for all $\vec{H}$. However, when $\vec{H}$ is independent of time, then the angular momentum $\vec{J}$ generates a cone. Now if we go to a frame which is rotating with an instantaneous angular velocity $\vec{\Omega}_R$, the rate of change of angular momentum in that frame is given by

$$\frac{\delta \vec{J}}{\delta t} = \vec{J} \times (\gamma \vec{H} + \vec{\Omega}_R). \tag{1.27}$$

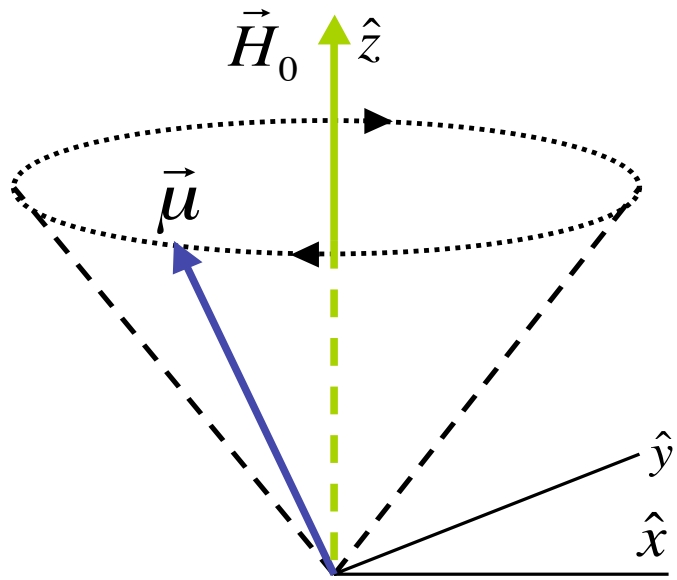

Figure 1.2: Magnetic moment $\vec{\mu}$ precession in a uniform magnetic field along $\hat{z}$ direction.

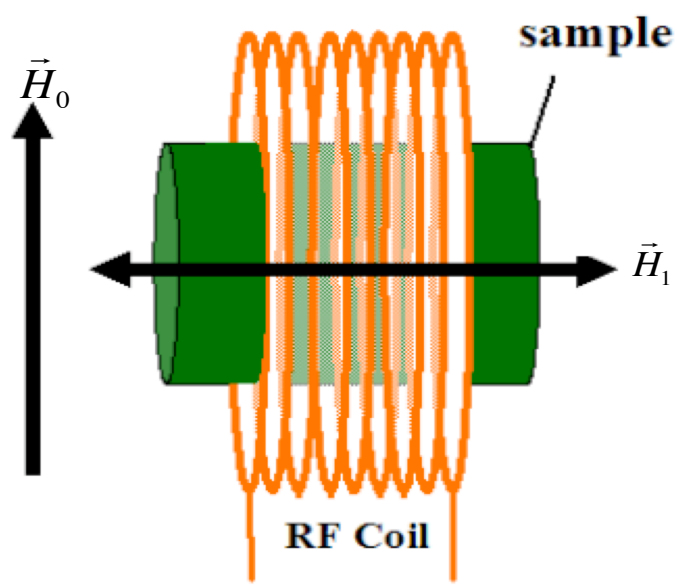

Figure 1.3: Nuclear magnetic resonance (NMR) setup: a sample is placed inside a coil and a uniform magnetic field $\vec{H}_0$ is applied perpendicular to the coil axis.

Now we can apply a time dependent magnetic field $H_x(t)\ \hat{x} = 2H_1 \cos\omega t\, \hat{x}$ by sending an alternating current through the RF coil (Fig. 1.3). This is in addition to a static magnetic field H_0 in the $\hat{z}$ direction. The total magnetic field in the static frame now is $\vec{H}(t) = H_0\, \hat{z} + H_x(t)\ \hat{x} = H_0\, \hat{z} + 2\, H_1\ \cos\omega t\ \hat{x}$, where $(\hat{x}, \hat{y}, \hat{z})$ are the unit vectors of static frame and ω is the frequency of the applied radio frequency (RF) field. The time dependent magnetic field $H_x(t)\ \hat{x}$ can be written as a superposition of two counter rotating magnetic fields as follows:

$$\vec{H}_R = H_1\ (\hat{x}\ \cos\omega t + \hat{y}\ \sin\omega t), \tag{1.28a}$$

$$\vec{H}_L = H_1\ (\hat{x}\ \cos\omega t - \hat{y}\ \sin\omega t). \tag{1.28b}$$

It is important to note that $\vec{H}_R$ and $\vec{H}_L$ are rotating with angular frequency $+\omega$ and $-\omega$ respectively. So in the static laboratory frame, the equation of motion for the nuclear angular momentum is

$$\frac{d\vec{J}}{dt} = \vec{J} \times \gamma\, [H_0\, \hat{z} + H_x(t)\, \hat{x}]. \tag{1.29}$$

Now if we go to a frame which is rotating such that $\vec{\Omega}_R = \omega\, \hat{z}$, then in that *rotating frame* Eq. 1.29 transforms into the following:

$$\frac{\delta\vec{J}}{\delta t} = \vec{J} \times [(\gamma\, H_0 + \omega)\, \hat{z} + \gamma\, H_1\, \hat{x}'], \tag{1.30}$$

where $(\hat{x}', \hat{y}', \hat{z})$ are the Cartesian unit vectors of the rotating frame. We have only taken the contribution from the $\vec{H}_R$ field to get Eq. 1.30 because this field is also rotating with same angular frequency, ω. The $\vec{H}_L$ field is rotating with an angular frequency 2ω with respect to this frame and hence, it will not contribute. However, if we go to a frame where $\vec{\Omega}_R = -\omega\, \hat{z}$, the rate of change of the nuclear angular

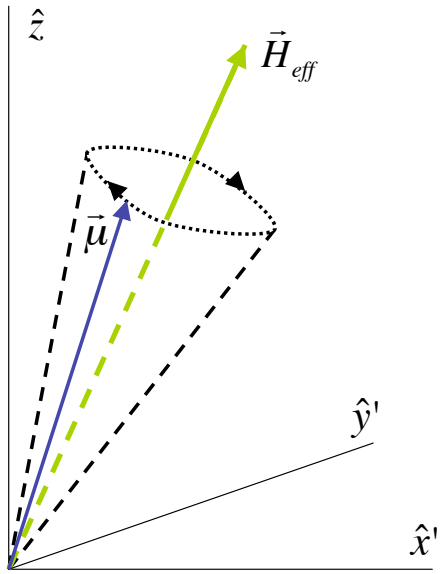

Figure 1.4: Magnetic moment precession around the effective magnetic field $\vec{H}_{\text{eff}}$ in the rotating frame.

momentum in that frame is

$$\begin{aligned}\frac{\delta \vec{J}}{\delta t} &= \vec{J} \times [(\gamma\, H_0 - \omega)\, \hat{z} + \gamma\, H_1\, \hat{x}'] \\ &= \vec{J} \times [(\omega_0 - \omega)\, \hat{z} + \gamma\, H_1\, \hat{x}'] \qquad (1.31) \\ &= \vec{J} \times \gamma\, \vec{H}_{\text{eff}}, \qquad (1.32)\end{aligned}$$

where $\omega_0 = \gamma\, H_0$ and

$$\vec{H}_{\text{eff}} = (H_0 - \omega/\gamma)\, \hat{z} + H_1\, \hat{x}'. \qquad (1.33)$$

So the rate of change of the nuclear magnetic moment in the rotating frame is

$$\frac{\delta \vec{\mu}}{\delta t} = \vec{\mu} \times \gamma\, \vec{H}_{\text{eff}}. \qquad (1.34)$$

Physically this means the nuclear magnetic moment precesses around the effective magnetic field, $\vec{H}_{\text{eff}}$ [Sli96]. This is illustrated in Fig. 1.4. However, there are two important things to notice. First, $\hat{x}'$ is fixed in the rotating frame, but rotating with

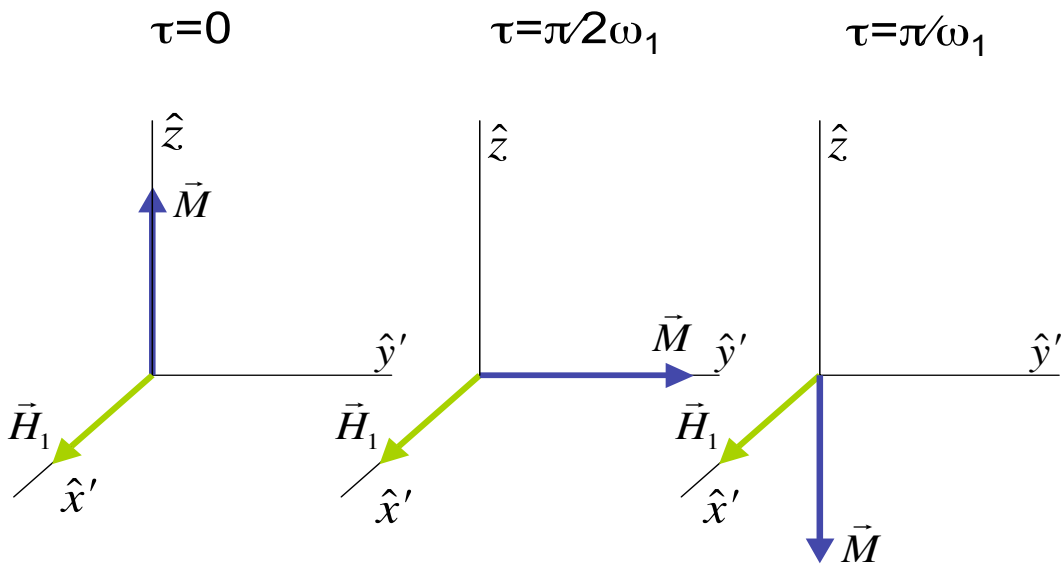

Figure 1.5: On resonance nuclear magnetic moment $\vec{\mu}$ precesses around the effective magnetic field $\vec{H}_1$ in the rotating frame. The directions of the nuclear magnetic moment at time $\tau = 0$, $\tau = \pi/2\omega_1$ and $\tau = \pi/\omega_1$ are shown. The RF pulse is on all the time.

frequency $-\omega$ in the laboratory frame. Second, the $\hat{z}$ component of the effective magnetic field depends on frequency. If $\omega = \gamma H_0 = \omega_0$, then $\vec{H}_{\text{eff}} = H_1 \hat{x}'$. We call this the magnetic resonance condition and we can control this magnetic resonance condition by changing the frequency of the applied RF magnetic field.

1.1.5 Nuclear Spin Manipulation by RF Field

In NMR, RF pulses of different durations are used to manipulate the nuclear spins. Initially, a static magnetic field $\vec{H}_0 = H_0 \hat{z}$ is applied to polarize the spins along the $\hat{z}$ direction. When an RF pulse with angular frequency $\omega_0 = \gamma H_0$ is applied perpendicular to the static magnetic field, the effective magnetic field in the rotating frame is $\vec{H}_{\text{eff}} = H_1 \hat{x}'$. As a result, the spins will precess around this effective

magnetic field $\vec{H}_{\text{eff}}$. So, if the pulse duration is τ, then the spins will rotate by an angle $\theta = \gamma\, H_1\, \tau = \omega_1\, \tau$ in the $\hat{z} - \hat{y}'$ plane.

Since the $\hat{z}$ direction is the same for both static and rotating frames, at the end of the RF pulse the spins will make an angle θ with the laboratory $\hat{z}$ axis. By carefully selecting the RF pulse length, we can rotate the spins by an angle of $\pi/2$ or π. For a $\pi/2$ rotation, the required pulse length is

$$\tau_{\pi/2} = \frac{\pi}{2\,\omega_1} = \frac{\pi}{2\,\gamma\, H_1}. \tag{1.35}$$

Similarly, we need a pulse of length $\tau_\pi = \pi/\omega_1 = 2\,\tau_{\pi/2}$ to rotate the spins by an angle π. This is shown in Fig. 1.5.

1.2 Nuclear Spin Relaxation Processes

One major application of NMR is to measure nuclear spin relaxation processes of any given sample. We measure relaxation times by manipulating nuclear spins. Based on our knowledge of spin manipulation, we now can talk about nuclear spin relaxation processes. This will help us to understand the interaction of nuclear spins with the environment, lattice and other spins.

1.2.1 Bloch Equations

When there is no applied magnetic field, then all orientations of any nuclear spin are identical. For a spin $\frac{1}{2}$ nucleus, both spin $\pm 1/2$ states have the same energy in zero field. We call this a degeneracy of spin states. However, when we apply a magnetic field $\vec{H}_0$, this degeneracy is broken. From Eq. 1.8 we know that the two spin states will now have different energies. If there is no thermal energy, all

spins will point along the applied magnetic field. At any finite temperature T, there will be a distribution of spins between these two energy levels and the ratio of the number of spins in the upper energy level to the number of spins in the lower energy level is given by

$$\exp\left(-\frac{\Delta E}{\kappa_B\, T}\right) = \exp\left(-\frac{2\,\mu\, H_0}{\kappa_B\, T}\right), \tag{1.36}$$

where κ_B is the Boltzmann constant. For an applied magnetic field of 1 tesla, this ratio is $\sim(1-10^{-6})$ at room temperature for protons. The small corresponding net (or thermal equilibrium) magnetization M_0 of the sample is given by Curie's Law:

$$M_0 = \chi\, H_0 = \frac{N\,\gamma^2\, S(S+1)\,\hbar^2}{3\,\kappa_B\, T}\, H_0, \tag{1.37}$$

where χ is the magnetic susceptibility of the sample and N is the total number of relevant atoms per unit volume. This net magnetization arises due to the small difference in the population of spins in the upper and lower energy levels.

We know when we apply a magnetic field, the spins will precess around the applied field. Now by applying an RF field, one can change the direction of spins and they can be rotated by any angle. So the sample magnetization $\vec{M}(t)$ can also change with time. The rates of change of the three components of magnetization with time are given by

$$\frac{dM_x}{dt} = \gamma\,(\vec{M}\times\vec{H})_x - \frac{M_x}{T_2}, \tag{1.38a}$$

$$\frac{dM_y}{dt} = \gamma\,(\vec{M}\times\vec{H})_y - \frac{M_y}{T_2}, \tag{1.38b}$$

$$\frac{dM_z}{dt} = \gamma\,(\vec{M}\times\vec{H})_z + \frac{M_0 - M_z}{T_1}. \tag{1.38c}$$

The convention used here is $\vec{H} = (H_x, H_y, H_0)$. Also, T_1 is called the spin-lattice relaxation time or longitudinal relaxation time and T_2 is called the spin-spin re-

laxation time or transverse relaxation time. These equations are called the **Bloch Equations**.

Viewed from the laboratory frame, the magnetization can be changing its direction continuously. However, there must be some net change of total energy of the spin system when M_z varies with time. This energy exchange takes place between spins and the lattice. Hence, the time constant of the rate of change of M_z is called the spin-lattice relaxation time. In contrast, there is no net change of total energy for changes of M_x or M_y as the static magnetic field is $H_0\,\hat{z}$. However, the magnitudes of M_x and M_y change as spins relax between themselves. So we call the time constant of the rate of change of these two transverse magnetizations the spin-spin relaxation time.

1.2.2 Solutions of the Bloch Equations

It is very hard to get a general solution of the Bloch equations. However, we can get an approximate solution of these equations for low amplitude of applied RF field. When the field $\vec{H} = (2H_1 \cos\omega t, 0, H_0)$ is applied in the laboratory frame, the rates of change of three components of the magnetization in the rotating frame are

$$\frac{dM_x}{dt} = +M_y\,(\gamma\,H_0 - \omega) - \frac{M_x}{T_2}, \tag{1.39a}$$

$$\frac{dM_y}{dt} = -M_x\,(\gamma\,H_0 - \omega) + M_z\,\gamma\,H_1 - \frac{M_y}{T_2}, \tag{1.39b}$$

$$\frac{dM_z}{dt} = -M_y\,\gamma\,H_1 + \frac{M_0 - M_z}{T_1}. \tag{1.39c}$$

We know M_x and M_y must vanish when $H_1 \to 0$. For magnetic resonance condition ($\omega = \omega_0 = \gamma H_0$) and in the very small H_1 field limit, the solutions of these Bloch

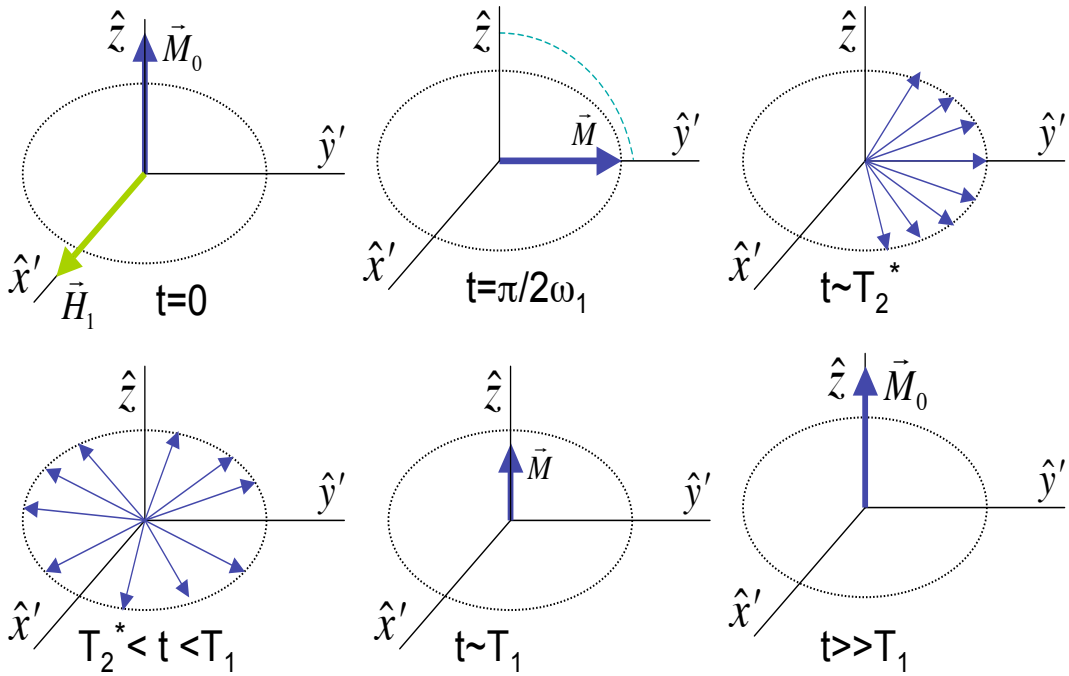

Figure 1.6: Initially the saturated magnetization is along the $\hat{z}$ direction. After a $\pi/2$ pulse, the magnetization dephases in the $x'-y'$ plane with a characteristic time constant T_2^*. This happens due to inhomogeneity of the internal magnetic field. After waiting for long enough, the magnetization relaxes back to its thermal equilibrium value along the $\hat{z}$ direction, with a characteristic time constant T_1.

equations are given by

$$M_{x,y}(t) = M_{x,y}(t=0)\, e^{-t/T_2}, \tag{1.40}$$

$$M_z(t) = M_0\,(1 - e^{-t/T_1}). \tag{1.41}$$

Using nuclear magnetic resonance one can measure these relaxation times. I will talk more about measurements of these relaxation times now.

These relaxation processes are illustrated in Fig. 1.6. After the application of the magnetic field $H_0\,\hat{z}$, there will be a net magnetization $\vec{M}_0$ along the $\hat{z}$ direction. A $\pi/2$ pulse can tilt the magnetization onto the $x'-y'$ plane. However, different

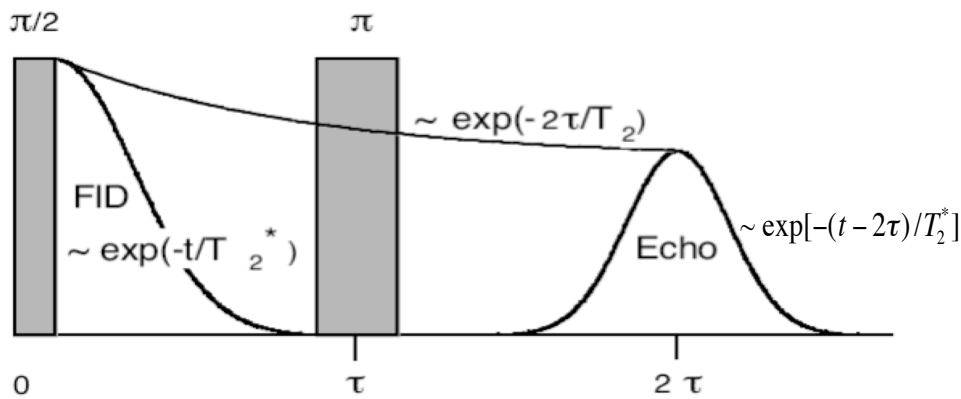

Figure 1.7: Spin-spin relaxation times: The free induction decay time constant is T_2^*, while the real magnetization decay rate time constant on the $x'-y'$ plane is T_2.

spins see different magnetic fields due to internal field inhomogeneity, so they will precess at different angular frequencies and soon they will spread out in the $x'-y'$ plane. The signal induced in the coil by the precessing spins will decay with time and we call this a free induction decay (FID). The free induction decay (FID) signal decays with a characteristic timescale T_2^*. The free induction signal decays due to two reasons: static magnetic field inhomogeneities and interactions, mainly the dipole-dipole interaction. As a result, the lineshape of the free induction decay is often broad (the decay is rapid, μs to ms). While spins dephase in the $x'-y'$ plane, a net magnetization starts to build up along the $\hat{z}$ direction. The time constant of this magnetization growth along the $\hat{z}$ is T_1. After a sufficiently long time, the spins will reach thermal equilibrium and we will get back to the equilibrium magnetization, $\vec{M}_0$ [Dra01].

1.2.3 Spin Echo and Spin-Spin Relaxation Times

A spin echo is one of the most commonly used NMR techniques. A spin echo experiment is often used to measure the magnetization at any time. It is commonly

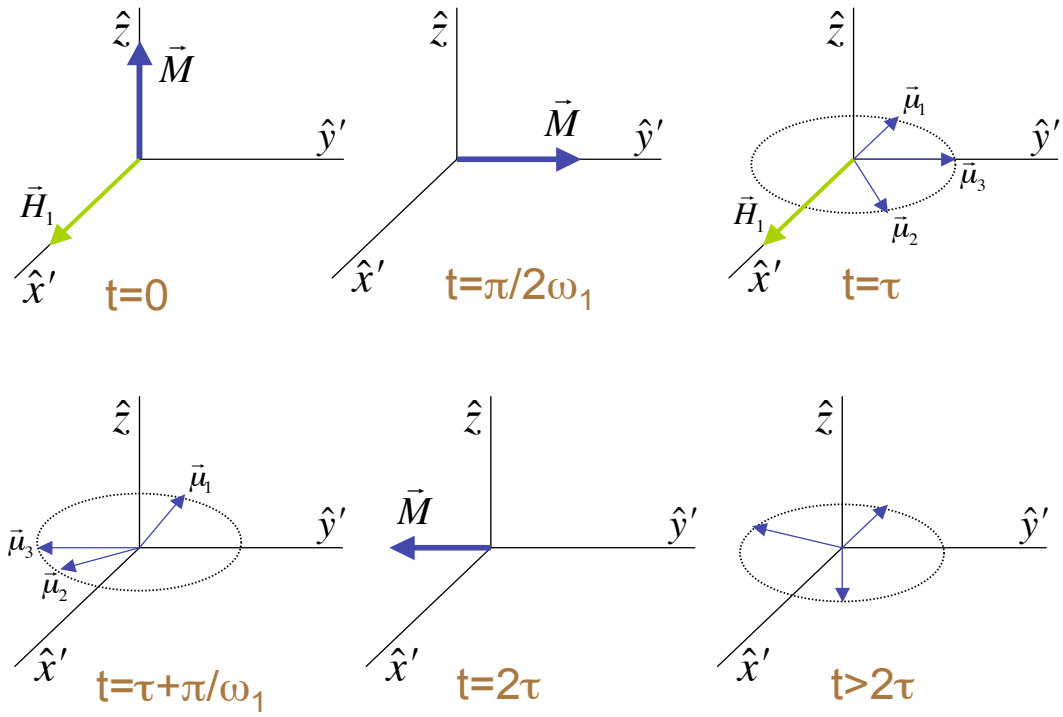

Figure 1.8: Initially the saturated magnetization is along the $\hat{z}$ direction. After a $\pi/2$ pulse along $\hat{x}'$ direction, it will be along the $\hat{y}'$ direction. However, it will decay due to field inhomogeneity. Another π pulse along $\hat{x}'$ after a time τ will rotate the moments in such a way that all of them will rephase along the $-\hat{y}'$ direction at time 2τ. That will give a large signal. This is known as spin echo.

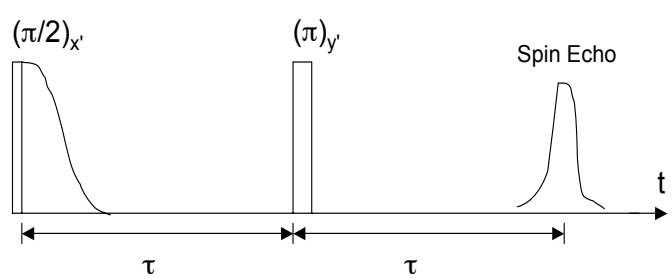

Figure 1.9: Spin echo experiment pulse sequence schematic diagram.

used to sample the magnetization in order to measure different nuclear relaxation times. I will explain the details of that experiment now.

The NMR experimental setup is described in Fig. 1.3. A $\pi/2$ RF pulse from the coil can align the sample magnetization along the y' direction on the x'–y' plane. As we have a static magnetic field $H_0\,\hat{z}$, the magnetization will precess around this field and remain in the $x'-y'$ plane. This will induce an e.m.f. in the RF coil and we can detect that to find the magnetization precession frequency. However, due to magnetic field inhomogeneity, different spins will have different precession frequencies. Also there are interactions between the nuclear spins. As a result, the signal will decay with time. This is called the free induction decay. The time constant of this decay rate is called T_2^*. So for a time $\tau > T_2^*$, the FID signal will decay to zero. However, we are often interested in the contribution to the decay that is *not* due to static field inhomogeneity, but due to interactions, typically dipole-dipole interaction. The corresponding magnetization decay time constant in the $x'-y'$ plane is T_2 (usually greater than T_2^*), which can be measured by a spin echo experiment. This is illustrated in Fig. 1.7.

At a time τ after the $\pi/2$ pulse, if we apply a π pulse along the x' direction, the spins will precess around this field. Only the y' component of the magnetic moment will rotate by an angle π. So if initially a spin was in the y' direction, after the π pulse, it will point in the $-y'$ direction. Spins precessing faster than that one are flipped so they are now behind, and spins precessing slower are now ahead. As a result, at time τ after the π pulse all of the spins will point along the $-y'$ direction and we will get a negative peak. This process is illustrated in the Fig. 1.8. Now by changing this delay time τ and using Eq. 1.40, we can find the magnetization decay

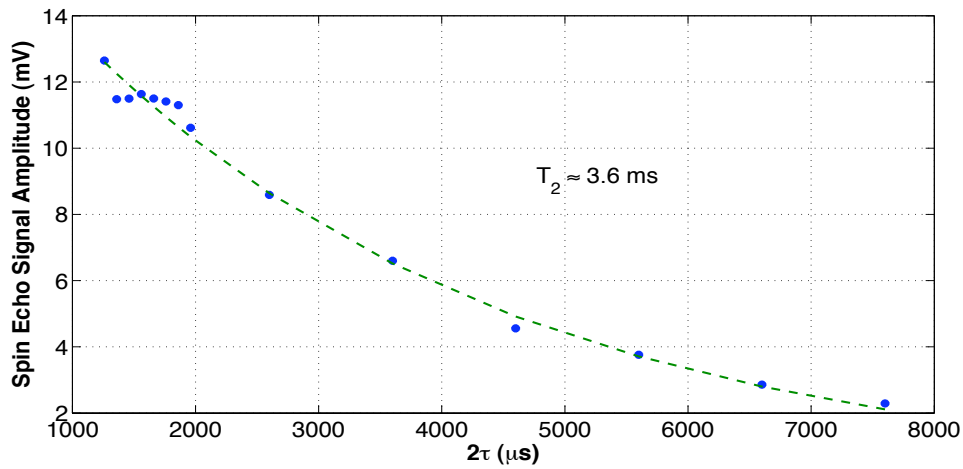

Figure 1.10: The spin-spin relaxation time of ^{11}B nuclei in H_3BO_3 (100% concentration in water) is measured by the NMR spin echo experiment at room temperature. The measured value of spin-spin relaxation time is about 3.6 ms.

time constant and it is generally longer than the FID time constant. This new time constant is called the spin-spin relaxation time or T_2. Fig. 1.9 gives a pulse sequence schematic for a positive spin echo experiment, which can be achieved when a the π pulse is applied along the y' axis. Figure 1.10 shows demonstration data that I obtained for the spin-spin relaxation time of ^{11}B in an H_3BO_3 saturated solution in water.

1.2.4 Spin-Lattice Relaxation Time

The nuclear magnetic moments build up along the applied static magnetic field through the spin-lattice relaxation process. This process was demonstrated in Fig. 1.6. So in order to destroy any initial net magnetization, we first apply a series of $\pi/2$ pulses, called saturation comb, at an interval t_s along the x' direction. At the end of the saturation comb pulse sequence, the spin orientation will be completely randomized. After that we wait for a time t and let the magnetization build

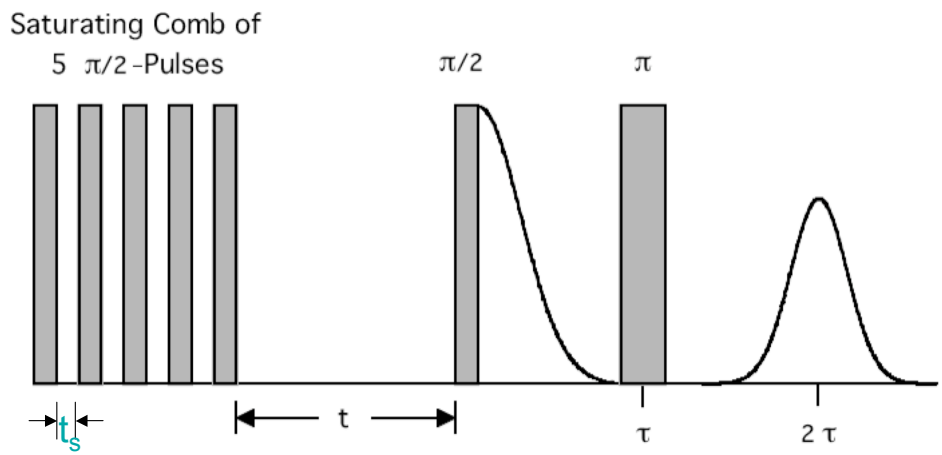

Figure 1.11: Pulse sequence to measure the spin-lattice relaxation time, T_1.

up along the $\hat{z}$ direction. This magnetization build-up process time constant is T_1. However, in order to measure the magnetization along the $\hat{z}$ direction, we need to do a spin echo experiment. We do a spin echo experiment for each t and get a series of data. All spin echo experiments are done at fixed time τ. Now we can fit the data to the Eq. 1.41 and get the spin-lattice relaxation time, T_1. This experimental pulse sequence is described in Fig. 1.11.

However, we are interested in measuring the spin-lattice relaxation time of MgB_2. For the MgB_2 sample, we will measure the spin-lattice relaxation time of ^{11}B nuclei, which have a spin $S = 3/2$. When placed within a magnetic field, there are four Zeeman energy levels for this nucleus and therefore three allowed nuclear transitions. As a result, the expression for the spin-lattice relaxation rate can be different for MgB_2 than for a spin $S = 1/2$ nuclei. For MgB_2, we expect the central transition to be most readily observed, and its spin-lattice relaxation rate can be expressed as the following:

$$\frac{M_0 - M_z(t)}{M_0} = \frac{1}{5}\,\exp\left(-\frac{t}{T_1}\right) + \frac{9}{5}\,\exp\left(-\frac{6\,t}{T_1}\right), \tag{1.42}$$

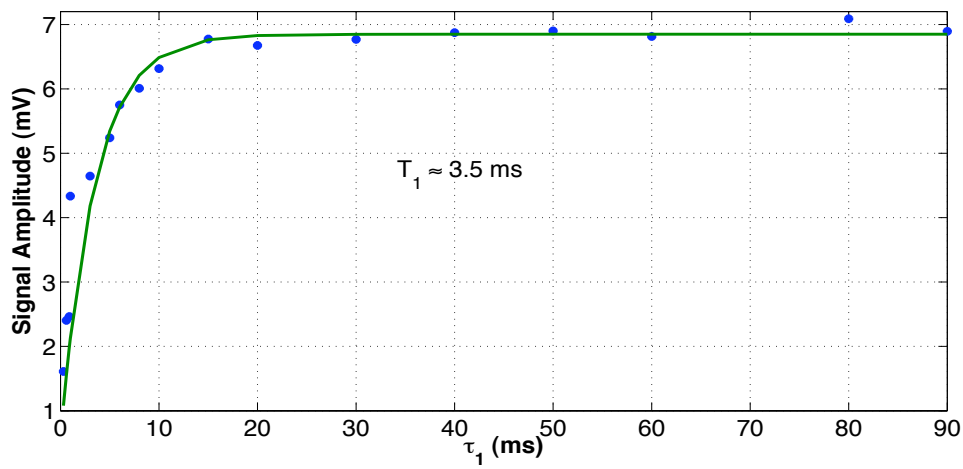

Figure 1.12: The spin-lattice relaxation time of ^{11}B nuclei in H_3BO_3 (100% concentration in water) is measured by pulse NMR at room temperature. The pulse sequence used for this experiment is $\pi/2 - \tau_1 - \pi/2 - \tau_2 - \pi$, with τ_2=1 ms. The measured spin-lattice relaxation time is approximately 3.5 ms.

where M_0 is the saturated magnetization of the sample and $M_z(t)$ is the magnetization of the sample at any given time. As described above, by doing an NMR experiment, we can measure $M_z(t)$ for different times and then fitting that data to Eq. 1.42, we can find out the spin-lattice relaxation time (T_1) of MgB_2 [SRM+07]. Figure 1.12 shows demonstration data that I obtained for ^{11}B nuclei in an H_3BO_3 saturated solution in water; for such a liquid, all three transitions contribute, and Eq. 1.41 applies.

1.3 Nuclear Magnetic Resonance Force Microscopy

In 1991, Prof. John Sidles first proposed the idea of magnetic resonance force microscopy [Sid91]. The main idea is that if a sample of magnetic moment $\vec{M}(t)$ is placed inside an external inhomogeneous magnetic field $\vec{H}$, then the force on the

sample is

$$\vec{F}(t) = (\vec{M}(t) \cdot \vec{\nabla})\, \vec{H}. \tag{1.43}$$

In the special case, when there exists a static magnetic field gradient only along the $\hat{z}$ direction, then the Eq. 1.43 can be rewritten as

$$F_z(t) = M_z(t)\, \frac{dH_z}{dz} = M_z(t)\, \frac{dH}{dz} = M_z(t)\ \nabla_z H. \tag{1.44}$$

This magnetic moment can be oscillated by frequency modulation of the RF pulse, in order to create a time dependent magnetization. The frequency of the frequency-modulated RF field is now

$$\omega(t) = \omega_0 + \Omega\, \sin \omega_m t, \tag{1.45}$$

where Ω is the amplitude of RF frequency modulation and ω_m is the angular frequency of RF frequency modulation. In the rotating frame, the effective magnetic field is

$$\vec{H}_{\text{eff}} = H_1\, \hat{x}' + (H_0 - \frac{\omega_0}{\gamma} - \frac{\Omega}{\gamma} \sin \omega_m t)\, \hat{z}. \tag{1.46}$$

On resonance, $\omega_0 = \gamma H_0$ and the effective magnetic field in the rotating frame is

$$\vec{H}_{\text{eff}} = H_1\, \hat{x}' - \frac{\Omega}{\gamma} \sin \omega_m t\ \hat{z}. \tag{1.47}$$

It is very clear from Eq. 1.47 that the $\hat{z}$ component of the effective magnetic field in the rotating frame will change periodically. The time dependence of the effective magnetic field is shown in Fig. 1.13.

We have seen that the magnetization precesses about the effective field. If the magnetization is initially *along* the effective field, and if the effective field changes direction sufficiently slowly (see Section 1.3.2), then the magnetization will follow

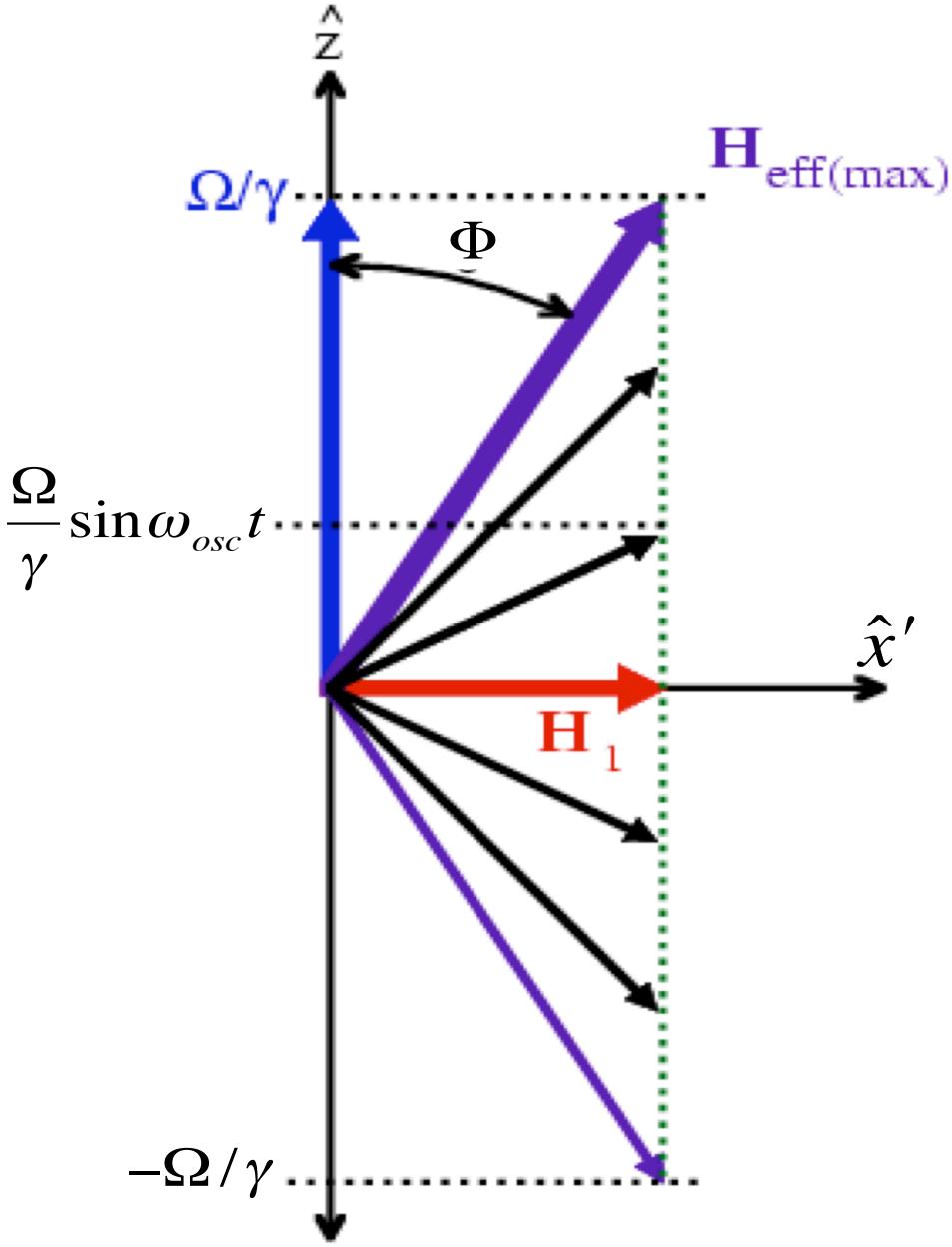

Figure 1.13: The $\vec{H}_{\mathrm{eff}}$ field in the rotating frame. The time dependent $\hat{z}$ component is used to oscillate the nuclear spins. As the $\hat{z}$ component changes with time, $\vec{H}_{\mathrm{eff}}$ also chages its direction.

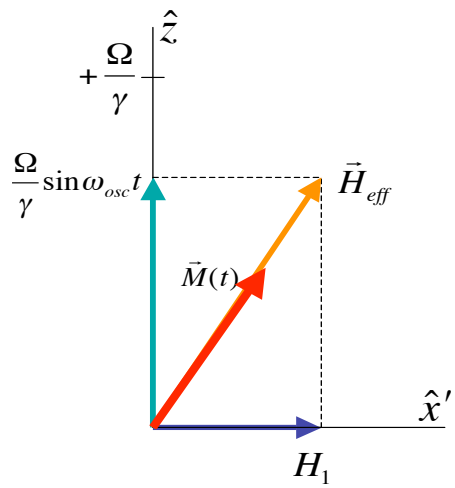

Figure 1.14: The sample magnetization follows the effective field.

the effective field. Since the magnetization follows the effective magnetic field, the z component of magnetization will change periodically with time as in the following:

$$M_z(t) = M_0 \frac{-\Omega \sin \omega_m t}{\sqrt{(\gamma H_1)^2 + (\Omega \sin \omega_m t)^2}}. \tag{1.48}$$

The sample is mounted on a micro-oscillator and will induce a time dependent force on the oscillator, and as result the oscillator will vibrate. When the frequency of the applied time-dependent force matches the resonance frequency of the oscillator, a resonance occours. On resonance, the amplitude of oscillator vibration is given by

$$A = Q \frac{F}{\kappa_{\text{osc}}}, \tag{1.49}$$

where Q is the quality factor of the oscillator, κ_{osc} is the spring constant of the oscillator and F is the amplitude of the applied force. This vibration can be measured by a fiber optic interferometer, which I will describe in detail later. This also clearly indicates that in order to get a large amplitude of oscillator vibration, the frequency of the radio frequency modulation should be the same as the resonance frequency

of the cantilever. Hence, we get $\omega_m = \omega_{\text{osc}}$. The amplitude of oscillator vibration on resonance for our experiment is typically on the order of a few nanometers.

1.3.1 Sensitivity of NMRFM

The minimum force that can be detected by NMRFM is given by

$$F_{\text{min}} = \sqrt{\frac{4\,\kappa_{\text{osc}}\,\kappa_B\,T\,\Delta\nu}{\omega_{\text{osc}}\,Q}}, \tag{1.50}$$

where $\Delta\nu$ is the "equivalent noise bandwidth" of the measurements, and ω_{osc} is the resonance frequency of the oscillator. This is calculated by equating the force necessary to create RMS thermal noise at a given temperature T. The minimum detectable force decreases with temperature. The magnetic force on the sample can be calculated from the Curie-Weiss Law. This is given as

$$F_{\text{mag}} = M_z \nabla_z H = n\,A\,\Delta z\;\frac{\gamma^2\hbar^2 I(I+1)}{3\,\kappa_B\,T} H_0\;\nabla_z H. \tag{1.51}$$

It is clear from the above equation that the magnetic force increases as we decrease the temperature, in direct proportion to the inverse of absolute temperature.

The signal-to-noise ratio (SNR) for the experiment is given by

$$\frac{F_{\text{mag}}}{F_{\text{min}}} = n\,A\,\Delta z\;\frac{\gamma^2\hbar^2 I(I+1)\sqrt{\omega_{\text{osc}}\,Q}}{6\sqrt{\kappa_{\text{osc}}\,\kappa_B^3\,T^3\,\Delta\nu}}\;H_0\,\nabla_z H. \tag{1.52}$$

Clearly the signal-to-noise ratio (SNR) will improve significantly as we lower the temperature. Also the oscillator quality factor Q and spring constant κ_{osc} play crucial roles in determining the signal-to-noise ratio for an NMRFM experiment.

Another parameter of the above equation is Δz, the width of the resonance slice. We know that only the nuclei in resonance with the applied RF field will contribute to the force on the sample. However, here we are changing the frequency

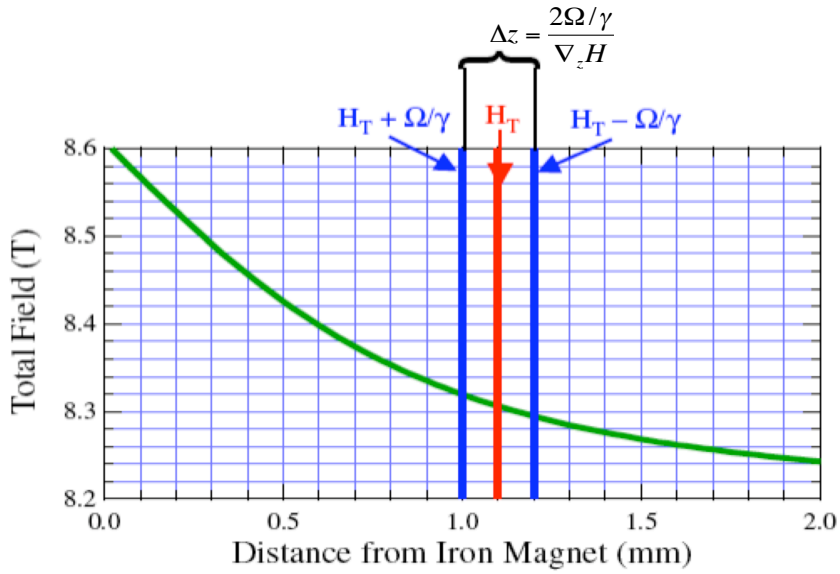

Figure 1.15: Here H_T is the total field created by the 8.067 tesla magnet and the field gradient producing magnet. All nuclei within $H_T \pm \Omega/\gamma$ field will contribute to force.

of the RF field. As a result there will be a range of magnetic fields which will be more or less in resonance with the applied RF field. All nuclei which see magnetic fields between $H_T \pm \Omega/\gamma$ will be close to resonance with the applied field and hence will contribute to the magnetic force. The physical thickness over which this field changes is shown in Fig. 1.15. This width is called the resonance slice and is given by

$$\Delta z = \frac{2\Omega/\gamma}{\nabla_z H}. \tag{1.53}$$

Clearly the width of the resonance slice will decrease as the field gradient increases. However, if Δz is very small, then we will get contribution from very few nuclei. So ideally we need to select a Δz that gives a decent signal-to-noise ratio. For my experiment, the amplitude of radio frequency modulation is 50 kHz and the magnetic

field gradient is about 200 T/m. This gives a width of the resonance slice of about 30 μm. However, my sample is about 10 microns thick. So the effective resonance slice thickness is only 10 microns for my experiment. However, if the sample thickness is bigger than the resonance slice width, then we get $\Delta z \cdot \nabla_z H = 2\Omega/\gamma$. For this condition, the NMRFM signal-to-noise ratio (Eq. 1.52) is independent of the magnetic field gradient and the resonance slice width.

1.3.2 Cyclic Adiabatic Inversion

The magnetization precesses around the effective magnetic field, as shown in Fig. 1.16. The cone is exaggerated to highlight the precession of individual spins; ideally, the net magnetization is parallel to the effective field. The effective magnetic field also changes its direction with time. However, in order to effectively lock the magnetization around the effective magnetic field, the precession frequency of the magnetization, γH_{eff}, must be much greater than the rate of change of Φ, the angle that $\vec{H}_{\text{eff}}$ makes with the $\hat{z}$ direction. Thus, the condition for adiabatic following is that the direction of $\vec{H}_{\text{eff}}$ must not change appreciably in one precession period. It is important to note that γH_{eff} is at its minimum when $\vec{H}_{\text{eff}}$ is pointing along the $\hat{x}'$ direction and also $d\Phi/dt$ has its highest value there. So the following condition needs to be satisfied to lock the magnetization around the effective magnetic field in the rotating frame:

$$\left.\frac{d\Phi}{dt}\right|_{\text{max}} \ll \gamma\, H_{\text{eff}}|_{\text{min}}\,. \tag{1.54}$$

It is easy to calculate that $d\Phi/dt|_{\text{max}} = \Omega\,\omega_{\text{osc}}/\gamma\, H_1$ and $\gamma\, H_{\text{eff}}|_{\text{min}} = \gamma\, H_1$. So combining these two we get the following condition:

$$\frac{(\gamma\, H_1)^2}{\Omega\,\omega_{\text{osc}}} \gg 1. \tag{1.55}$$

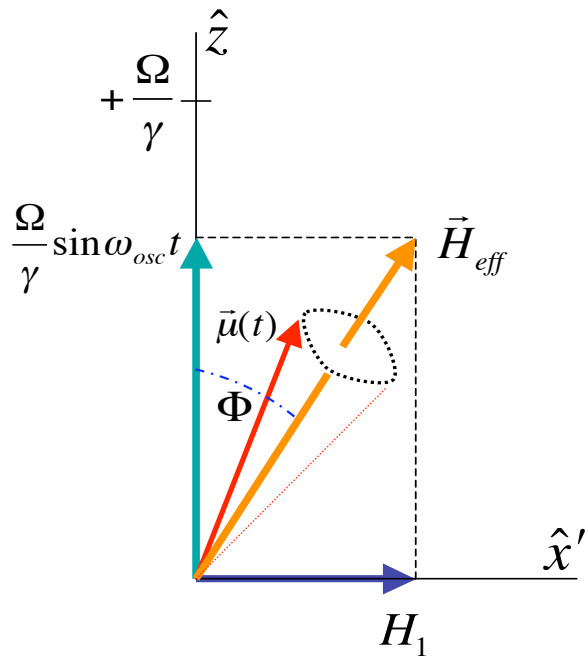

Figure 1.16: The magnetic moment precesses around the effective magnetic field.

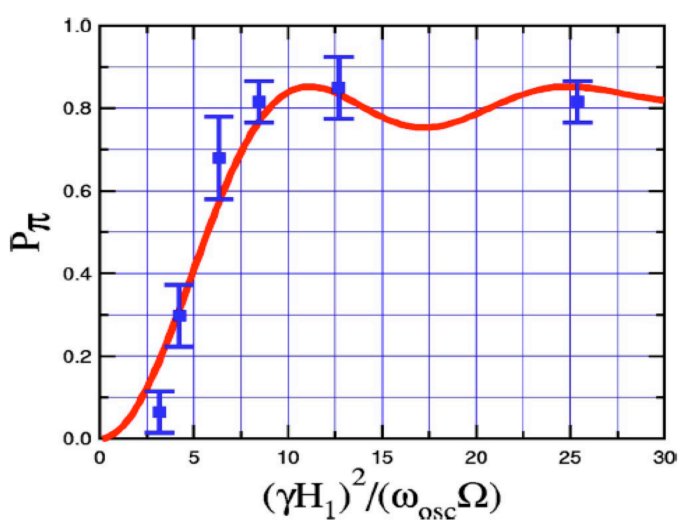

Figure 1.17: The probability that spins will be locked after a rotation by an angle π is plotted against the quantity $(\gamma H_1)^2/\Omega\omega_{\rm osc}$. This shows that the probability saturates when the value of that ration reaches about 10. After that P_π remains almost constant. The saturation below $P_\pi = 1$ may be due to magnetic field inhomogeneities [MM05].

This is called the Cyclic Adiabatic Inversion Condition. Unless we satisfy this condition, the spins will not be locked effectively around the effective magnetic field and they will be lost as we modulate the effective magnetic field.

Experiments that are performed in our laboratory show that if the ratio $(\gamma\, H_1)^2/\Omega\, \omega_{\text{osc}}$ is very small, then the probability that spins will be locked with the effective magnetic field after a rotation of an angle π is also very small. Only when the ratio has a value of about 10 or more, will the probability reach the highest value [MM05, Mil03]. This result is shown in Fig. 1.17. The saturation of the probability below $P_\pi = 1$ represents the loss of some spin following, due to inhomogeneity and edge-of-resonance-slice effects. The cyclic adiabatic inversion condition is a very important constraint that we need to consider during our experiment and make sure it is well satisfied. Otherwise, the signal-to-noise ratio will be very small and it will be hard to detect any NMRFM signal.

Chapter 2

MgB_2: A Unique Two-band Superconductor

It doesn't matter how beautiful your theory is, it doesn't matter how smart you are. If it doesn't agree with experiment, it's wrong.

– Richard P. Feynman (1918 - 1988)

MgB_2 is a classic example of a two-band superconductor. In this chapter I will briefly discuss the properties of this unique superconductor. The superconductivity of MgB_2 was discovered in Japan by a group of scientists in 2001 [NNM$^+$01]. Since then there has been a huge amount of research activity on this unusual superconductor.

The main intriguing feature of this superconductor is that it has a superconducting transition temperature of about 39 K. This is an unusually high transition temperature for an ordinary BCS type superconductor. Further research has re-

vealed that it is a Type-II, s-wave, BCS superconductor. But the most interesting thing about MgB_2 is that there are two superconducting bands: π and σ bands. These two bands have different electron-phonon coupling strengths and may become superconducting at different transition temperatures [CC03]. Among these two bands, the σ band has a stronger electron-phonon coupling than the π band.

From the BCS theory we know that

$$\kappa_{\mathrm{B}}\, T_c = 1.13\, \hbar\, \omega_{\mathrm{D}}\, \exp\left[\frac{-1}{V\, \rho(E_{\mathrm{F}})}\right], \tag{2.1}$$

where T_c is the superconducting transition temperature, ω_{D} is the phonon Debye frequency, $\rho(E_{\mathrm{F}})$ is the electron density of states at the Fermi level and V is the strength of the electron-phonon coupling. It is clear from Eq. 2.1 that as the electron-phonon coupling strength V increases, the superconducting transition temperature T_c will also increase. It is now widely believed that the reason for the unusually high T_c for MgB_2 is the strong electron-phonon coupling in the σ band.

2.1 A Basic Introduction to MgB_2

The MgB_2 crystal structure and the π and σ bands of boron are shown in Fig. 2.1. The unit cell of MgB_2 consists of (orange) magnesium atoms and (blue) boron atoms. The boron atoms form a hexagonal honeycomb lattice. The two superconducting bands are formed by the outer electrons of boron atoms. While the (brown) σ band is two-dimensional, the π band extends over all three dimension. Also these π electrons connect B atoms of different layers. Since π electrons connect two different layers, the electron-phonon coupling in this band is not that strong. However, the σ electrons are confined within two dimensions and that makes the electron-phonon

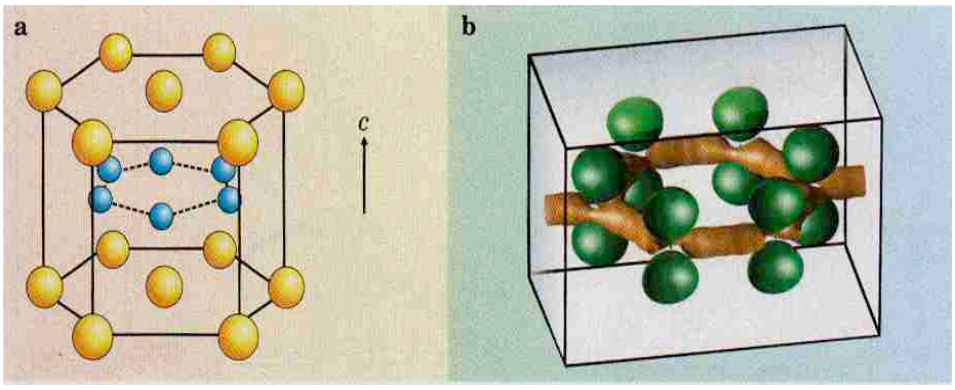

Figure 2.1: a. Crystal structure and b. π and σ bands of MgB_2. The orange atoms are Mg atoms and blue atoms are B atoms. The direction of c-axis is also shown. In the band structure, the σ band has brown color and π band has green color [CC03].

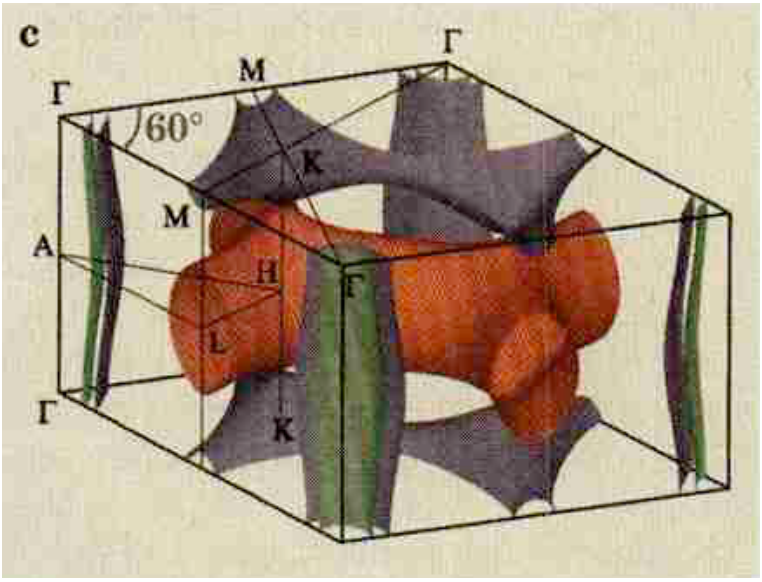

Figure 2.2: Fermi energy levels of π and σ bands of MgB_2. The green section of columns on four corners are Fermi surface of σ band and red tunnel with caves is the Fermi surface of π electrons [CC03].

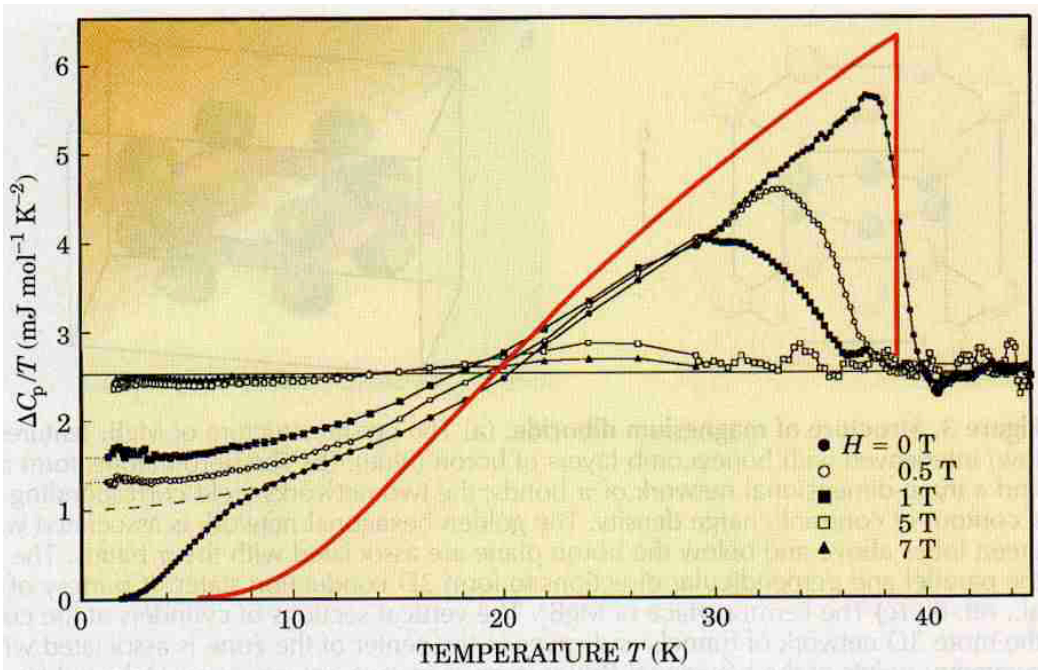

Figure 2.3: The electronic part of specific heat data for MgB_2 [CC03]. The data shows clear deviation from one band BCS theory predicted curve (red curve).

coupling in this band a lot stronger than in the π band.

The Fermi surfaces created by these two bands are shown in Fig. 2.2. The green column sections near the corners are Fermi surfaces associated with σ band electrons while the red tunnel with caves at the center is associated with π band electrons.

The electronic specific heat data shows the existence of two bands in MgB_2, shown in Fig. 2.3. The red curve is from a BCS theory calculation, considering only one band. The zero field specific heat data shows clear deviation from the one band BCS theory prediction. The deviation is especially greater at lower temperatures. Also the slope of zero field specific heat data changes at about 10 K. It is now believed that the σ band becomes superconducting just below 40 K. Then the π band

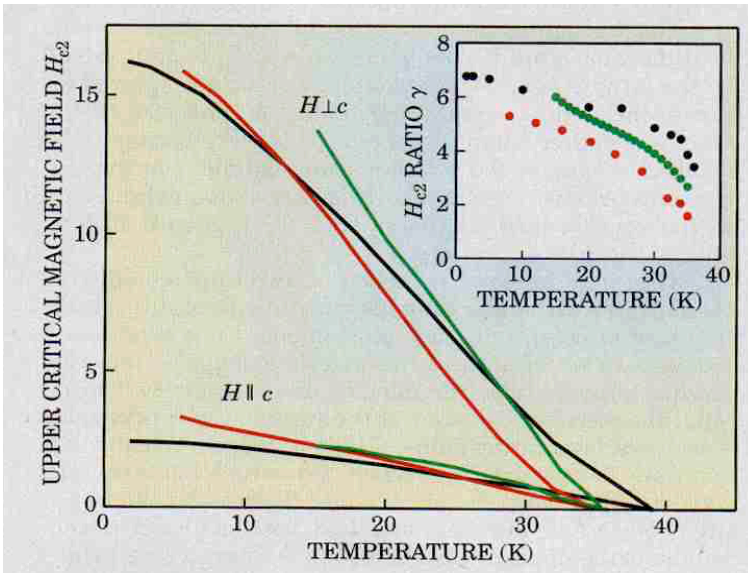

Figure 2.4: Upper critical field anisotropy of MgB_2. The red lines are data from polycrystalline sample. The green and black lines are data from two different single crystals. The inset shows anisotropy ration, $\gamma = H_{C2}^{\perp c}/H_{C2}^{\parallel c}$, from each of these three data sets [CC03].

may become superconducting at about 10 K temperature. Application of a small magnetic field of about 0.5 tesla can suppress this second superconducting transition. An externally applied magnetic field of 7 Tesla can suppress both superconducting transitions. The electronic part of the specific heat is a clear indication of the existence of two nearly separate superconducting bands in MgB_2.

Besides the electronic specific heat measurement data, tunneling experiments also show the existence of two gaps, and thus contributions from two bands. Another important aspect of MgB_2 is the upper critical field anisotropy. The upper critical field is the highest applied magnetic field below which MgB_2 remains superconducting. The upper critical field is much higher perpendicular to the c-axis than parallel to the c-axis, as shown in Fig. 2.4. It is also known from the band

structure that electrical conduction perpendicular to the c-axis is dominated by the σ band while that along the c-axis is dominated by the π band. The better σ-band conductivity corresponds to a larger in-plane coherence length. The upper critical field for $H \parallel c$ is determined by the supercurrents perpendicular to the c-axis. So the upper critical field along the c-axis ($H_{C2}^{\parallel c}$) is very small. Also, the out-of-plane coherence length is smaller due to the weaker interlayer coupling of the π bands of MgB_2. So the upper critical field perpendicular to the c-axis ($H_{C2}^{\perp c}$) is also very high.

2.2 Spin-Lattice Relaxation in Superconductors

One triumph of the BCS theory is that it could explain the origin of the coherence peak in the spin-lattice relaxation process. Before I explain the origin of the coherence peak in the superconducting state, I will explain the spin-lattice relaxation process in the normal state. The spin-lattice relaxation time can be measured by an NMR experiment.

The spin-lattice relaxation process is often dominated by the hyperfine interaction between electrons and the nucleus. The normal state spin-lattice relaxation rate ($1/T_1$) due to this interaction may be expressed as follows:

$$\frac{1}{T_1} = \frac{64}{9}\,\pi^3\,\hbar^3\,\gamma_e^2\,\gamma_n^2\,\left\langle |u_k^2(0)| \right\rangle_{E_\mathrm{F}}^2\,\rho^2(E_\mathrm{F})\,\kappa_\mathrm{B}T, \tag{2.2}$$

where $\rho(E_\mathrm{F})$ is the electron density of states at the Fermi level and u_k is the electron wavefunction. It is clear from the above equation that in the normal state $1/T_1$ decreases linearly as temperature decreases.

However, for s-wave superconductors, just below T_c a uniform energy gap

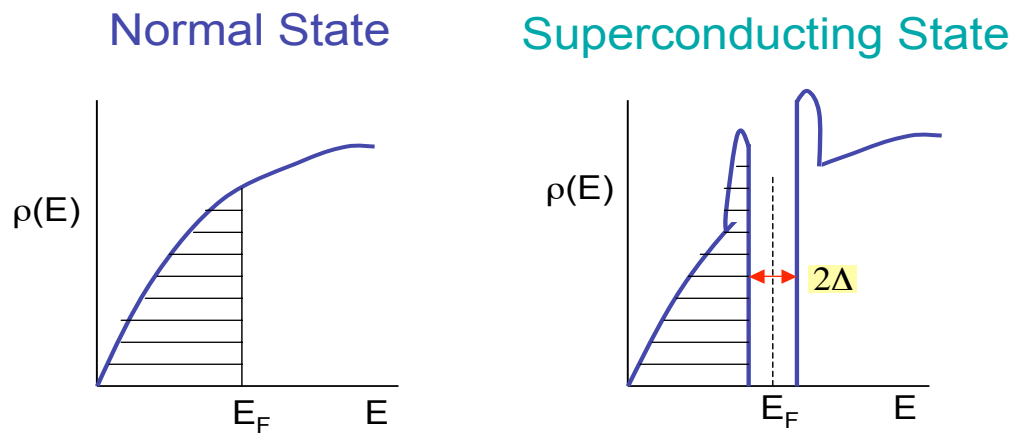

Figure 2.5: Electronic density of states $\rho(E)$ in normal and superconducting states. In the superconducting state, an energy gap (Δ) opens up at E_{F} and two peaks appear on either side of E_{F}.

opens up at E_{F} (Fig. 2.5). Since no state can exists within the energy gap, the states within that energy interval pile up on both sides of the energy gap. As a result there will be two peaks in the density of states, one on either side of the superconducting energy gap. The states below the Fermi level are filled and the states above the Fermi level are empty. So in order for nuclei to relax, they must scatter electrons from filled states below the Fermi level to empty states above the Fermi level. However, in the superconducting state the electrons have a phase coherence. As a result the scattering process will not be random. Due to this coherence effect and the peaks of the density of states on both sides of the energy gap, for most superconductors just below T_c, $1/T_1$ briefly increases rapidly as temperature decreases.

Now as temperature decreases further, the superconducting energy gap also increases [Mar00, AM01]. This is shown in Fig. 2.6. Due to this it will be exponentially harder to scatter electrons from below the energy gap to above the energy gap. Besides this, there is also less thermal excitation energy as temperature goes

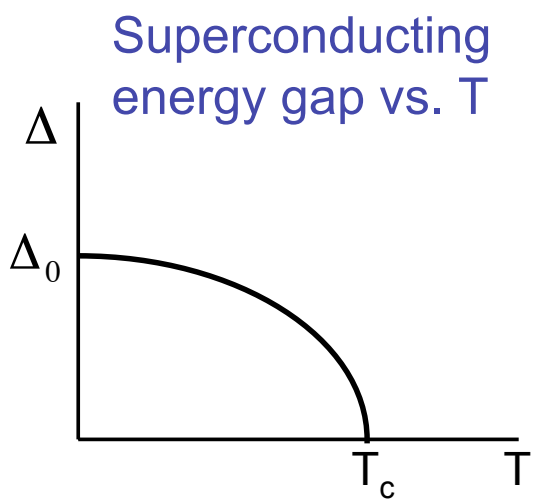

Figure 2.6: Superconductor energy gap (Δ) as a function of temperature.

down. So the combined effect of all these is that $1/T_1$ will decrease exponentially at low temperatures.

One effect of all this is a peak in $1/T_1$ versus T plot. This peak appears just below T_c and is called the coherence peak (Fig. 2.7). The reason we call it a coherence peak is that it is there because of the phase coherence of superconducting electrons [Tin96]. In the normal state, there is no phase coherence of electrons and as a result when these electrons are scattered by nuclei, there will be no coherence effects. Below T_c, the electrons go through a phase transition and due to phase coherence between electrons, there will be additional terms in the scattering processes. These terms give rise to this coherence peak. This coherence peak was first explained by the BCS theory of superconductivity and it is regarded as one the main triumphs of the BCS theory. A coherence peak has been detected in some superconductors, but none has been detected in the high-T_c copper oxide materials, many of which are believed to be d-wave superconductors.

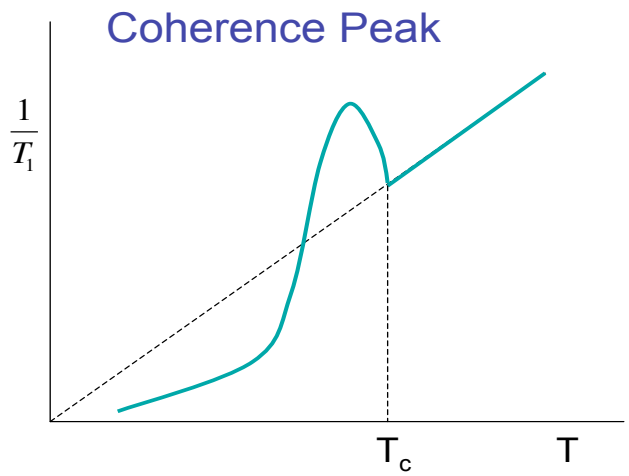

Figure 2.7: The coherence peak of a superconductor. The dotted line is for normal state.

2.3 Spin-Lattice Relaxation in Polycrystalline MgB_2

MgB_2 is a type-II, s-wave, BCS type superconductor, so we may expect to see a coherence peak in the spin-lattice relaxation data. The spin-lattice relaxation time T_1 of polycrystalline MgB_2 was measured at different temperatures by NMR. The data is shown in Fig. 2.8. The data shows no evidence of a coherence peak for both magnetic fields.

It is known that many d-wave superconductors don't exhibit any coherence peak. However, MgB_2 is not a d-wave superconductor, so our guess is that the reason for no coherence peak in this data is due to the polycrystalline nature of this MgB_2 sample. It has already been discussed that MgB_2 is a very anisotropic material, with an upper critical field which is different along the c-axis than along the direction perpendicular to it. Also, the T_c for this superconductor depends on the applied magnetic field strength and its orientation with the c-axis. The polycrystalline sample is made with many nano-size single crystals and these have

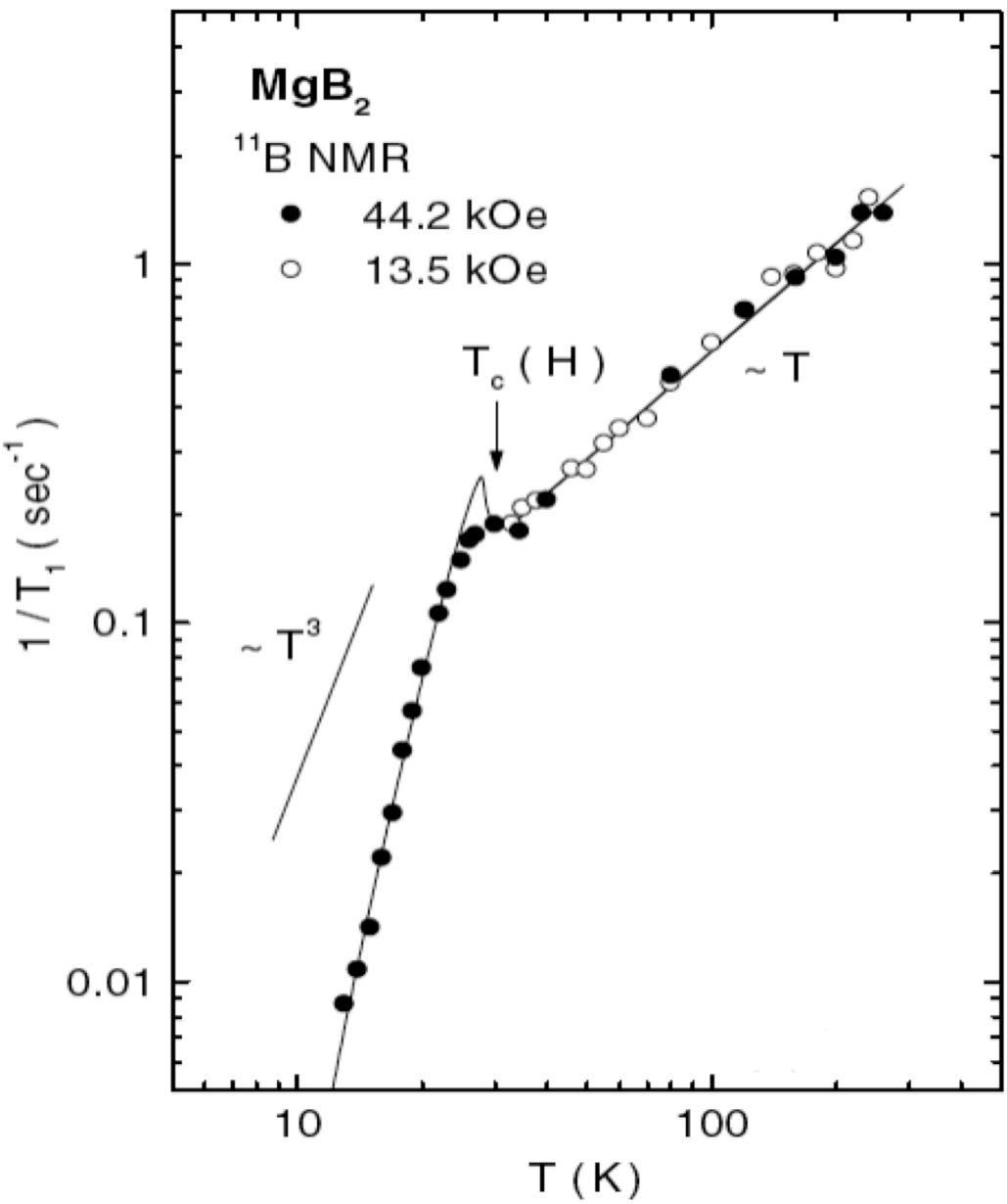

Figure 2.8: The spin-lattice relaxation time of polycrystalline MgB_2 is plotted as a function of temperature. There is no coherence peak below T_c. T^3 slope below T_c is expected for d-wave superconductor. The data shows relaxation times for two different applied magnetic fields [KIK+01].

all possible orientations with respect to the applied magnetic field. So due to this, the polycrystalline specimen will have a distribution of T_c's. That means each tiny single crystal is becoming superconducting at a different temperature as we lower the sample temperature. So even if the coherence peak exists for MgB_2, the effect will be averaged out over a large temperature range and we do not expect to detect it in a polycrystalline sample. This is one probable reason for the lack of an observation of a coherence peak in the powder MgB_2 sample.

In order to see the coherence peak for the MgB_2 superconductor, and to determine the anisotropy in this and other properties, we need to measure the spin-lattice relaxation time of a single crystal with the field along different directions. However, the problem is that MgB_2 single crystals are very small in size. The biggest high-quality samples of MgB_2 have dimensions of about 50 μm by 50 μm by 10 μm. This is a very small sample for conventional NMR. A very sensitive conventional NMR experiment can detect typically only about 10^{16} protons. For ^{11}B nuclei, the number of nuclei will be lot bigger since the gyromagnetic ratio of ^{11}B nuclei is much smaller than that of a proton. Also an NMR set-up working at this sensitivity level has many problems. As NMR is an inductive detection technique, when the RF coil becomes very small, it gets very hard to get a good signal-to-noise ratio. Very recently, one group achieved MgB_2 single crystal growth of ~ 1 mm^3, but no conventional NMR detection of ^{11}B in the superconducting state of this crystal could be achieved [SRM$^+$07].

However, it is possible to do a single crystal MgB_2 relaxation time measurement experiment with NMRFM. In fact, a single crystal of size 30 μm by 30 μm by 5 μm will give a high enough signal-to-noise ratio to measure the ^{11}B proper-

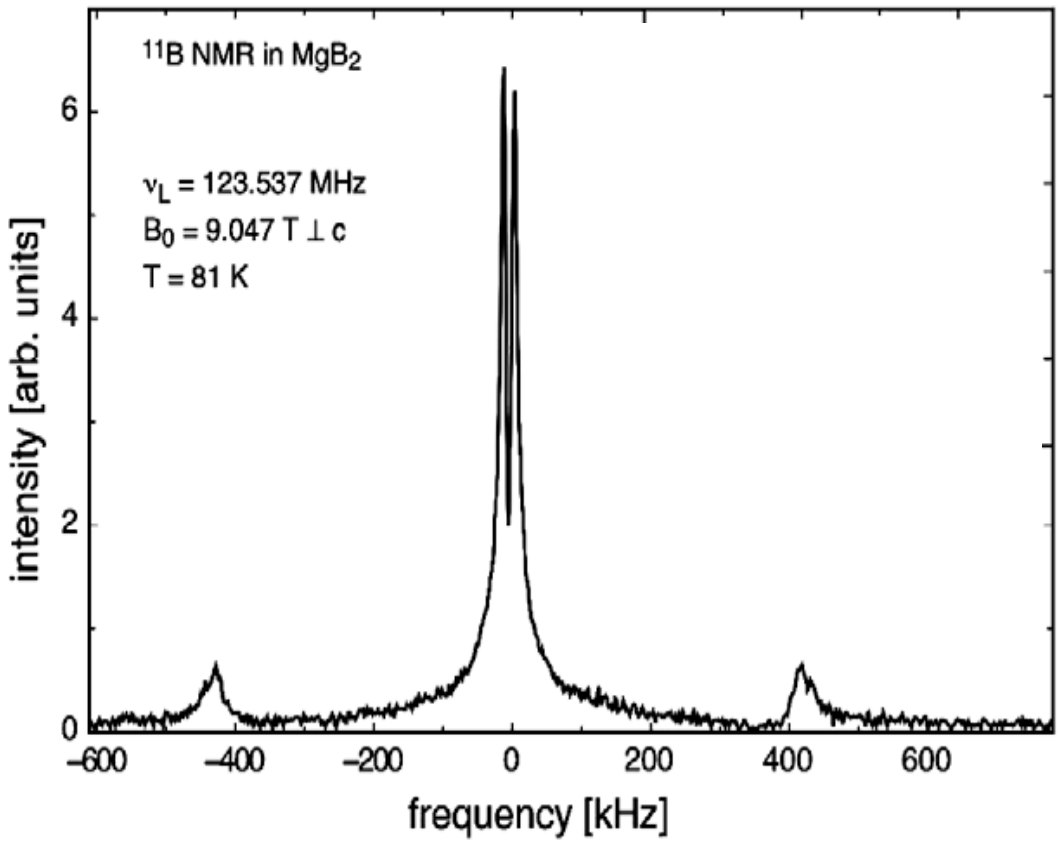

Figure 2.9: ^{11}B NMR spectrum of the MgB_2 single crystal at 81 K ($H \perp c$) showing a dipolarly split central line and two satellite lines asymmetric in shape. [SRM+07].

ties in small MgB_2 single crystals at 77 K. I will talk more about the experimental parameters required to achieve this in the next chapter.

2.4 ^{11}B NMR Spectrum of Single Crystal MgB_2

Very recently Strässle *et al.* [SRM+07] reported the measurement of the spin-lattice relaxation time of single crystal MgB_2 in the normal state. The single crystals that are used for their experiment are of size ~ 1 mm^3. However, they are unable to

measure the spin-lattice relaxation time in the superconducting state.

Figure 2.9 shows the ^{11}B conventional NMR spectrum of the MgB_2 single crystal at 81 K. The applied magnetic field (9.047 tesla) is perpendicular to the c-axis. The ^{11}B NMR spectra of MgB_2 is complex due to the simultaneous presence of first- and second-order quadrupole interactions, anisotropic magnetic shift, and nuclear dipolar coupling. The central peak exhibits a clearly visible symmetric splitting ($\approx$15.5 kHz) which is temperature independent. The full line width at half maximum (FWHM) of the central peak is $\approx$ 8 kHz and constant in the normal phase. However, it increases in the superconducting phase due to the inhomogeneity of the internal magnetic field caused by the vortex structure in the mixed state.

They also measured the anisotropy of the spin-lattice relaxation time T_1 of single crystal MgB_2 in the normal state. However, the worsening of the signal-to-noise ratio caused by the diamagnetic shielding due to the onset of superconductivity entails the need of a substantial increase of the measuring time in addition to the necessary increase due to the slow down of the nuclear spin-lattice relaxation process, which made it impossible for them to get reliable data on the spin-lattice relaxation below T_c for a single crystal MgB_2 by conventional NMR. But it is possible to measure the spin-lattice relaxation time in the superconducting state of single crystal MgB_2 by NMRFM.

Chapter 3

Experimental Details and Results

A theory is something nobody believes, except the person who made it.
An experiment is something everybody believes, except the person who made it.
– Albert Einstein (1879 - 1955)

Nuclear Magnetic Resonance Force Microscopy (NMRFM) is a novel scanned probe which holds potential for atomic-scale resolution. This technique has potential applications in many different fields. In this chapter, I will discuss various aspects and instruments used to do the NMRFM experiment. This chapter also includes details of fiber optic interferometry, signal-to-noise calculations, difficulties of the experiment, signal artifact, etc. I also will discuss the experimental results that I have obtained so far.

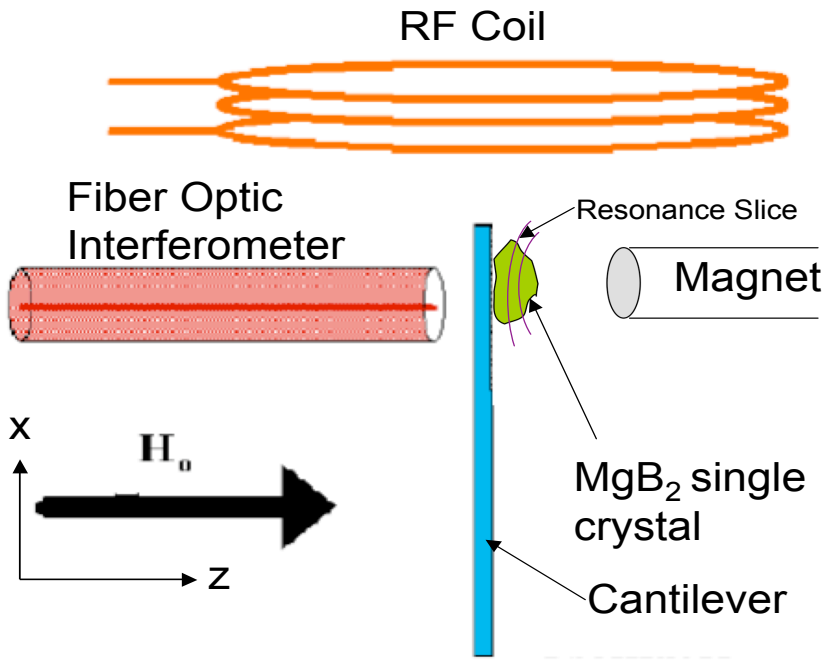

Figure 3.1: My NMRFM experiment setup.

3.1 Experiment Setup

Figure 3.1 shows my NMRFM experimental setup. A micron size MgB_2 single crystal is mounted on an ultra-floppy cantilever. The size of our samples are on the order of 40 μm by 40 μm by 5 μm and are mounted on the cantilever with silver epoxy. During sample mounting, we have to be very careful so that we don't use too much epoxy. If excess epoxy is used, then the mass of the cantilever increases to a limit where the resonance frequency will be very low, sacrificing sensitivity ($F_{\min} \propto 1/\sqrt{\omega_{\text{osc}}}$). Also, after mounting the samples, we need to bake the system at about 60°C for a few hours. We also need to be careful that epoxy chemicals don't wet the cantilever. If any chemical wets the cantilever, it will change the spring constant of the cantilever. The quality factor of the cantilever will also decrease,

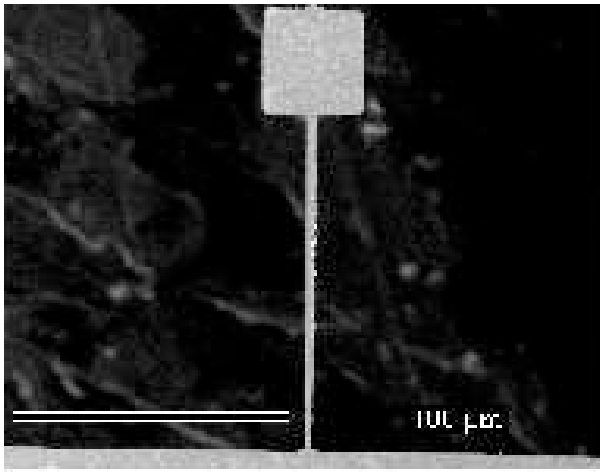

Figure 3.2: SEM image of one cantilever used for NMRFM experiment.

especially at low temperature. Besides all this, we should keep in mind that MgB_2 is an anisotropic crystal. So during the sample mounting, we need to carefully mount the sample so that c-axis of the crystal is parallel or perpendicular to the external magnetic field. For our initial experiments, we chose $H \parallel c$, since then the somewhat flat resonance slice is parallel to the crystal, improving the signal-to-noise ratio.

One of the cantilevers used for this experiment is shown in Fig. 3.2. These are about 100 μm long, with a square head at the top. The head dimension is about 20 μm by 20 μm. The cantilever arms are 5 μm wide and only a few tenths of a micron (about 300 nm) thick. The spring constant of these cantilevers is about 10^{-2} N/m, which is measured by a thermal noise scan. These cantilevers are fabricated lithographically on single crystal silicon [CMM$^+$04]. The sample is mounted on one face of the square head of the cantilever. The laser light is pointed at the opposite face of the square head of the cantilever. All cantilevers are attached to a large silicon substrate, which is in turn attached to the probe.

The entire experiment is done inside a large superconducting magnet, which

produces a uniform 8.067 tesla magnetic field. In addition to the static magnetic field $\vec{H}_0$, there is also a field-gradient-producing magnet. This is a small iron cylinder, placed very close to the sample. The total magnetic field is shown in Fig. 1.15. The total magnetic field changes over distance and this gives the spatial resolution of NMRFM. For higher spatial resolution, or a smaller resonance slice, we need a higher field gradient. Calculations show that a nanomagnet can provide enough field gradient to image a single proton. Appendix B has details of this calculation and its results. The program that I wrote to calculate the 3D magnetic field profile and field gradient is included in Apprendix A. The magnetic field created by a 2 micron radius, 180 nm long cylindrical permalloy magnet is shown in Fig. 3.3.

Another important component is the RF coil. This coil produces a radio frequency field when an alternating current flows through it. The RF coil is part of an RF tank circuit, which is tuned to have a total impedance of 50 Ω using a network analyzer. The output impedance of the RF power amplifier is matched to 50 Ω. So in order to maximize power transfer from the RF amplifier to the RF coil, the tank circuit impedance also should be close to 50 Ω.

3.1.1 Fiber Optic Interferometer

Another very important part of the NMRFM experiment is the fiber optic interferometer and related circuit, used to detect any vibration of the cantilevers. A schematic of the fiber optic interferometer is shown in Fig. 3.4. A laser diode is used as the light source. The output of the laser diode goes to a directional coupler, which rejects 90% of the laser light and only 10% of the laser light goes towards the cantilever. The reason for this is that if too much laser light hits the cantilever, then

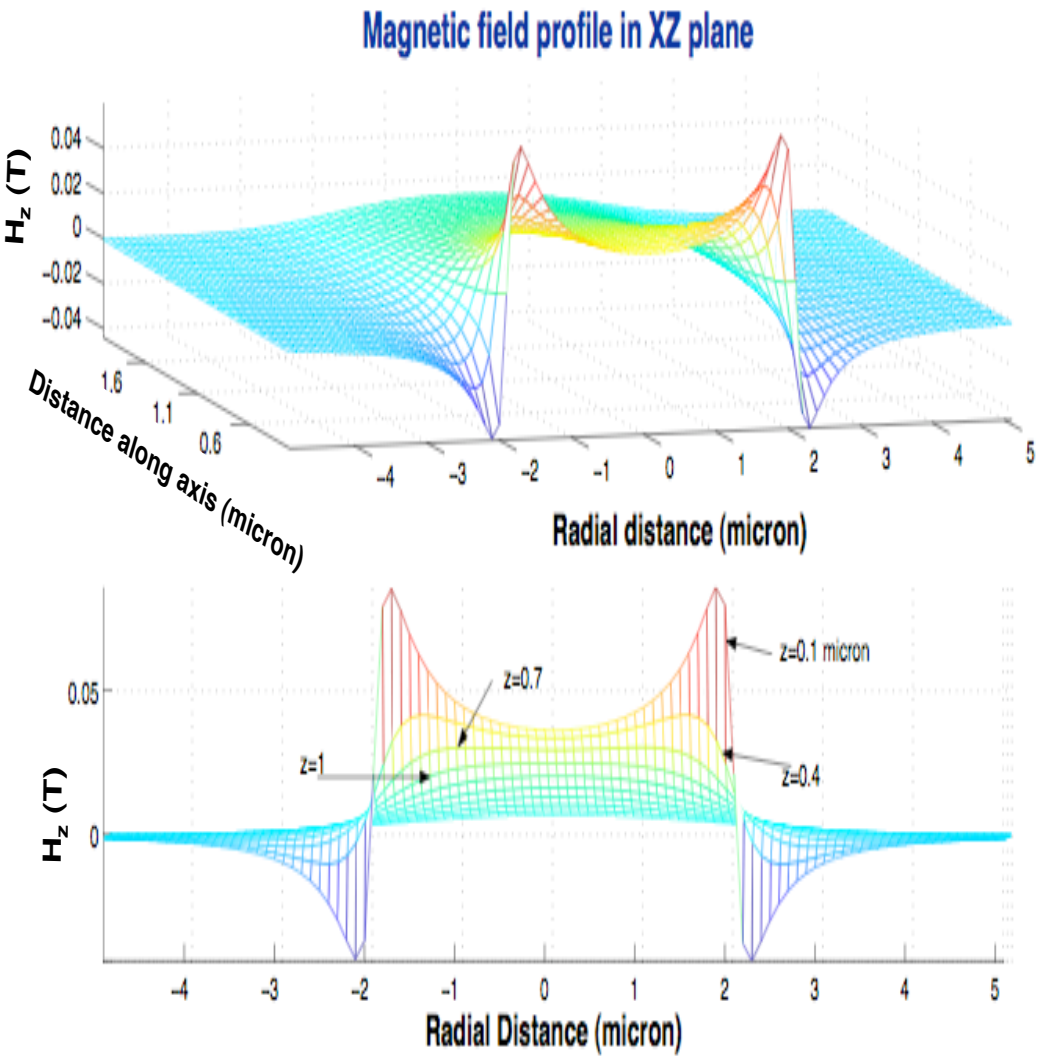

Figure 3.3: Magnetic field created by a 2 micron radius, 180 nm thick cylindrical permalloy magnet. The second plot shows contours of constant magnetic field lines. The axis of this cylinder is along the z direction. This data is calculated by a C program that is given in Appendix A. Then the data is plotted by using Matlab.

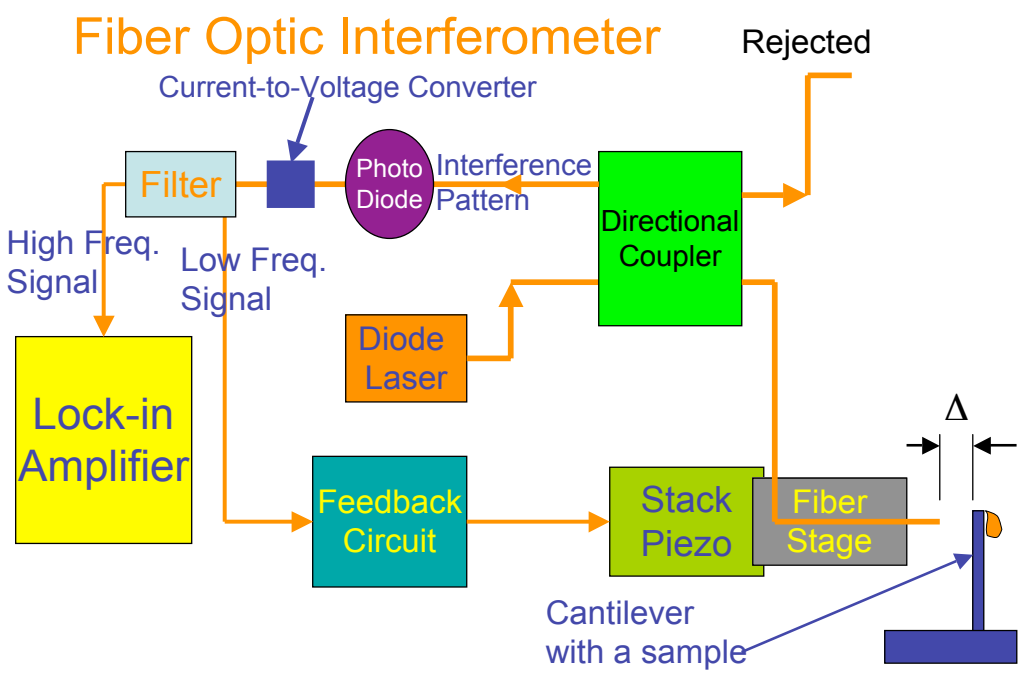

Figure 3.4: Fiber optic interferometer and related circuits.

it will heat the cantilever. Part of the light gets reflected backward from the fiber edge and the rest gets transmitted through it. Much or all of the transmitted light gets reflected by the cantilever; some of this reflected light re-enters the fiber and interferes with the light reflected from the edge of the fiber. These two rays have a path length difference of 2Δ and as a result they create an interference pattern. As the cantilever vibrates, this path length changes and hence the interference pattern also changes. This interference pattern intensity is a periodic function of the fiber-cantilever distance, with a period length that is half of the wavelength of laser diode.

The interference pattern travels through the fiber and hits a photo diode. This photo diode coverts the time dependent light intensity signal to an alternating current. As the interference pattern changes, the photo diode output current also

changes. This current in turn gets converted to a voltage and this is our signal. This signal then passes through a filter and the low-frequency part of the signal goes to a feedback circuit. This feedback circuit controls a stack piezo, which controls the movement of the fiber stage. I will discuss it below, after discussing signal processing near the mechanical oscillator frequency.

3.1.2 Lock-in Amplifier

The high-frequency part of the signal goes to a lock-in amplifier, which digitizes the signal. The lock-in amplifier is a phase sensitive device, which can determine the relative phase of different cantilever modes. The lock-in also amplifies and mixes down to near dc the Fourier components of the signal within a given bandwidth. The bandwidth ($\Delta\nu$) of the lock-in amplifier is related to its time-constant (τ_c) by the following relation: $\Delta\nu = 1/4\,\tau_c$ for the normal 6 dB/octave filter. The reference signal frequency for the lock-in is usually set to the resonance frequency of the cantilevers. The lock-in used in this experiment was a Stanford Research Systems, model SR 830 DSP lock-in amplifier.

This lock-in amplifier has two outputs. Both of these outputs go to a Nicolet model Pro30, a digital signal recorder, which records and averages these signals. This data is then analyzed to detect the NMRFM signal. The outputs of the lock-in amplifier are usually set to provide the amplitude R and the phase Θ of the signal. We also can select X and Y, the elastic and absorptive parts of the signal, respectively. The lock-in can also be controlled by a computer program. We have written a LabVIEW program to automate these steps. This lock-in amplifier was also used to determine the cantilever characteristics, which I have discussed in Section 3.2.

3.1.3 Fringe Lock

Due to various reasons, the gap between the fiber and cantilever may change. One possible reason is temperature variation. This will cause a change in the DC signal. Also there are many sources of low frequency vibrations. These low frequency noises will change the DC level and create some low frequency noise. In order to cancel these, we use the low-frequency part of the signal as an input to a feedback circuit. The details of the feedback circuit are given in C. W. Miller's Ph.D. thesis [Mil03]. The output of this feedback circuit is directly connected with a stack piezo which moves the fiber to cancel out these slow changes.

Besides damping out the low frequency noise, the feedback circuit is used to lock onto the interference pattern or fringe. It is known that if the distance between the fiber and the cantilever is changed, we will see a shift in the position on the interference pattern. In order to get the best force sensitivity, we need to lock the interference pattern at the point of maximum slope. Only then a small vibration of the cantilever will induce the largest voltage change. The absolute value of the slope is maximum at the half way between points of maximum and minimum intensity of the interference pattern. The slope at that point is given by

$$\left|\frac{dV}{dz}\right|_{\max} \simeq \frac{\pi}{2} \times \frac{4}{\lambda} \times (V_{\max} - V_{\min}), \tag{3.1}$$

where λ is the wavelength of the laser, V is the interference voltage signal, z is the distance between the fiber and the cantilever, and $V_{\max}$ and $V_{\min}$ are the maximum and the minimum intensities of the interference pattern, respectively. Using an adjustable DC power supply, we apply a DC voltage to the stack piezo to set the fringe at the point of maximum slope. Then the fringe lock feedback circuit is switched on to keep the fringe at that position.

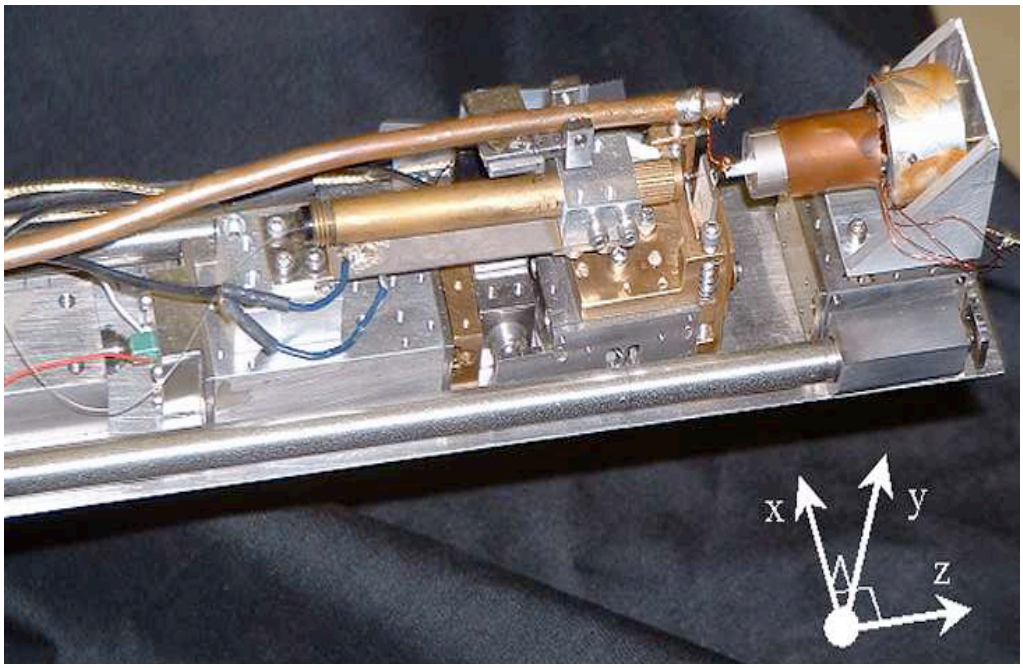

Figure 3.5: A picture of my probe.

The above equation can also be used to convert the voltage signal to a vibration amplitude of the cantilever. If the voltage difference between the highest and the lowest points of the interference pattern is V_{pp} $(= V_{\mathrm{max}} - V_{\mathrm{min}})$, then the amplitude of cantilever vibration, x, is

$$x \approx \frac{\lambda}{2\pi\, V_{\mathrm{pp}}} V, \tag{3.2}$$

where V is the signal amplitude at the resonance frequency of the cantilever. The wavelength (λ) of diode laser is 1310 nm for our experiment. The amplitude of cantilever vibration is usually a few nanometers. We have selected this diode laser to minimize the cantilever heating. The wavelength of this diode laser falls within the band-gap of silicon. As a result, (ideally) no laser light will be absorbed by the silicon-made cantilever.

3.1.4 Other Accessory Systems

Another very important component of the experiment is the large 8.067 tesla magnet. It is a Cryomagnetics, Inc. superconducting magnet, which produces a uniform magnetic field, with 1 ppm homogeneity over 1 cm^3 volume. We also have a vacuum pump to pump out the air from the probe. The air pressure inside the probe is about 10^{-5} torr. It is mainly to reduce air damping of the cantilever vibration. In normal atmospheric pressure, damping is so large that the quality factor Q of the cantilever vibration is very small. Only at very low pressures does the cantilever have a large amplitude of vibration. However, during low temperature experiments, we put a small amount (a few mTorr) of helium gas inside the probe. This helium acts as an exchange gas to conduct heat to the outer cryogen bath and maintains a low temperature within the probe.

Another very important component is the low temperature system. In order to do the NMRFM experiment, we need to cool down the probe to very low temperatures. It was shown above that the signal-to-noise ratio increases as temperature decreases, mainly due to lower thermal noise and greater magnetization at lower temperatures. MgB_2 also becomes superconducting at about 39 K. Such temperatures are attained with a dewar. We use a Janis cryostat, model SVT-200T, the tail of which is specifically designed to fit into the $3.50''$ diameter bore of our magnet and is equipped with a Lakeshore, model CX-1050 calibrated Cernox thermometer located at the bottom of the sample space. The inner space of the dewar is filled with liquid helium, while the outer space is filled with liquid nitrogen; a layer of vacuum thermally isolates each space. When the probe is placed inside a third isolated space, the central sample space of the dewar, it is surrounded by cold helium

gas to vary the temperature, or by liquid helium to reach 4 K.

In the probe there are three different stages to move the cantilever on the X-Y plane, move the magnet towards the cantilever and move the fiber towards the cantilever. All these stages are used to make very accurate alignment of fiber, cantilever and magnet. Since the cantilever head is only 20 micron wide, we need very good alignment to do this experiment. Also without proper alignment, the interference intensity will not be strong and without a strong interference intensity we will not be able to get a large voltage signal.

3.2 Determining Cantilever Characteristics

The resonance frequency and and quality factor of the cantilever first has to be determined before doing the NMRFM experiment. Also we need to find out the spring constant of the cantilever to calculate sensitivity of NMRFM experiment.

3.2.1 Frequency Scan

During the frequency scan, a sinusoidal voltage is applied for a time interval Δt from a Stanford Research System DS345 signal generator to a piezo plate on which the cantilever is mounted. A reference signal from the signal generator goes to the reference input of the lock-in amplifier. The applied voltage causes the ceramic piezo (made by American Piezo Ceramics, Inc.) to expand or contract by an amount Δh according to the formula

$$\Delta h = d_{33}\, V, \tag{3.3}$$

where d_{33} is a piezo-dependent constant equal to 2.9×10^{-10} m/V and V is the applied voltage. The silicon chip containing the cantilevers is glued to the piezo

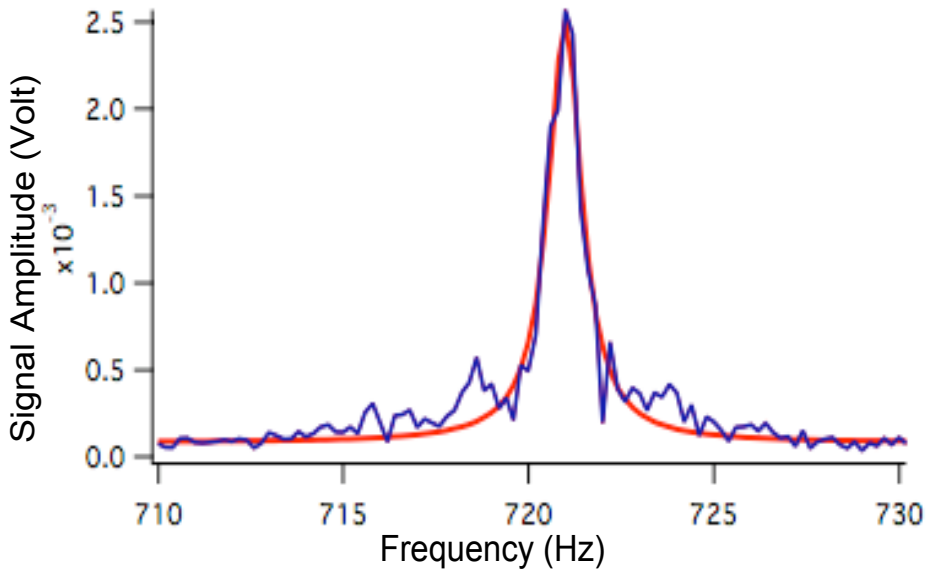

Figure 3.6: Frequency scan of a cantilever with a MgB_2 crystal. Blue line is the measured signal and red line is the best fit curve. From the Lorentzian fitting we get the resonance frequency 721 Hz and the quality factor about 450. Pressure inside the probe: less than 1 millitorr and frequency step size: 0.5 Hz.

by silver epoxy (H21D of Epoxy Technology). So if we apply a periodic voltage, that will induce periodic expansion of the piezo. This will impose a driving force on the cantilever at the frequency of the voltage. Due to cantilever vibration, the interference pattern also will change periodically and it will induce a periodic voltage signal. This signal is sent to the lock-in where it is averaged with a time constant τ_c. The cantilever shaking interval Δt is set to be 3 times τ_c to ensure the output of the lock-in is stable.

The equivalent noise bandwidth of the lock-in is $\Delta\nu = 1/4\tau_c$ when the normal 6 dB/octave filter is used. This means that the lock-in is effectively detecting all signals within the frequency range $f_0 - \Delta\nu$ to $f_0 + \Delta\nu$. After shaking the cantilever for Δt time, the program saves the lock-in outputs X and Y in the computer and

then increments the frequency of the signal generator and then repeats all of these steps. This is known as frequency scan.

After the frequency scan, the cantilever vibration amplitude is plotted for different frequencies. When the frequency of vibration is the same as the resonance frequency of the cantilever, the amplitude will be a maximum. So by fitting the amplitude versus frequency plot to a Lorentzian, we can determine the resonance frequency of the cantilever and this also gives a decent estimate of the quality factor, Q (Fig. 3.6). We have seen seen that Q increases as pressure drops. In fact in order to get a decent Q we need to keep the pressure of the probe at a level of few mTorr.

3.2.2 Determining the Cantilever Spring Constant

Another very important characteristic of the cantilever is its spring constant. While we don't need to know the exact spring constant of the cantilever to perform the NMRFM experiment, we must know the approximate value in order to calculate the signal-to-noise ratio. Without a decent signal-to-noise ratio, it is impossible to detect any signal without much signal averaging.

Direct measurement of the spring constant, κ_{osc}, is not easy for such micron size cantilevers. However, it is possible to determine κ_{osc} using the Equipartition Theorem, which is

$$\frac{1}{2}\kappa_{\text{osc}}\,\langle x^2\rangle = \frac{1}{2}\kappa_B\,T, \tag{3.4}$$

where $\langle x^2\rangle$ is the mean square noise vibration amplitude of the cantilever and T is temperature. But determining $\langle x^2\rangle$ is not that straightforward. It is defined as

$$\langle x^2\rangle = \int_0^\infty |G(f)|^2\,S_f\,df, \tag{3.5}$$

where $G(f)$ is the mechanical transfer function of the cantilever and S_f is the noise spectral density. The absolute square of mechanical transfer can be written as

$$|G(f)|^2 = \frac{f_{\rm osc}^4/\kappa_{\rm osc}^2}{(f_{\rm osc}^2 - f^2)^2 + (f_{\rm osc} f/Q)^2}, \tag{3.6}$$

and the noise spectral density is given by

$$S_f = \frac{4\kappa_{\rm osc}\,\kappa_B\,T}{2\pi f\,Q}. \tag{3.7}$$

The lock-in itself measures the RMS noise vibrations $\sqrt{|G(f)|^2\,S_f}$ with a bandwidth $\Delta\nu$. So selecting a very narrow lock-in bandwidth will allow us to reconstruct the shape of $\sqrt{|G(f)|^2\,S_f}$ by determining the RMS values for discrete frequencies in the spectrum.

In order to determine the RMS noise amplitude for a given frequency, a time series must be taken by digitizing the outputs of the lock-in for a given frequency. The RMS value of this time series will be the RMS noise amplitude for that frequency. When these RMS values are plotted for different frequencies, we get the RMS noise amplitude spectrum. The noise power spectrum (the integrand of Eq. 3.5) is calculated by squaring the RMS noise amplitude spectrum, and then dividing the result by the bandwidth of the lock-in amplifier. The resulting curve is then integrated over the frequency range to get the value for $\langle x^2 \rangle$. Now using Eq. 3.4 we can calculate $\kappa_{\rm osc}$. An example of RMS noise amplitude, power spectrum and corresponding integrated power spectrum of a cantilever at room temperature is shown in Fig. 3.7. It is also possible to write a LabVIEW program to do all of these steps automatically and find the cantilever spring constant. The cantilevers used in this experiment have spring constant of about 2.0×10^{-3} N/m.

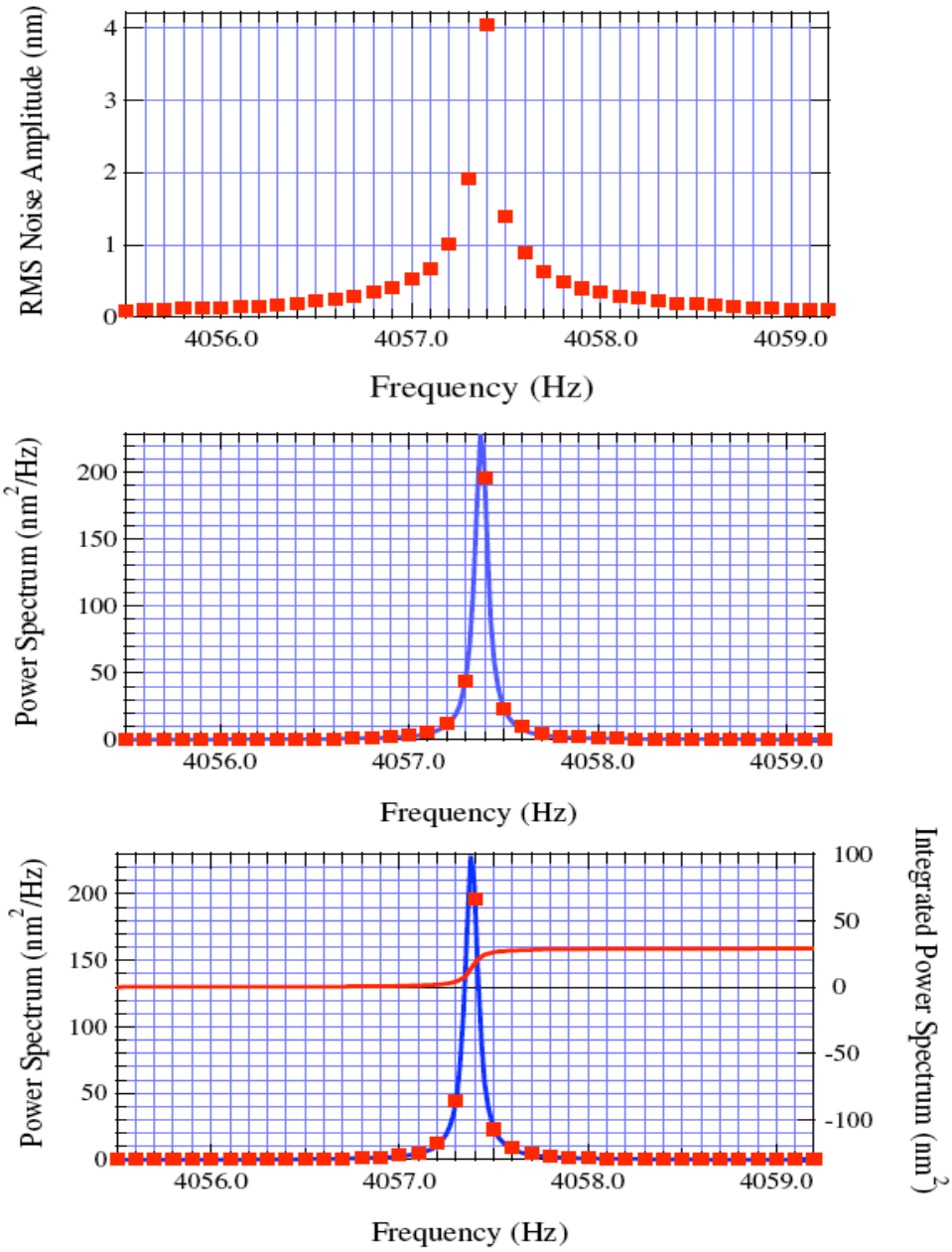

Figure 3.7: An example of RMS noise amplitude, power spectrum and corresponding integrated power spectrum of a cantilever at room temperature. The lock-in time constant is set at 3 second and the reference frequency increment step is 0.1 Hz between different time series [Mil03].

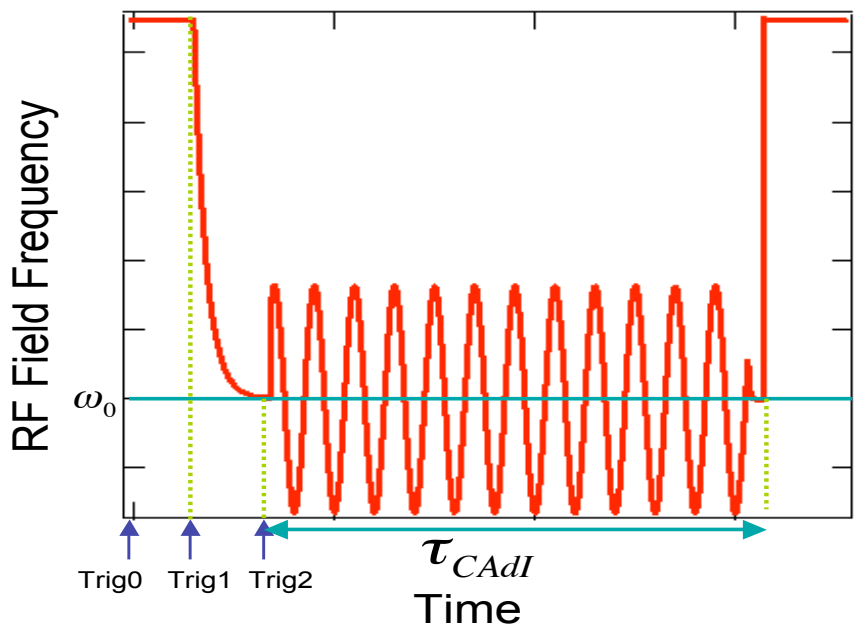

Figure 3.8: The RF frequency modulation scheme is shown here. τ_{CAdI} is the duration of Cyclic Adiabatic Inversion or frequency modulation.

3.3 NMRFM Experiment

NMRFM is a very complex experiment with several components. I have described the fringe lock system, fiber optic interferometer, RF coil, gradient producing magnet, cantilever, etc. Also, I have described how to oscillate the sample magnetization by modulating the RF field frequency. Now I will describe the RF field frequency modulation setup and related electronics. After that I will talk about the way we do the NMRFM experiment in our laboratory.

3.3.1 Frequency Modulation Setup

As we have discussed before, in order to create an oscillating magnetization, we need to modulate the RF frequency. However, we can not start modulating the RF

frequency instantaneously. If we do so, we will not be able to lock the spins around the effective magnetic field in the rotating frame. There are several ways to start the RF frequency modulation. The way I did that for my experiment is to start with an RF field frequency that is far from the resonance frequency ω_0, then exponentially approach the resonance frequency ω_0, and then start modulating the RF frequency. The RF frequency modulation amplitude is 50 kHz and its frequency is the resonance frequency of the cantilever. After a duration, the frequency modulation is stopped and RF frequency goes back to far off resonance value. This frequency modulation scheme is shown in Fig. 3.8. The electronics for achieving this is described in detail in Casey W. Miller's Ph.D. thesis [Mil03].

3.3.2 RF Power Amplifier

The output power from the RF signal generator is very low, usually order of few milliwatt. To achieve a value of H_1 (≥ 10 gauss) adequate for manipulating nuclear spins, we need to amplify the signal. This is done by an RF power amplifier. We use an ENI model 5100L-NMR RF power amplifier to amplify the RF signal by 50 dB. The output of this RF amplifier goes to the tank circuit, which contains the RF coil. The output impedance of the RF power amplifier is 50 Ω. That is why we also tune the impedance of tank circuit to 50 Ω. This will ensure maximum power transfer from the amplifier to the coil and we will get a large RF magnetic field.

To do the MgB_2 NMRFM experiment, it is very important that we get a large RF magnetic field for two reasons. First, the RF field must be larger than the local fields inside the sample. For solids dense with many nuclei, it is known that local fields are large, on the order of a few gauss. So the external RF field must

be greater than the local fields, or the RF field will not be able to modulate the spins. The second reason is that we have to satisfy the cyclic adiabatic inversion condition (Eq. 1.54). According to that condition, a sufficiently large RF magnetic field is needed to achieve adequate adiabatic following, and thus an adequate signal-to-noise ratio. For our desired $\Omega = 50$ kHz and a typical $f_{\rm osc} = 0.7$ kHz, the cyclic adiabatic inversion condition requires $(\gamma\, H_1)^2/(\Omega\, \omega_{\rm osc}) > 10$, which gives $H_1 > 14$ gauss. It is typically necessary to get at least 10 gauss or more RF field strength.

3.3.3 Signal-to-Noise Ratio Calculation

Before performing any experiment, it is necessary to calculate the theoretically expected signal-to-noise ratio of that experiment. It is wise to do the experiment only when we have a decent signal-to-noise ratio. For our experiment, we want to detect ^{11}B nuclei, with spin $S = 3/2$. The gyromagnetic ratio for ^{11}B is $\gamma/2\pi = 13.66$ MHz/T. Our magnetic field gradient is 200 T/m (based on the calculation given in Appendix A) and our chosen RF modulation amplitude is 50 kHz. Choosing $\Omega \sim 2\gamma H_1$ ensures that the magnetization is oscillated with nearly maximal amplitude. (See Fig. 1.13). Using Eq. 1.53, we get the resonance slice thickness of about 31 μm. However, our sample thickness is only about 10 microns. So that means the effective resonance slice thickness for our experiment is only 10 microns. Recall a typical MgB_2 single crystal area is about 40 microns by 40 microns.

Other experimental parameters are: total magnetic field $H_0 = 8.28$ tesla, MgB_2 density: 2.57 g/cm^3, molecular weight: 45.93 g/mole and natural abundance of ^{11}B nuclei: $\sim 81\%$. Parameters related to the cantilever are: $\kappa_{\rm osc} \approx 2 \times 10^{-3}$ N/m, $\Delta\nu = 2.5$ Hz, $Q \simeq 100$, $f_{\rm osc} = 740$ Hz.

From Eq. 1.51 we get that at temperature T, the magnetic force on the cantilever $F_{\text{mag}} = 5.6 \times 10^{-12}/T$ Newton. Also from Eq. 1.50 we get that at temperature T, the minimum detectable force by a cantilever is $F_{\text{min}} \approx 0.7 \times 10^{-15}\sqrt{T}$ Newton. Clearly the signal-to-noise ratio depends on temperature. At liquid nitrogen temperature, 77 K, the signal-to-noise ratio is $F_{\text{mag}}/F_{\text{min}} \sim 11$. We feel this was a sufficient theoretically expected signal-to-noise ratio to start the experiment. Actual signal-to-noise ratio is usually slightly less than this as there can be other sources of noise and errors.

3.4 Challenges of NMRFM Experiment

We had to overcome several challenges to perform the NMRFM experiment. One of the main challenges with this experiment is sample mounting. Since MgB_2 is a anisotropic sample, so we have to mount the sample very carefully. We have an 8 tesla magnet; so to measure the relaxation times in the superconducting state, our external magnetic field must be perpendicular to the c-axis of the MgB_2 single crystal. Unfortunately, our experimental setup requires that we mount such a sample vertically (on edge) on the cantilever. I have discussed some details of the sample mounting on the Section 3.1. We also have to be very careful during the sample mounting so that we don't accidentally break a cantilever. It requires a lot of practice and patience to mount a sample properly on a cantilever. We use a very stable XYZ movement stage to do that.

Other major issues with this probe are problems at low temperature. We have performed all our experiments at 77 K. And we have faced several challenges at that temperature. First of all is the alignment of the cantilever with the fiber. We align

those at room temperature. Then we cool down the probe to 77 K. However, due to differential contraction of different probe elements, very soon all this alignment is lost. In fact, many things may happen. Sometimes the fiber had destroyed the cantilever. Also the fiber may point in a different direction than at the cantilever. If that happens, we will not have any interference signal. In that case, and if our lateral movement could not re-attain alignment, we have to pull the probe out and realign the fiber-cantilever and go through all those steps again. It usually takes three to four tries to get correct fiber-cantilever alignment. Also in order to avoid fiber destroying the cantilever, we usually pull the fiber away from the cantilever during cool-down, and then advance it when cool.

Also we have seen that at low temperature, the gears get jammed. In order to avoid that I had to clean the gears very often and also made sure that all bolts are tight. Also when we place the probe inside the magnet, the large magnetic field pulls the probe towards itself. So that may also destroy the cantilever if the fiber points at it at that time. So in order to avoid that, I used to point the fiber at some other laterally displaced direction during this. Only when the probe is inside the magnet, I align the fiber with the cantilever.

Another problem is associated with the feedback piezo. The type of piezo that we have used in this probe works well only at room temperature. However, when we cool down the probe to 77 K, the plastic packaging of the piezo will harden and as a result, the piezo may not be able to expand/contract at low temperature. In fact, these piezos become unusable after few cooling-heating cycles. Although the ceramic piezo works at very low temperature, the pressure from plastic packaging makes those completely ineffective at low temperature. As far as I know, there is

only one German company which makes piezo that can be used at low temperature.

3.5 Results and Discussion

There are several ways to do an NMRFM experiment. In my experiment, I have fixed the resonance frequency ω_0 at 112.18 MHz. We also know that only those nuclei which are within the resonance slice will exert a force on the cantilever. The center of the resonance slice is at the point where total magnetic field is $H_{\text{tot}} = \omega_0/\gamma = 8.28$ tesla and the width of this slice is $2\Omega/\gamma\,\nabla H_z \approx 31$ microns. Due to the presence of the gradient field producing magnet (a 2.1 mm diameter, 20 mm long iron cylinder), the magnetic field is changing over distance. Since we have fixed the radio frequency, this also fixes the distance between the resonance slice and gradient field producing magnet, which is about 1.5 mm for this experiment (Fig. 3.1). This experiment was performed at 77 K.

Initially I placed the iron magnet far from the sample and then very slowly I decreased the distance. Our setup allows us to decrease the distance by about 3-micron steps. When the resonance slice does not penetrate the sample, the amplitude of cantilever vibration is small. The cantilever rings up to a frequency-independent value due to strong coupling of the modulated RF field with the cantilever; this "artifact" has an amplitude of about 1.9 nm in Fig. 3.9. Fluctuations about this baseline are due to thermal noise. However, when the resonance slice penetrates through the sample, the amplitude of cantilever vibration increases. As we decrease the sample-magnet distance further, the resonance slice will be out of the sample and the amplitude of cantilever vibration will again decrease to the artifact and thermal noise value. This is shown in Fig. 3.9. The "dips" of the amplitude

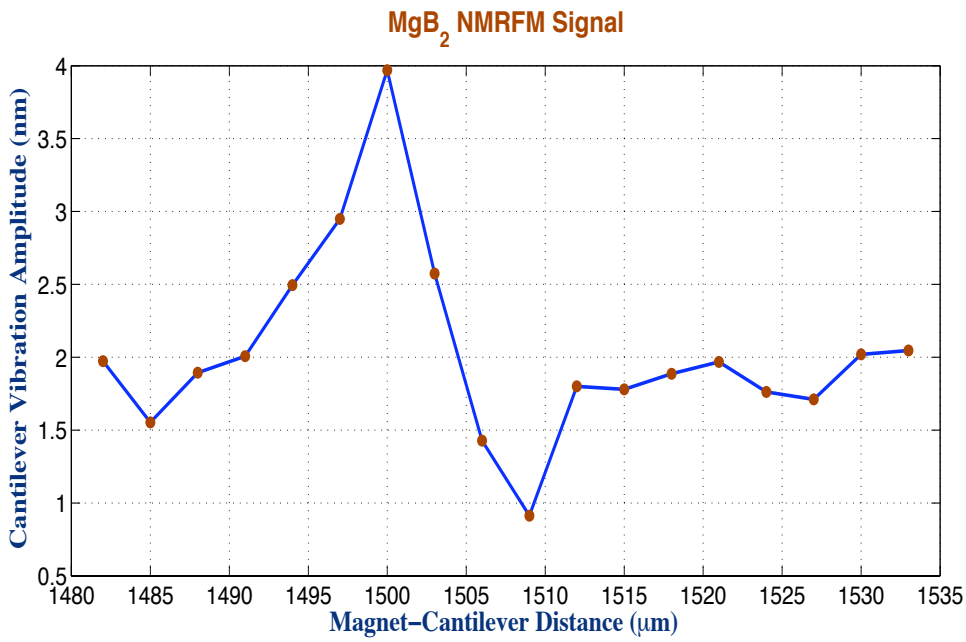

Figure 3.9: NMRFM signal of ^{11}B nuclei in MgB_2 sample.

on either side of the peak is probably due to the magnetic field fringing effects.

The amplitude of cantilever vibration induced by the nuclear magnetism is approximately 2.2 nm. This corresponds to a magnetic force of

$$F_{\text{mag}} = \frac{\kappa_{\text{osc}} \cdot x_{\text{mag}}}{Q} \approx \frac{2 \times 10^{-3}\ \text{N/m} \cdot 2.2 \times 10^{-9}\ \text{m}}{100} = 4.4 \times 10^{-14}\ \text{N}, \tag{3.8}$$

which is slightly smaller than the theoretically expected value (Eq. 1.51) of 0.7×10^{-13} N at 77 K. This theoretical overestimation may be due to several reasons. First, we don't know the exact size (both thickness and area) of the MgB_2 single crystal. Second, the cyclic adiabatic inversion condition (Eq. 1.54) is probably not properly satisfied. Third, we don't know the exact value of the magnetic field gradient. We also don't know the exact value of the cantilever spring constant.

Similarly the rms thermal noise motion is about 0.5 nm, corresponding to

$$F_{\text{noise}} = \frac{\kappa_{\text{osc}} \cdot x_{\text{noise}}}{Q} \approx 1.0 \times 10^{-14} \text{ N}, \tag{3.9}$$

again slightly larger than the theoretically estimated value (Eq. 1.50) of 0.6×10^{-14} N at 77 K. This theoretical underestimation is probably due to the approximate value of the cantilever spring constant used, $\sim 2 \times 10^{-3}$ N/m. So the experimentally determined signal-to-noise ratio for my NMRFM experiment is about 4.4, which is less than half of the theoretically estimated value (Eq. 1.52) of about 11 at 77 K.

3.6 Future Studies

This is the first force detected NMR signal of ^{11}B nuclei. I have demonstrated that it is possible to detect ^{11}B nuclei by NMRFM. Thus it is reasonable to undertake future NMRFM experiment on ^{11}B in MgB_2. In the future, we will study the spin-lattice relaxation rate anisotropy in both normal and superconducting states, the two-band effects on the relaxation process and the existence of any coherence peak (or two peaks?!!) in the superconducting state of a single crystal MgB_2 sample.

Chapter 4

Ti-sheathed Doped MgB_2 Superconducting Wires

Nothing shocks me. I'm a scientist.

– *Harrison Ford (1942 -)*, as Indiana Jones

The principle goal of this separate project is to study the superconducting properties of SiC doped Ti-sheathed MgB_2 wires. In contrast with the previously reported results that nano-SiC doping with a doping range below 16 wt% usually enhances the critical current density J_c, particularly at higher fields, our measurements show that SiC doping decreases J_c over almost the whole field range from 0 to 7.3 T at all temperatures. Furthermore, it is found that the degradation of J_c becomes stronger at higher SiC doping levels. Our results indicate that these negative effects on J_c could be attributed to the absence of significant effective pinning centres (mainly Mg_2Si) due to the high chemical stability of the crystalline-SiC

particles [LFL$^+$07]. Here I will give details of the sample preparation, experiments, and results. I also will discuss in detail the probable reasons for the observed results.

4.1 Introduction

Following the first report of Dou *et al.* on the dramatic enhancement of critical current density (J_c) in MgB_2 superconductors by nano-SiC doping, extensive studies have been carried out on nano-SiC-doped MgB_2 wires/tapes/pellets prepared with different SiC grain sizes (5300 nm), doping levels, sintering conditions and precursor powders [DSH$^+$02]. In particular, the dependence of J_c on the SiC doping level is an important issue and has been studied by a number of groups in the last few years. The initial study of Dou *et al.* on Fe-sheathed $MgB_2(SiC)_y$ samples, with y being the weight percentage of SiC and the size of SiC in the range between 10 and 100 nm, indicated that J_c increases dramatically with y increasing from 0 to 10 wt%. However, it is still unclear at what doping level and under what synthesizing/fabricating conditions (e.g. sintering temperature and time, etc.) SiC doping would optimize or degrade J_c.

Recently, Liang *et al.* have have successfully fabricated Ti-sheathed, undoped MgB_2 wires with high J_c and demonstrated that the performance of a Ti-sheath on J_c is comparable to or even better than an Fe-sheath [LFH$^+$06]. To further increase J_c for future applications of Ti-sheathed MgB_2 wires in lightweight superconducting magnets, we obtained from Liang Ti-sheathed MgB_2 wires doped with crystalline nano-SiC (20 nm) at different doping levels. We wanted to know if J_c in these wires could be enhanced substantially and the results obtained could help us further understand the dependence of J_c on the SiC doping level.

4.2 Experimental Details

Ti-sheathed, SiC-doped monocore MgB_2 wires were fabricated using the standard *in situ* powder-in-tube (PIT) method. The SiC powder was well mixed with the milled Mg + 2B mixture which has an average particle size of about 1 μm. The SiC powder with a nominal size of 20 nm was purchased from Alfa Aesar. The $MgB_2(SiC)_y$ wires were prepared with SiC doping levels at y = 5, 10 and 15 wt%. Wire sections about 6 inches long were cut from the as-drawn wires and sintered in a tube furnace in flowing high purity argon with the following schedule: the temperature was increased from room temperature to 800°C at a rate of 300°C h^{-1}, kept at 800°C for 30 min, and then cooled down to room temperature at a rate of 100°C h^{-1}. The cross-sectional areas of the wires were about 1 mm $\times$ 1 mm and the MgB_2 cores had cross-sectional areas of about 0.34 mm $\times$ 0.37 mm.

The size and shape of the commercial SiC particles were measured by transmission electron microscopy (TEM). The impurities, compositions and microstructures of the SiC-doped MgB_2 wires were studied by TEM, x-ray energy dispersive spectroscopy (EDS) and scanning electron microscopy (SEM). The temperature (T) dependent resistivity, $\rho(T)$, was measured by a standard four-probe dc technique. The temperature dependent magnetization, $M(T)$, was measured in both zero-field-cooled (ZFC) and field-cooled (FC) modes using a magnetic properties measurement system (MPMS) magnetometer from Quantum Design. Except for the 30 K hysteresis half-loop of the sample with y = 10 wt% SiC, which was measured using the MPMS, all of the other hysteresis loops were measured using a vibrating sample magnetometer (VSM) with a field ramping step of $\Delta H \approx 33$ Oe. In the $M(T)$ or $M(H)$ measurements, the longitudinal axis of each wire sample was oriented along

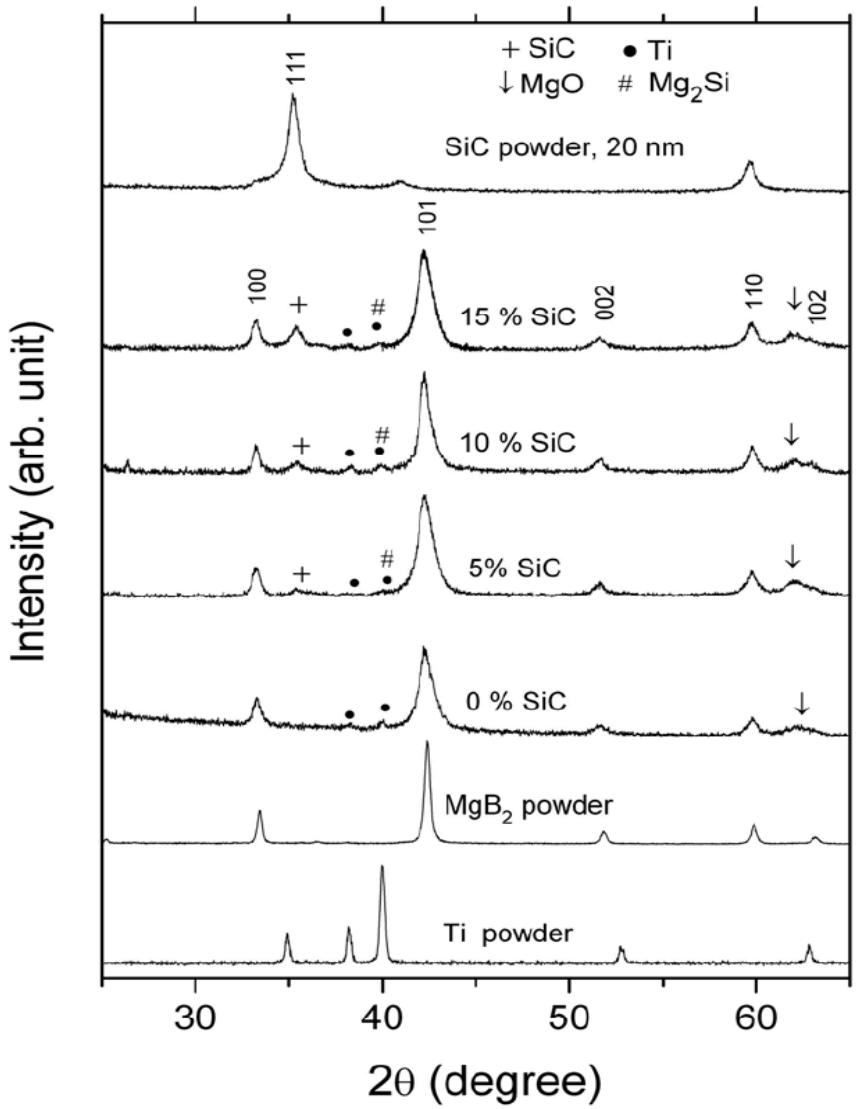

Figure 4.1: XRD patterns for the core materials of the Ti-sheathed, SiC doped MgB_2 wires. For comparison, XRD patters of three reference compounds, SiC powder, MgB_2 powder and Ti powder, are shown [LFL+07].

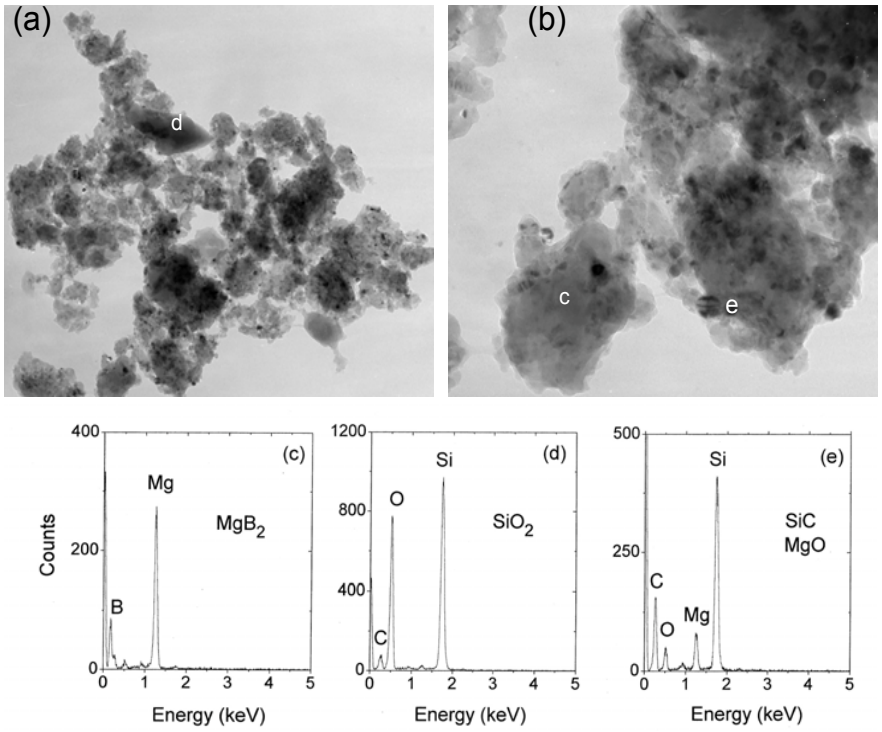

Figure 4.2: (a) TEM imag of the powder of the 20 nm SiC-doped MgB_2 core with a doping level of 10 wt%. (b) The magnified bottom portion of image in (a). (c)-(e) The EDS spectra taken sites of the sample [LFL$^+$07].

the direction of the applied magnetic field.

4.3 Results and Discussion

The average size of SiC particles was measured as 20.2 nm with a standard deviation of 9.7 nm. The X-ray diffraction (XRD) pattern shown in Fig. 4.1 indicates that these SiC nanoparticles are crystallized in the cubic β-SiC phase and lattice constant $a = 4.362(4)$ Å. Figure 4.1 shows the XRD patterns for the core material of the $MgB_2(SiC)_y$ wire samples, with the SiC doping level (in weight percentage of

MgB_2) $y = 0$, 0.05, 0.10 and 0.15. For comparison, the patterns of three reference compounds, SiC (20 nm), MgB_2 powder (-325 mesh) and Ti powder (-325 mesh), are also shown in Fig. 4.1. All of the patterns are normalized to the intensity of the strongest peak in each pattern. The major peaks for these wire samples can be indexed with the MgB_2 hexagonal structure, indicating that the core materials in these wires are primarily the MgB_2 phase. The SiC(111) peak located at $2\theta \approx 35.6°$ is seen in each pattern of the three SiC-doped samples but not in the undoped sample ($y = 0$) indicating that the SiC nanoparticles did not react completely with the other elements during the 30 min sintering at 800°C. However, our XRD data cannot determine definitely the existence of Mg_2Si impurities in the samples.

In Fig. 4.2, we show the TEM images and EDS spectra for the powder of the core material of the MgB_2 wire with 10 wt% SiC doping. Figure 4.2(a) shows an overview image in lower magnification, and its bottom part is magnified in Fig. 4.2(b). The large grains are identified mainly in the MgB_2 phase, as shown by the EDS analysis in Fig. 4.2(c). Some particles of irregular shape are identified as amorphous SiO_2; an example is marked in Fig. 4.2(a) and its EDS spectrum is shown in Fig. 4.2(d). Figure 4.2(b) shows that on the surface of MgB_2 grains there is a distribution of two kinds of particles: the larger ones (darker) with size 17.1±3.5 nm are SiC, and the well dispersed smaller particles with size less than 10 nm are MgO particles. Because these two kinds of particles are well dispersed, the EDS spectrum shows both MgO and SiC in Fig. 4.2(e). The EDS does not detect the existence of Mg_2Si particles, indicating that either Mg_2Si impurities were not formed in the SiC-doped samples during the sintering process or their concentration is too low to be detected. This EDS result is consistent with the XRD result discussed

above and can be explained by the slight reaction of SiC and the formation of SiO_2 which reduces the amount of Si available for forming Mg_2Si.

The above XRD/TEM/EDS results show some distinct differences between our SiC-doped MgB_2 samples and those of Dou *et al.* For our samples, the reaction between the doped SiC particles and Mg + 2B mixture is very slight, as seen by the small size change for the SiC particles before and after sintering, whereas for their samples, SiC reacted fully and no SiC peak was observed in the XRD patterns. For our samples, no indication of the formation of significant or detectable amounts of Mg_2Si nanoparticles was observed. For their samples, a prominent intensity of Mg_2Si peak was observed in the XRD patterns. Our TEM result shows that the SiC particles are mostly located on the surface boundaries of the MgB_2 grains, whereas their TEM results indicated that most of the SiC particles are embedded inside the MgB_2 grains.

Shown in Fig. 4.3 are the SEM images for the cores of the four wire samples. The surfaces of the samples were polished. These images show that large numbers of holes/voids exist in the samples. Most of them are about 12 μm in diameter which is close to the size of the Mg particles in the milled Mg + 2B powder precursor. These voids could be produced by the volume reduction in the Mg + 2B $\rightarrow$ MgB_2 reaction, it could also be partially attributed to the evaporation of the Mg particles during the sintering of the wires. It appears from the SEM images that the density of the holes/voids decreases with the increase in the doping level. For example, the hole density for the 15 wt% SiC sample shown in Fig. 4.3(d) is much less than that of the undoped sample shown in Fig. 4.3(a). In the process of mixing and packing the Mg, B and SiC powders, the spaces between the bigger Mg + 2B particles ($\sim$1 μm

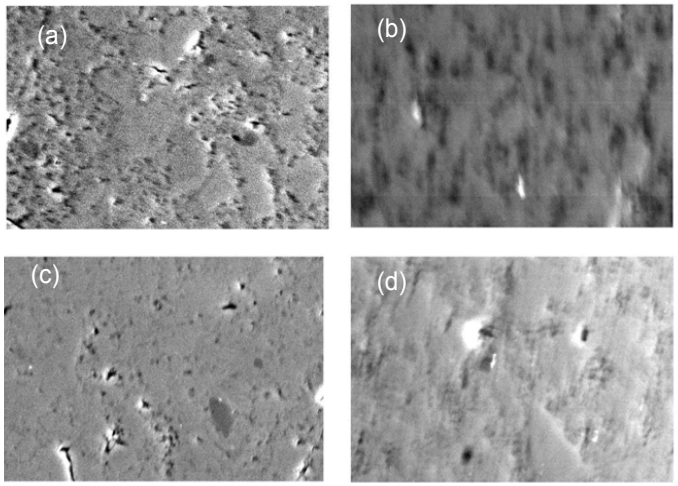

Figure 4.3: SEM images of the cores of the Ti-sheathed MgB_2 wires which are (a) undoped, (b) doped with 5 wt% SiC, (c) doped with 10 wt% SiC and (d) doped with 15 wt% SiC. The surfaces of the cores were polished before taking the images. These SEM images show that a large number of holes/voids exist in the cores of the wires [LFL+07].

in size) were filled by the much smaller SiC nanoparticles (20 nm average size), thus a higher doping level of SiC could result in a higher filling or packing factor.

Figure 4.4 shows the magnetic hysteresis loops obtained for the various samples at different temperatures. Figure 4.5 shows the field dependent magnetic $J_c(H)$ curves for the Ti-sheathed $MgB_2(SiC)_y$ wire samples. The rectangular cross sections of the MgB_2 wire cores are 0.34 mm $\times$ 0.37 mm = 0.126 mm^2 and the lengths of the wires range from 7.5 to 10 mm. The magnetic J_c of the samples was calculated with the formula $J_c = 20\,\Delta M/[a(1 - a/3b)]$ from the Bean critical state model, where ΔM is the difference between the upper and lower branches of the hysteresis loops (Fig. 4.4), $a = 0.34$ mm and $b = 0.37$ mm. Here we want to calculate the critical current density of MgB_2 wires and that is the reason for choosing those values for parameters a and b. Our field dependent magnetization measurement on the Ti-

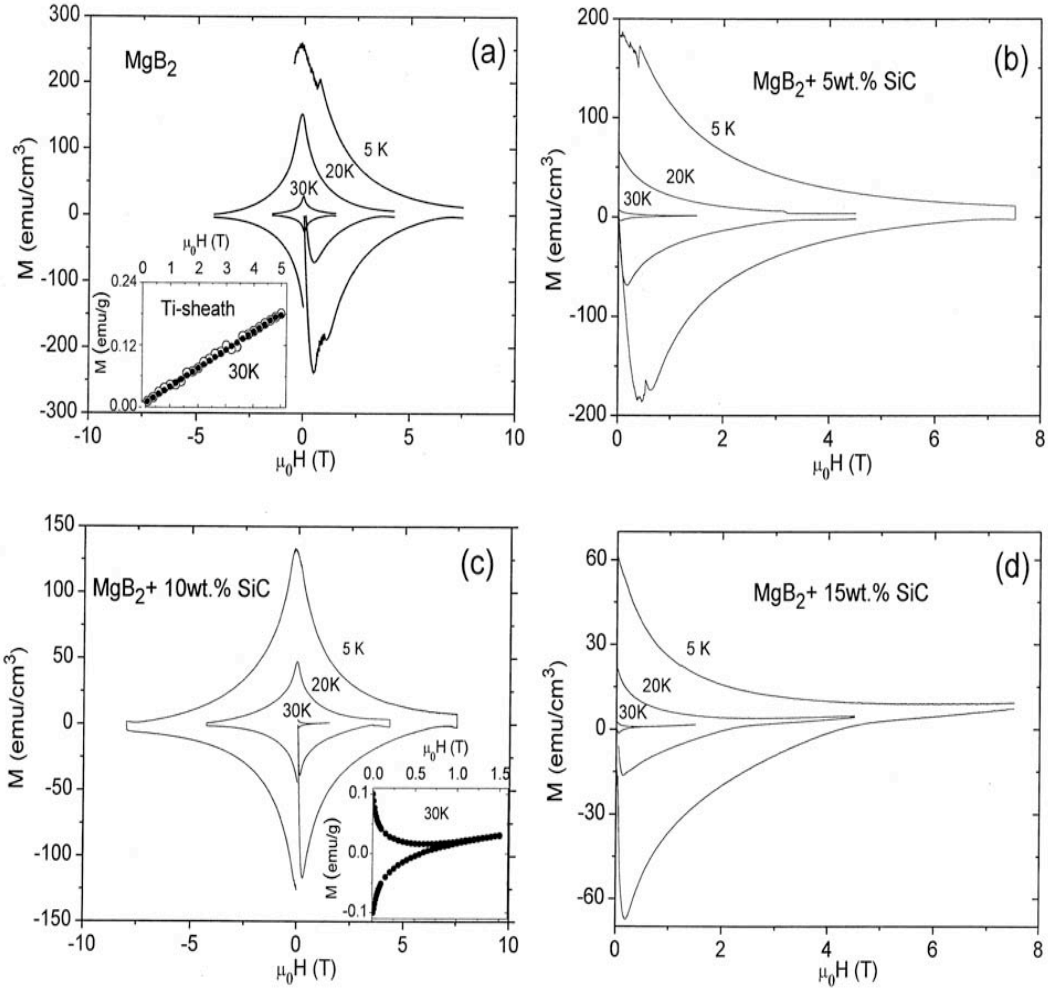

Figure 4.4: Hysteresis of undoped and doped MgB_2 wires, measured by a vibrating sample magnetometer. This data is used to calculate J_c using the Bean model. Inset of (c): this data only was taken using a SQUID magnetometer [LFL+07].

sheath of the wires indicates that the Ti-sheath is paramagnetic and reversible with field, and thus the magnetization background due to the Ti-sheath should make no contribution to the calculated J_c. The four J_c curves measured at 5 K (Fig. 4.5(a)) clearly show that SiC doping depresses J_c substantially in the whole field range from 0 to 7.5 T, and the effect of depression is stronger when the SiC doping level y is higher. At 15 wt% SiC, J_c is decreased to only 15%-25% of the value of the undoped ($y = 0$) sample. For example, the J_c at 2 T for the undoped sample is about 1.7 $\times 10^5$ A cm^{-2}; it decreases to only 2.5$\times 10^4$ A cm^{-2} at $y = 0.15$. There is no crossover between the J_c curve of the undoped and doped samples, indicating that SiC doping does not enhance J_c, not even in the high field region.

It is seen from the slopes of the J_c curves that for the samples with $y = 5$ and 10 wt%, the drop of J_c with increasing field is slower than that of the undoped sample. This is the only positive effect of SiC doping observed from Fig. 4.5. However, for the sample with y =15 wt%, the slope of the $J_c(H)$ curve is similar to that of the undoped sample, indicating that at this higher doping level SiC doping does not slow down the decrease in J_c. The J_c curves measured at 20 K (Fig. 4.5(b)) show similar effects of SiC doping to that shown by the 5 K J_c curves, except that the 20 K J_c curve of the $y = 5$ wt% sample has a crossover with the 20 K J_c curve of the $y = 0$ sample at about 3.8 T. For the J_c curves measured at 30 K (Fig. 4.5(c)), the variation of the slope indicates that at 30 K, the SiC doping actually causes the J_c to drop faster at higher SiC doping levels in the whole doping range of $0 \leq y \leq 15$ wt%.

Such a substantial depression of J_c in a wide range of fields and at all temperatures, caused by nano-SiC doping with doping level ranging from 0 to 15 wt% SiC, is in sharp contrast with earlier results that SiC doping in this range usually enhances

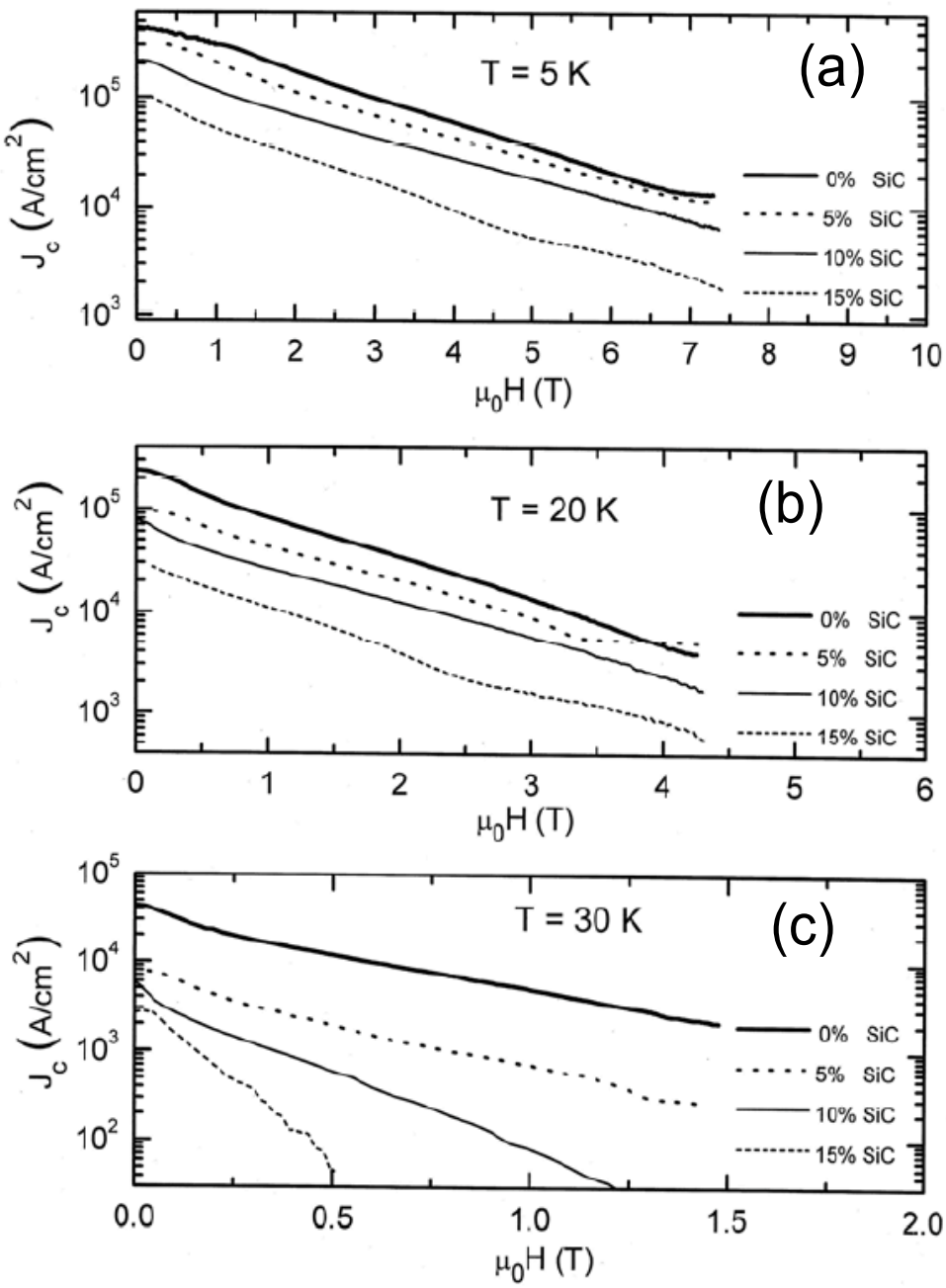

Figure 4.5: The field dependent magnetic J_c curves measured at temperatures of 5, 20 and 30 K for the undoped and SiC-doped MgB_2 wires [LFL$^+$07].

J_c, particularly in the high field region. Some researchers attributed such enhancement of J_c to the nano-SiC and Mg_2Si inclusions embedded inside MgB_2 grains and believed that these nano-inclusions function as effective pinning centres. If such an explanation is valid, then the observed negative effects of SiC doping on J_c for our samples could be explained by the absence of significant amounts of SiC and Mg_2Si nanoparticles distributed inside MgB_2 grains. For our samples, as discussed above for the XRD/TEM/EDS results, no detectable amount of Mg_2Si was formed due to the very slight reaction of the β-phase SiC nanoparticles with other elements, and the unreacted SiC nanoparticles are distributed mainly on the surface boundaries of the MgB_2 grains instead of being embedded inside the MgB_2 grains.

We believe that the suppression of J_c by SiC doping in our samples is a consequence of the competition between two opposite effects: on one hand, there could still be small amounts of very fine SiC and other formed impurities (possibly Mg_2Si) embedded inside the MgB_2 grains as effective pinning centres, which can enhance J_c. On the other hand, the majority of the unreacted SiC and the impurities (MgO and SiO_2) are distributed around the boundaries of the MgB_2 grains serving as weak links, resulting in the substantial decrease of J_c. Thus, more SiC nanoparticles located at the grain boundaries mean more degradation of J_c. This explains why J_c decreases with the increase of the SiC doping level. This explanation for the negative effect of SiC doping on J_c suggests that unlike the SiC nanoparticles located inside the MgB_2 grains, the SiC nanoparticles located at the grain boundaries of the MgB_2 grains may not act as effective pinning centres for enhancing J_c.

Figure 4.6 shows the dc magnetization $M(T)$ curves for the four samples, measured using a SQUID magnetometer at 20 Oe in both zero-field-cooled (ZFC)

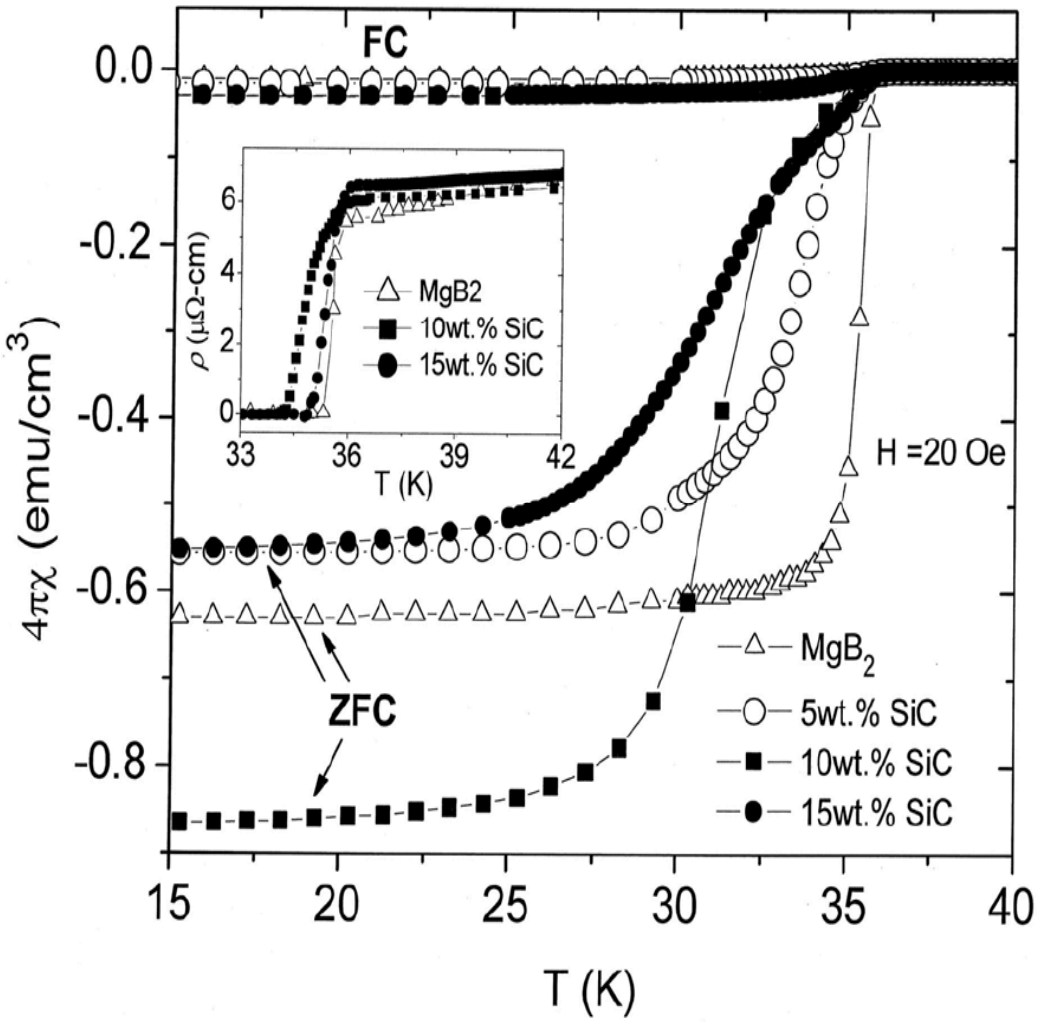

Figure 4.6: Temperature dependent dc magnetization, measured in both ZFC and FC modes in a field of 20 Oe and between 5 and 50 K, for the Ti-sheathed $MgB_2(SiC)_y$ wires. In the figure, only the sections of the curves in the temperature range between 15 and 40 K are shown. The inset shows the temperature dependent electrical resistivity curves in a temperature range between 33 and 42 K. The $T_{c,on}$ determined from these $\rho(T)$ curves is 35.9 K for all of three samples, which matches well with the values determined from the $M(T)$ curves [LFL+07].

and field-cooled (FC) modes. It is observed from the ZFC curves that the onset transition temperature, $T_{\mathrm{c,on}}$, defined as the temperature at which the susceptibility starts to drop, is ∼35.9 K. It is observed that the $T_{\mathrm{c,on}}$ is almost unchanged with the doping level y. In contrast, the midpoint transition temperature, $T_{\mathrm{c,mid}}$, defined as the temperature at the half drop of $M(T)$, decreases continuously with increasing y from 35.4 K at $y = 0$ to 30.8 K at $y = 15$ wt%. The width of the transition, ΔT, defined by the difference between the temperatures at 10% and 90% of the full drop of $M(T)$, increases continuously with increasing y from $\Delta T = 2.2$ K at $y = 0$ to $\Delta T = 9.8$ K at $y = 0.15$. The decrease of $T_{\mathrm{c,mid}}$ and increase of the width ΔT with increasing y were also observed by Dou *et al.* for their $MgB_2(SiC)_y$ samples. However, compared with their observed variations in $T_{\mathrm{c,mid}}$ and ΔT, which are about 1.7 and 1.03 K, respectively, with doping level up to $y = 0.2$, the changes in $T_{\mathrm{c,mid}}$ (≈ 4.6 K) and ΔT (≈7.6 K) for our samples with y up to 15 wt% are much larger. These large variations in $T_{\mathrm{c,mid}}$ and ΔT suggest that the co-substitution of B by both Si and C might not occur in our samples.

4.4 Conclusions

We have fabricated and characterized mono-core Ti-sheathed MgB_2 wires doped with crystalline SiC nanoparticles of average size 20 nm and concentrations up to 15 wt% SiC. The wires were sintered at 800°C for 30 min. In sharp contrast with the previously reported results that amorphous nano-SiC doping in this doping range usually enhances J_c, at least at higher fields, our measurements show that crystalline SiC doping decreases J_c in almost the whole field range from 0 to 7.3 T and at all temperatures. It is found that the degradation of J_c becomes stronger when the SiC

doping level is higher. Our XRD/TEM/EDS analysis indicates that the origins of these negative effects on J_c could be attributed to the absence of significant pinning centres (mainly very fine SiC and Mg_2Si particles) embedded inside the MgB_2 grains.

4.5 Future Studies

We are now studying the effects of sintering temperature and duration on these samples. We will study how critical current density changes with sintering temperature and also duration. We have already measured the hysteresis and magnetization of these samples and detail calculations are currently in progress.

Part II

Magnetic Measurements of Group IV Magnetic Semiconductor Alloys

Chapter 5

Group IV Magnetic Semiconductor Alloys

The most exciting phrase to hear in science, the one that heralds new discoveries, is not 'Eureka!' (I found it!) but 'That's funny ...'

– Isaac Asimov (1920 - 1992)

In this chapter I will talk about my research on group IV magnetic semiconductor alloys. First, I will give a very brief introduction to magnetic semiconductors. Magnetic semiconductors are materials which combine semiconductor properties with magnetism. One way to get such materials is to introduce magnetic moments into well known semiconductors. This new class of materials is known as dilute magnetic semiconductors [JSM$^+$06].

In the past 15 years, much pioneering research has been done on magnetic semiconductors. As a result of this huge international effort, we now have several group (III, V) compound semiconductors which become ferromagnetic after Mn doping. Dilute magnetic semiconductors such as (Ga,Mn)As and (In,Mn)As have transition temperatures well below room temperature. For example, the Curie temperature of (Ga,Mn)As is about 170 K. However, below the ferromagnetic transition temperature, these materials exhibit both magnetic and semiconducting properties. It is this property that creates the possibilities for many novel technologies, including spintronics, current induced magnetization reversal, quantum computation, etc.

5.1 Basic Introduction to Magnetic Semiconductors

Here, I will briefly describe the origin of ferromagnetism in (Ga,Mn)As. A (Ga,Mn)As epitaxial layer is grown by nonequilibrium, low-temperature Molecular Beam Epitaxy (MBE); it contains about 1% Mn. When it was first reported in 1992, the critical temperature was only 7.5 K. However, through careful MBE growth, annealing, etc., the Curie temperature has increased to about 170 K. However, it is still far below room temperature.

The crystal structure of (Ga,Mn)As shows (Fig. 5.1) two types of Mn atom sites in the GaAs lattice. Some Mn atoms substitute at Ga sites, these are called substitutional Mn atoms. Each substitutional Mn site (Mn_{Ga}) has a total of five unpaired electrons. Because orbital angular momentum is quenched by the crystal field, each Mn_{Ga} site has a total angular momentum of $S = 5/2$ [Kit04]. These substitutional Mn atoms also act as a moderately shallow acceptor. The other Mn impurities are at interstitial Mn sites, called Mn_I sites. Calculations have confirmed

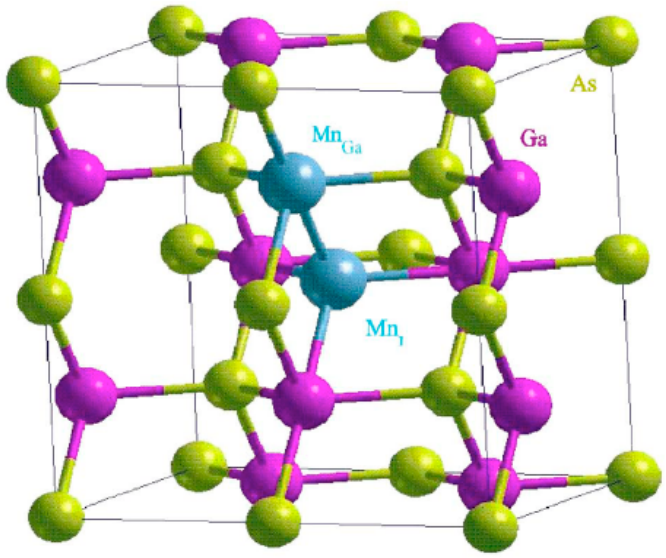

Figure 5.1: (Ga,Mn)As crystal structure: substitutional Mn_{Ga} and interstitial Mn_I in GaAs lattice [JSM+06].

that Mn_I acts as a double donor, as expected for a divalent metal atom occupying an interstitial site. Each Mn_I therefore compensates for two substitutional Mn acceptors. It is also likely that due to strong Coulombic attraction between positively charged Mn_I and negatively charged Mn_{Ga} defects, that these two defect sites pair up, as shown in Fig. 5.1. The total spin of the Mn_{Ga}–Mn_I pair is much less than the local spin 5/2 of an isolated Mn_{Ga} acceptor. This is known as the short range antiferromagnetic interaction between two defect sites and has been confirmed experimentally [EFJ+05].

Ferromagnetism in (Ga,Mn)As is observed when the Mn concentration reaches about 1%. At this large concentration, the localization length of Mn_{Ga} band states extend to a degree that allows them to mediate the ferromagnetic exchange interaction between them. At even higher Mn concentrations, the impurity states become

delocalized as the impurity band merges with the valance band. At this level, the interaction between local Mn atoms is mediated by the $p-d$ kinetic exchange mechanism. The crossover from the first to second type of interaction is controlled not only by the Mn density but also by the carrier density [JSM+06].

The term "ferromagnetic semiconductor" is used for materials where coupling between local moments is mediated by carriers in the valence or conduction band of the host semiconductor. Since the magnetic interaction is carrier mediated, it can be controlled by a number of different techniques: gate voltage, doping, photodoping, band-structure engineering, etc. This property of magnetic semiconductors makes them very interesting subjects to study.

5.2 Group IV Magnetic Semiconductors and Alloys

The main challenge with (III,Mn)V dilute magnetic semiconductors is that the Curie temperature is still very low, well below room temperature. One way to improve the Curie temperature is to increase the Mn dopant concentration. It has been predicted theoretically that to reach room temperature with (Ga,Mn)As about 10% Mn dopant in the GaAs lattice is needed. However, it is not at all easy to incorporate that much Mn into the GaAs lattice. Another problem with large scale production of such materials is that all of these materials are grown by MBE, which is very low yield and also expensive. These epitaxial layers are also very fragile, which makes it very hard to do the next stage of processing (i.e. etching, creating gates, source-drain, etc.). Besides these problems, another issue is that they are not compatible with current semiconductor technologies.

One way to get a room temperature magnetic semiconductor may be to

dope group IV semiconductors to make them ferromagnetic. It has been predicted by a number of groups that Mn doped group IV semiconductors will have Curie temperatures above room temperature [MSN04, dSF04]. Recently three groups have reported above room temperature ferromagnetism in MBE grown $Ge_{1-x}Mn_x$ and Mn implanted bulk Ge and Si systems [POD+06, JBD+06, BAAS+05]. This opens up the possibility of other group IV magnetic semiconductors, especially the group IV semiconductor alloys, like SiGe and GeC. We are trying to make these two group IV semiconductor alloys magnetic by Mn ion implant. Already, there is the prediction, based on a theoretical study, that Mn implanted $Si_{1-x}Ge_x$ alloys are suitable candidates for spintronic applications [PAC+04].

One great advantage of group IV magnetic semiconductors is that their fabrication technique is totally compatible with modern microelectronics fabrication techniques. The group IV semiconductor alloys, such as SiGe and GeC add another dimension to the study of dilute magnetic semiconductors. We will have another control parameter to fine tune the properties of these magnetic semiconductors. This new parameter is the composition of alloys. Already, preliminary data shows that the composition of semiconductor alloys can influence magnetic properties in a noticeable way. Also, alloys are better materials to study the effects of strain in dilute magnetic semiconductors.

5.3 Experimental Details

Here I will give the details of sample preparation. 20 keV manganese (Mn) ions are implanted in three samples: bulk Ge and 250 nm and 20 nm thick epitaxial GeC layers. The bulk Ge sample is used a reference sample, so we can compare

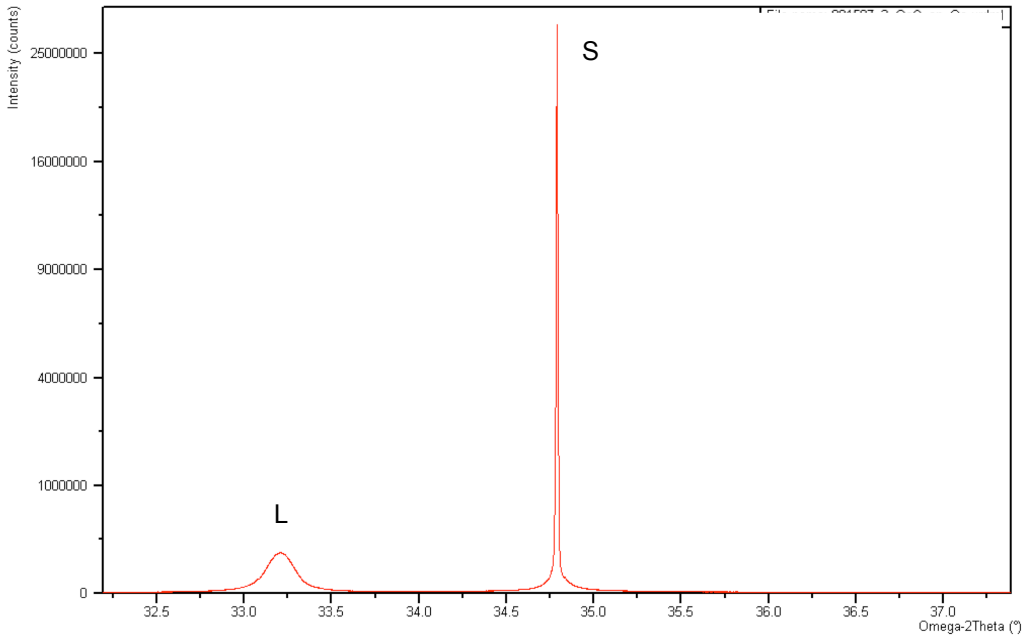

Figure 5.2: This is x-ray diffraction rocking curve of 200 nm GeC thin film, grown on Si (100) substrate. The S peak is from the substrate and the L peak is from the GeC layer. Source: Mustafa Jamil.

the magnetic properties of the GeC thin film samples. The GeC epitaxial layers are grown on Si(100) surfaces by ultra high vacuum chemical vapor deposition (UHV-CVD). The gas mixture is germane (GeH_4) and methylgermane (CH_3GeH_3). Before the epitaxial growth, the residual air pressure inside the chamber is maintained at about 10^{-9} Torr. This will greatly reduce the amount of contaminants in GeC films. During the sample growth, temperature and pressure are maintained at 450°C and 5 mTorr, respectively.

X-ray diffraction data shows a very good single crystalline phase of the GeC film (Fig. 5.2). The surface roughness of these films is about 0.5 nm, measured by an Atomic Force Microscope (AFM). These GeC thin films contain less than 1% carbon. However, the GeC film is grown on a Si(100) substrate. Due to lattice

mismatch between the Si substrate and the GeC film, there will be a compressive strain on the GeC film. While the 250 nm (thick) GeC film is completely relaxed, the 20 nm (thin) GeC film still has about 30% of its initial strain remaining. So, by implanting Mn ions in identical conditions in both of these GeC films, we can study the effects of strain on the magnetic properties of this material.

The Mn ion implant energy, dose and other conditions are identical for all the samples, so that we can compare the magnetic properties of different samples. The Mn ion implant energy is 20 keV and the dose is $1.1 \times 10^{16}/\text{cm}^2$. During the Mn ion implant all samples were kept at 300°C to avoid amorphization. For this relatively low energy ion implant, the Mn ion range is about 17 nm, with straggle in the distribution of about 9 nm. The peak Mn ion concentration is about $5 \times 10^{21}/\text{cm}^3$. If we assume that the only part of the film which contains the highest Mn ion concentration will become magnetic, then we have a very thin (less than 10 nm) magnetic layer for each film.

After the Mn ion implant, samples are cleaned ultrasonically using acetone, methanol and de-ionized water, respectively. This will clean off all magnetic and organic impurities from the samples. In the past, I have seen several "magnetic" signals. However, very careful experimentation has reveled that those are all coming from some magnetic impurities, most likely iron. It is also important to keep in mind that a diamond tipped iron needle is used to cut the silicon wafers into small pieces. So it is very likely that we may get some iron contamination with the semiconductor samples. Another thing that I have noticed that this iron contaminant "magnetic signal" does not vary that much with temperature over a range of 5 K to 300 K. This is not that surprising if we consider that iron has a very high Curie temperature

(about 1043 K) and as a result, iron contaminant magnetic moment will not change significantly over this temperature range. So we must clean the samples carefully before any SQUID measurement. After the cleaning I also made sure that I don't use any iron made objects (like tweezer, etc) to handle these samples. Only after the sample cleaning, a Superconducting Quantum Interferometer Device (SQUID) magnetometer is used to measured the magnetic properties of the samples. For each sample, field cooled and zero field cooled magnetizations at different applied magnetic fields are measured between 5 K and 300 K and magnetic hysteresis is measured at different temperatures [GJMB07].

Besides these three samples, there is a fourth sample: another 20 nm thin epitaxial GeC sample. The Mn ion implant conditions for this sample are identical to those for the other samples. However, in addition to Mn ions, we have also implanted boron (B) ions in this sample. The goal is to see the effects of co-doping in this type of magnetic semiconductor. If the magnetism in Mn implanted GeC is carrier mediated, then it will be greatly influenced by the carrier concentration. So, by co-doping this sample with a p-type dopant, we will increase the hole concentration and this in turn will influence the magnetic properties of Mn implanted GeC.

5.4 Experimental Results

The experimental results are discussed here. So far we have measured the magnetic properties of two samples: Mn implanted Ge and GeC (250 nm thick). The results are very encouraging so far. Fig. 5.3 shows the magnetization of these two samples at different temperatures. The external field is 1000 Gauss. The data clearly shows that magnetization per unit area for Mn implanted GeC is about 30% greater than

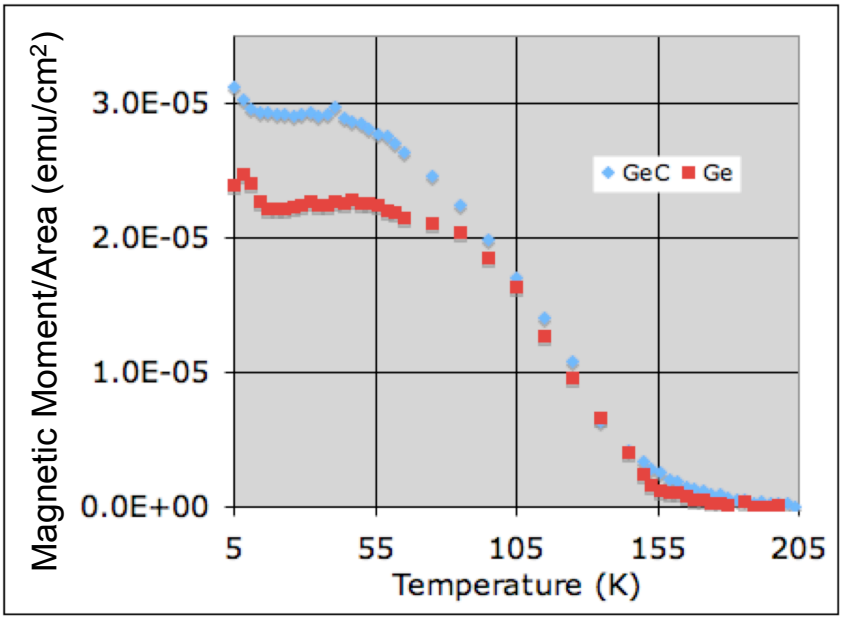

Figure 5.3: In plane saturated magnetization of Mn implanted Ge and GeC at different temperatures. Applied magnetic field is 1000 Gauss.

that of Mn implanted Ge. However, the Curie temperature for both of these samples are essentially the same, about 180 K.

In plane magnetic hysteresis loops at $T = 50$ K for Mn implanted Ge and GeC are shown in Fig. 5.4. Out-of plane magnetic hysteresis loops for the same samples are shown in Fig. 5.5. Both of these studies show that the magnetic field necessary to saturate magnetic moments in and out-of plane for Mn implanted GeC is greater than that for Mn implanted Ge. We also see clear hysteresis of Mn implanted GeC for the lower temperatures data (Fig. 5.6). This data exhibit hysteresis at three different temperatures. Clearly the hysteresis depends strongly on temperature.

Another informative set of data is the field-cooled and zero-field-cooled magnetic moment data for Mn implanted GeC (Fig. 5.7). To do this experiment, the

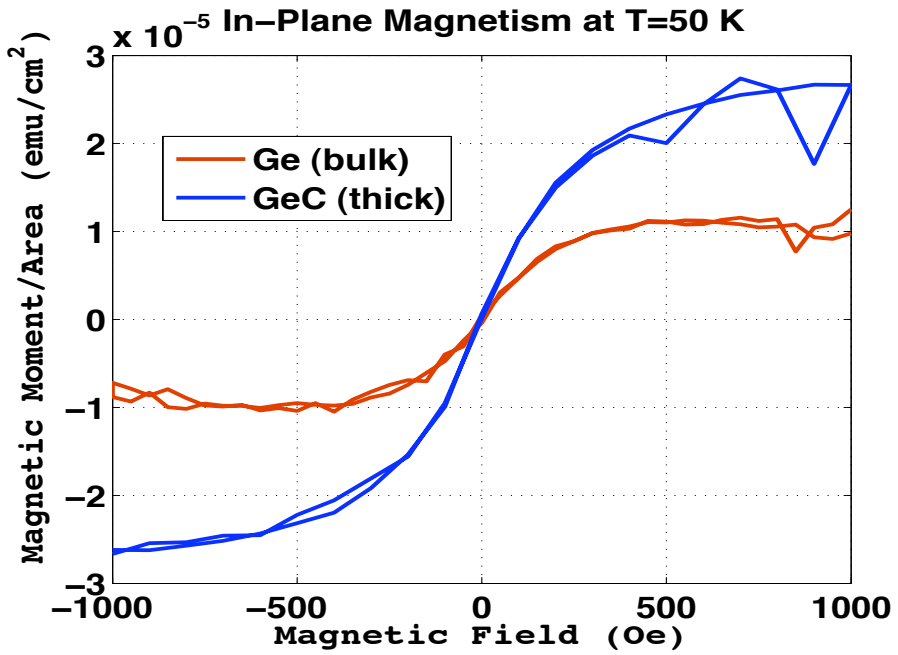

Figure 5.4: In plane magnetism of Mn implanted Ge and GeC (250 nm thick).

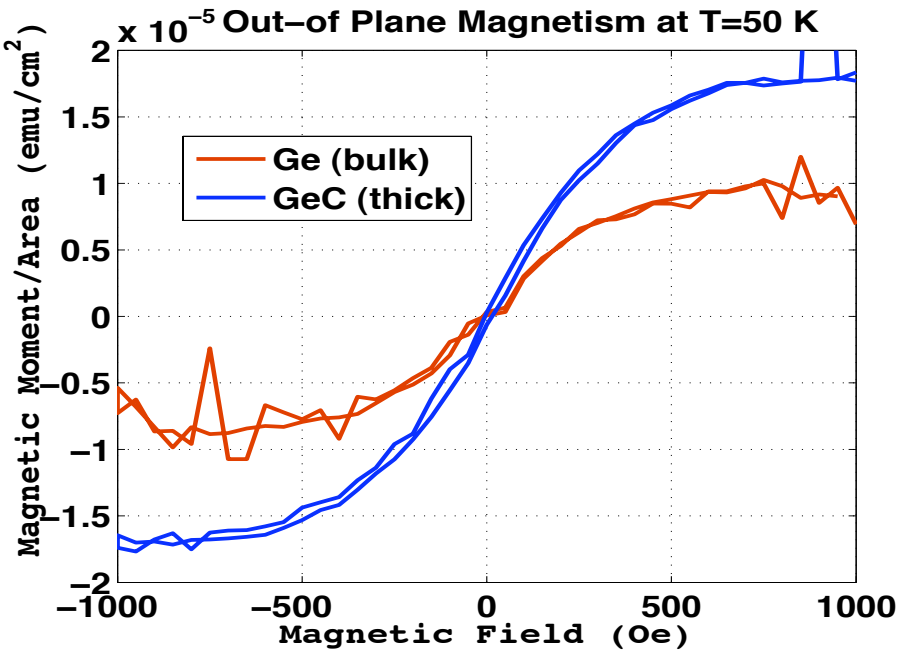

Figure 5.5: Out of plane magnetism of Mn implanted Ge and GeC (250 nm thick).

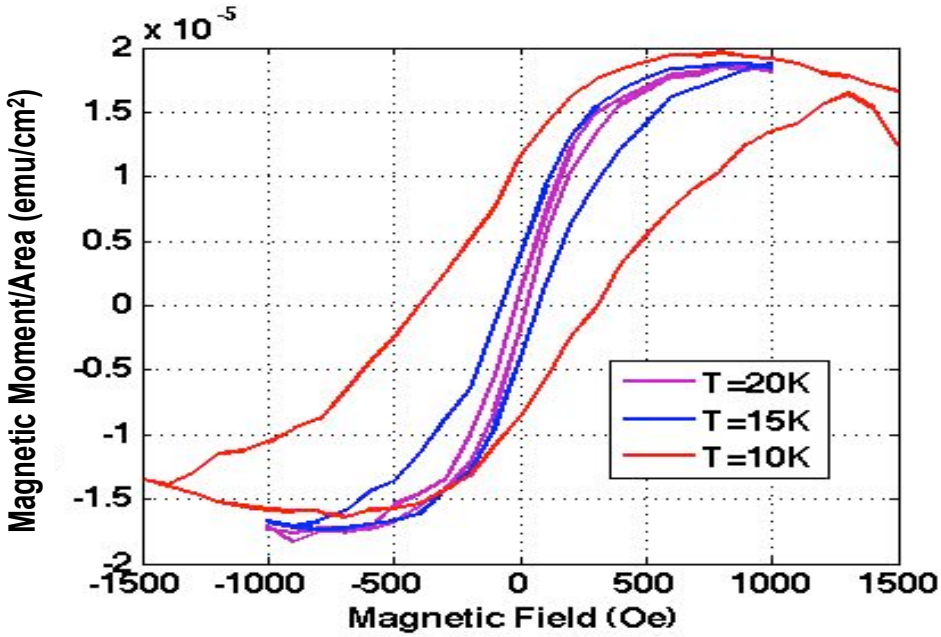

Figure 5.6: In plane hysteresis of Mn implanted GeC (250 nm thick) at different temperatures.

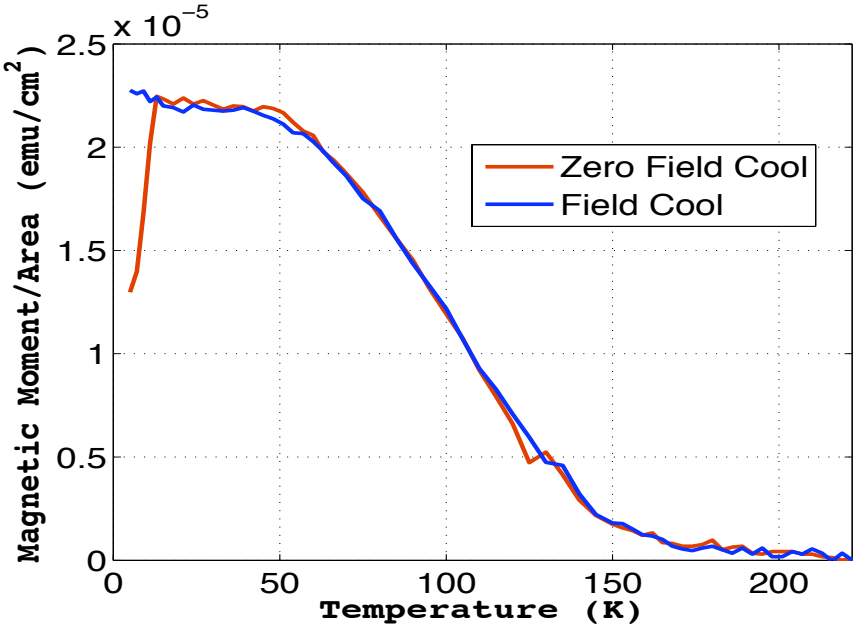

Figure 5.7: In plane field-cooled and zero-field-cooled magnetization for Mn implanted GeC (250 nm thick) in a 500 gauss magnetic field.

sample is first cooled down to 5 K without any magnetic field. After the temperature stabilizes, a 500 gauss magnetic is applied and the magnetic moment is measured for increasing temperatures up to 220 K. After the temperature reaches 220 K (which is above Curie temperature for this sample), the sample is gradually cooled down again in a 500 gauss applied magnetic field and magnetic moment is measured at different temperatures. This data clearly shows magnetic spin glass effects. The field-cooled data shows an ordinary increase of the magnetic moment with decreasing temperature. The zero-field-cooled data shows that the magnetic moment increases as temperature increases up to about 20 K. Above that temperature, the curve coincides with the field-cooled data curve, and then both magnetic moments decrease with increasing temperature.

5.5 Discussion

It is well known that high energy ion implants create defects. The field-cooled and zero-field-cooled data clearly show some magnetic spin glass effects. Based on this data, we can assume that for both of these samples there are magnetic atoms or clusters of atoms imbedded inside a non-magnetic substrate. When there is no applied field, the moments of the different atoms and clusters are aligned in random directions. So as we cool down the sample at zero field, the moments of different magnetic entities can be frozen along their different local random fields. As a result, the zero-field-cooled data shows a smaller magnetic moment than the field-cooled data at very low temperature. But, as we warm the sample, thermal excitation will help the moments to align along the applied magnetic field and so the magnetic moment will increase with temperature. Above 20 K, the thermal excitation is high

enough to destroy any spin freezing effects, and so both field-cooled and zero-field-cooled curves coincide. This also shows that the blocking temperature for these small magnetic clusters imbedded inside the semiconductor is about 20 K.

Another aspect of this type of magnetic semiconductor is that magnetic hysteresis depends strongly on temperature. Below the blocking temperature, we have a very strong hysteresis. But above the blocking temperature, the hysteresis is very weak. This also clearly shows the granular nature of this magnetic semiconductor. However, ferromagnetism persists well above the blocking temperature, even up to 180 K.

One way to make a more uniform magnetic semiconductor is to anneal these samples. We have done a high temperature rapid thermal anneal (550°C for 5 minutes) of these samples. After annealing, the spin glass effect almost disappears. However, the sample magnetization also decreases after annealing, mainly due to the fact that Mn atoms diffuse and disperse. As a result, the magnetization decreases, but the sample becomes more uniformly magnetic. The Curie temperature also increases after annealing. This clearly tells us that by proper Mn implant dose and annealing condition, we can get a more uniform magnetic semiconductor with higher Curie temperatures.

This is the first reported study of magnetism in Mn implanted GeC. This study clearly shows that addition of small amount of non-magnetic material (carbon here) can have very large impact on the magnetic properties of magnetic semiconductors. We have shown that Mn implanted GeC has higher magnetization than Mn implanted Ge for the same implant conditions. We think it may be due to the fact that inclusion of carbon induces compressive strain in the Ge lattice and hence

it changes magnetic properties. It also gives us another parameter to control the properties of magnetic semiconductors.

5.6 Future Studies

There are openings for many fundamental physics and technological studies on this type of system. So far, not much research has been done on granular magnetic semiconductors. In fact, most studies on granular magnetic materials are based on studies of the properties of iron nanoparticles implanted on SiO_2 substrate or similar types of systems. Here, we have a unique system where small magnetic nanoparticles are imbedded in the GeC substrate. Both the nanoparticles and substrate have a similar crystalline structure. As a result, despite the inhomogeneous nature of this material, extended band states of the semiconductor crystal couple strongly with the local magnetic moments, resulting in an enhanced magneto-optical and magneto-electronic response [Sam07]. Mn implanted GeC is a very good system to study magneto-transport and opto-electronic properties.

Besides these, not much research has been done to study effects of codoping on magnetic semiconductors. We need to study effects of both types of doping on the magnetic properties of this semiconductor. We also need to do X-ray magnetic circular dichroism (XMCD) experiments to study magnetic properties of this semiconductor. The XMCD study also will tell us how effective this semiconductor is going to be for device applications.

We also have prepared a Mn implanted SiGe sample and we will study its magnetic properties very soon. A theoretical calculation predicts ferromagnetism in the Mn implanted SiGe alloy. We hope to test this prediction very soon.

Appendix A

Program to Calculate 3D Magnetic Field Profile and Field Gradient

The following is the C language program that I wrote to calculate three-dimensional magnetic field and field gradient on the XZ plane, produced by a cylindrical magnetic tip. The z direction is along the cylinder axis. A little modification of this program will give only z component of magnetic field and magnetic field gradient along the z axis. The magnetic tip and its coordinates are shown in Fig. A.1. A typical result from this program, plotted by Matlab, is shown in Fig. 3.3.

The three different components of magnetic field at point (x, y, z) created by this cylindrical magnet of uniform magnetization $M\hat{z}$, radius r and height h is given

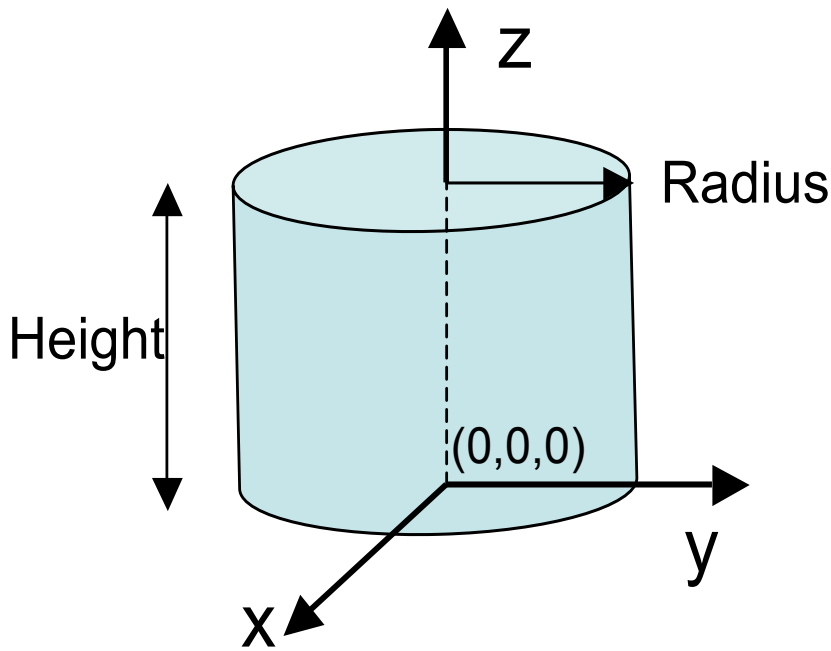

Figure A.1: The cylindrical magnetic tip and its coordinates.

below:

$$H_x = \frac{\mu_0 M r}{4\pi} \oint d\theta \ \cos\theta \left[\frac{(h-z) + \sqrt{\alpha(x,y,z,\theta)}}{\alpha(x,y,z,\theta) + (h-z)\sqrt{\alpha(x,y,z,\theta)}} + \frac{z - \sqrt{\beta(x,y,z,\theta)}}{\beta(x,y,z,\theta) - z\sqrt{\beta(x,y,z,\theta)}} \right], \tag{A.1a}$$

$$H_y = \frac{\mu_0 M r}{4\pi} \oint d\theta \ \sin\theta \left[\frac{(h-z) + \sqrt{\alpha(x,y,z,\theta)}}{\alpha(x,y,z,\theta) + (h-z)\sqrt{\alpha(x,y,z,\theta)}} + \frac{z - \sqrt{\beta(x,y,z,\theta)}}{\beta(x,y,z,\theta) - z\sqrt{\beta(x,y,z,\theta)}} \right], \tag{A.1b}$$

$$H_z = \frac{\mu_0 M r}{4\pi} \oint d\theta \left[\frac{\gamma(x,y,\theta)}{\alpha(x,y,z,\theta) + (h-z)\sqrt{\alpha(x,y,z,\theta)}} - \frac{\gamma(x,y,\theta)}{\beta(x,y,z,\theta) - z\sqrt{\beta(x,y,z,\theta)}} \right], \tag{A.1c}$$

where

$$\alpha(x,y,z,\theta) = (x - r\cos\theta)^2 + (y - r\sin\theta)^2 + (h-z)^2, \tag{A.2a}$$

$$\beta(x,y,z,\theta) = (x - r\cos\theta)^2 + (y - r\sin\theta)^2 + z^2, \tag{A.2b}$$

$$\text{and } \gamma(x,y,\theta) = x\ \cos\theta + y\ \sin\theta\ - r. \tag{A.2c}$$

Similarly, $\partial H_z/\partial z$ can be expressed as

$$\frac{\partial H_z}{\partial z} = \frac{\mu_0 M r}{4\pi} \oint d\theta\ \gamma(x,y,\theta) \left[\frac{\left[2(h-z)\sqrt{\alpha(x,y,z,\theta)} + \alpha(x,y,z,\theta) + (h-z)^2\right]}{\left[[\alpha(x,y,z,\theta)]^{5/4} + (h-z)\,[\alpha(x,y,z,\theta)]^{3/4}\right]^2} + \frac{2z\sqrt{\beta(x,y,z,\theta)} - \beta(x,y,z,\theta) - z^2}{\left[[\beta(x,y,z,\theta)]^{5/4} - z\,[\beta(x,y,z,\theta)]^{3/4}\right]^2} \right]. \tag{A.3}$$

This program is written to calculate these quantities. This program is written such a way that some minor modification of this program can calculate the field created by a magnet placed at some other point (x_t, y_t, z_t), instead of at the origin (as shown in Fig. A.1). Because of the cylindrical symmetry, I have plotted the magnetic field on the XZ plane only.

```
/* A PROGRAM TO DETERMINE THE B FIELD, ITS COMPONENETS AND THE
GRADIENT IN XZ PLANE */

#include<stdio.h>
#include<math.h>
#include<time.h>
```

```
#define HTIP      0.18      /* height of the mag tip, in micron */
#define MTIP      650000    /* magnetization of the tip magnet, SI unit */
#define RTIP      2.001     /* radius of the magnet tip, in micron */
#define B0        0         /* static uniform fixed magnetic field from outside */
#define LENGTH    10        /* XY plane length, in micron */
#define STEP      0.1       /* step size in the xy plane, in micron */
#define ZMAX      -3        /* distance in z direction, in micron */
#define ZMIN      -0.1      /* min distance in z direction, in micron */

void valueBBz(double x, double y, double z, double xt, double yt, double zt, double b0,
double rtip, double htip, double mtip, double *b, double *bz);

main()
{
double x, y, z, xt, yt, zt;
double B, Bxy, Byz, Bxz, Bz;
double min, max, diff;
FILE *fp1, *fp2;
time_t now, then;

now = time(NULL);
fp1 = fopen("./data/Bxz.dat", "a");
fp2 = fopen("./data/Bgz.dat", "a");

xt = 0;
```

```
yt = 0;
zt = 0;
y = 0;

min = -LENGTH/2;
max = LENGTH/2;

for (z = ZMIN; z >= ZMAX; z -= STEP) {
    for (x = min; x <= max; x += STEP) {
        Bxz = 0;
        Bz = 0;
        valueBBz(x, y, z, xt, yt, zt, B0, RTIP, HTIP, MTIP, &Bxz, &Bz);

        fprintf(fp1, "%e\t", Bxz);
        fprintf(fp2, "%e\t", Bz);
    }
    fprintf(fp1, "\n");
    fprintf(fp2, "\n");
}

fclose(fp1);
fclose(fp2);
then = time(NULL);
diff = difftime(then, now);
```

```
printf("\nTime taken is = %f\n", diff);
return 0;
}

/* Function to determine the B field */

void valueBBz(double x, double y, double z, double xt, double yt, double zt, double b0,
double rtip, double htip, double mtip, double *b, double *bz)
{
 double theta, thetastep, amp;                          /* integration variable */
 double x1, y1, z1, zh, xy, xyz1, xyz2, xyz3, xyz4, xyz;  /* intermediate variable */
 double b_x, b_y, b_z, gbz;                             /* mag field components and Bz */
thetastep = 0.001;
b_x = 0;
b_y = 0;
b_z = 0;
gbz = 0;

amp = rtip * mtip/10000000;          /* 10000000 is devided as it is part of mu_0 */
z1 = zt - z;
zh = zt + htip - z;

for (theta = 0; theta <= 6.285714286; theta += thetastep) {
    x1 = x - xt - rtip * cos(theta);
```

```
    y1 = y - yt - rtip * sin(theta);
    xyz1 = sqrt(x1 * x1 + y1 * y1 + zh * zh);
    xyz2 = sqrt(x1 * x1 + y1 * y1 + z1 * z1);
    xyz3 = xyz1 * xyz1 + zh * xyz1;
    xyz4 = xyz2 * xyz2 + z1 * xyz2;
    xy = x1 * cos(theta) + y1 * sin(theta);
    xyz = (zh + xyz1)/xyz3 - (z1 + xyz2)/xyz4;

    b_x += amp * cos(theta) * xyz * thetastep;
    b_y += amp * sin(theta) * xyz * thetastep;
    b_z += amp * (xy/xyz3 - xy/xyz4) * thetastep;

    gbz += amp * xy * ((xyz3 + zh * zh + zh * xyz1)/(xyz3 * xyz3 * xyz1) -
    (xyz4 + z1 * z1 + z1 * xyz2)/(xyz4 * xyz4 * xyz2)) * thetastep;
}

/*b = b_z; /* Select this if you want B_z only. */
*b = sqrt(b_x * b_x + b_y * b_y + (b_z + b0) * (b_z + b0)); /* Total mag field (B) */
*bz = gbz * 1000000; /* Bz; 1000000 is multiplied to make dimension correct */
return;
}
```

Appendix B

C Program to Simulate 2D Image of NH_3 Molecule

The following is the C language program to study the feasibility of imaging a planer NH_3 molecule using the Nuclear Magnetic Resonance Force Microscope. The magnetic field strength and gradient calculation part of the program is same as that of Appendix A. The calculated force amplitude profile is shown in Fig. B.1.

The time dependent force on the cantilever can be calculated by using Eq. 1.44, where the time dependent magnetization can be expressed as in Eq. 1.48. However, here M_0 is the magnetic moment of a proton. The force amplitude is the amplitude of the first Fourier harmonic of this time dependent force, calculated at the cantilever resonance frequency. The calculated data is plotted by the Matlab. Some minor modification of this program can calculate 3D force amplitude profile.

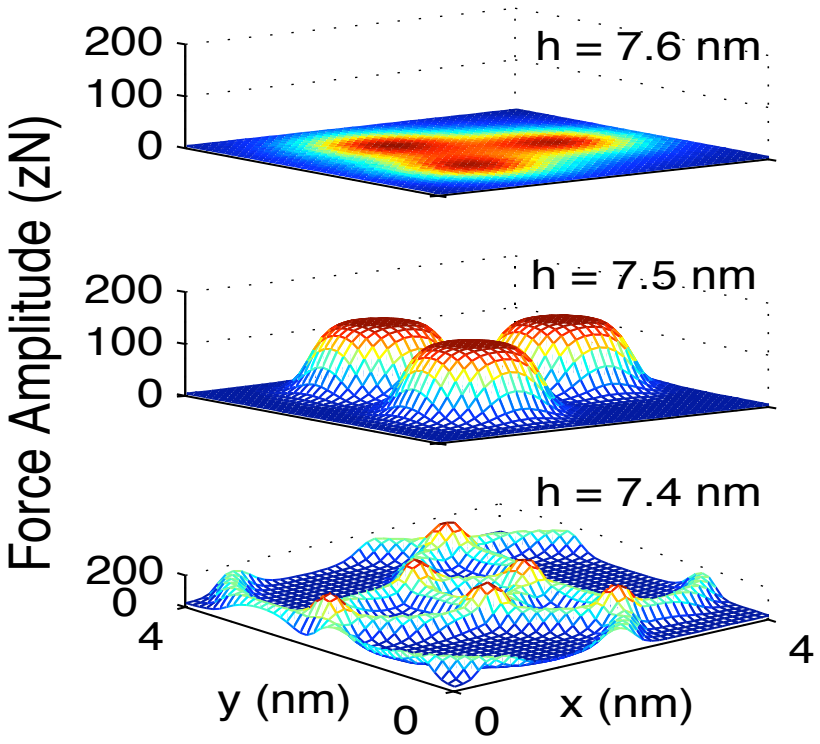

Figure B.1: The 2D force amplitude profile of a planer NH_3 molecule for three different sample-magnet distances. Here we are using a iron-tipped carbon nanotube as gradient-field-producing magnet. The force amplitude profile data is calculated by this program and then plotted by Matlab. Here I have assumed the magnet-on-cantilever NMRFM setup and we are scanning the cantilever to measure force amplitude at different points. It is also assumed that all three hydrogen atoms of NH_3 molecule lie on the same plane.

```
/* A PROGRAM TO SIMULATE 2D FORCE MAP FOR AN AMMONIA MOLECULE.
LENGTH SCALE NANOMETER */

#include<stdio.h>
#include<math.h>
#include<time.h>

#define LENGTH 2 /* Length of the sample space in the XY plane, in nano */
#define STEP 0.1 /* Step size in XY plane in x-y direction, in nano */

#define ZMAX 0.01 /* Thickness of the sample, in nano (bottom of the sample at z=0
plane) */
#define ZSTEP 1.0 /* Step size within the sample in z direction, in nano */

#define SCANL 4 /* Scan length in xy plane, in nano */
#define SCANS 0.1 /* Scan step size in all three direction, in nano */
#define SCANH 0.3 /* Scan length in z-direction, in nano (I probably do not need it
now.) */

#define ZTIP 7.6 / * Distance between the magnetic tip and the sample, in nano (about
the magnet diameter) */

#define FILEF "./data/2d21.dat" /* File where the force map will be saved */
#define FILEA "./ovar/2d21a.dat" /* File where the complex angle between real and
```

```
imag is saved */
#define FILER "./ovar/2d21r.dat" /* File where real part of force will be saved */
#define FILEI "./ovar/2d21i.dat" /* File where imag part of force will be saved */

#define OMEGA 348779020.9 /* RF frequency, Hz */
#define BRF 0.00025 /* Amplitude of the RF field, in Tesla */
#define OMEGAMOD 3100 /* Amplitude of RF Modulation, in frequency (Hz) */

#define B0 8.073 /* Magnetic field of the superconducting magnet, in Tesla */
#define MSAMP 1.4106 /* Magnetic moment of proton, SI unit (times 10^-26) */

#define RTIP 7.5 /* Radius of the magnet on the cantilever tip, in nano */
#define HTIP 100 /* Height of the magnet on the cantilever tip, in nano */
#define MTIP 650000 /* Magnetization of the magnet on cantilever (SI unit) */

#define FREQ 4017.5 /* Resonance frequency of the cantilever (Hz) */
#define TMAX 0.1 /* Maximum time of integration/ data taken, in sec */

double sample (double x, double y, double z, double length, double zmax, double msamp,
double step);
/* Define the sample distribution. Here 3D structure of single ammonia molecule. */

void firsthar(double b, double bz, double samp, double omega, double brf, double omeg-
amod, double freq, double tmax, double *prf, double *pif);
```

```
/* function to find out the real and imaginary amplitudes of first Fourier harmonic */

void valueBBz(double x, double y, double z, double xt, double yt, double zt, double b0,
double rtip, double htip, double mtip, double *b, double *bz);
/* function to find out the value of mag field (B) and its gradient (Bz) at any point */

main()
{
double xt, yt, zt, x, y, z; /* x,y,z are position of sample; xt,yt,zt are position of tip */
double lower, upper, B, Bz, ffh, mag, dV, scanlo, scanup;
double rforce, iforce; /* real & imaginary parts of the force */
char *fn1, *fn2, *fn3, *fn4; /* define the file name pointers */
FILE *fp1, *fp2, *fp3, *fp4; /* defines the file pointers */

zt = ZTIP; /* for this 2D experiment only */
fn1 = FILEF;
fn2 = FILEA;
fn3 = FILER;
fn4 = FILEI;

lower = -LENGTH/2;
upper = LENGTH/2 + STEP/10;
dV = STEP * STEP * ZSTEP; /* volume element within the sample */
```

```
scanlo = -SCANL/2;
scanup = SCANL/2 + SCANS/10;

fp1 = fopen(fn1, "a"); /* Opening the file to write the force map */

fp2 = fopen(fn2, "a"); /* one other file to write only force */
fprintf(fp2,"angle\n"); /* Writing the data column name into the file */

fp3 = fopen(fn3, "a"); /* file to record the real force */
fprintf(fp3,"real\n");

fp4 = fopen(fn4, "a"); /* file to record imag part of force */
fprintf(fp4,"imag\n");

/* main loop starts here */
for (yt = scanlo; yt <= scanup; yt += SCANS) {
    for (xt = scanlo; xt <= scanup; xt += SCANS) {
        rforce = iforce = 0;
        for (x = lower; x <= upper; x += STEP)
            for (y = lower; y <= upper; y += STEP)
                for (z = 0; z <= ZMAX; z += ZSTEP) {

                B = Bz = 0;
                mag = sample(x, y, z, LENGTH, ZMAX, MSAMP, STEP);
```

```
            /* find sample distribution from sample function */
            valueBBz(x, y, z, xt, yt, zt, B0, RTIP, HTIP, MTIP, &B, &Bz);
            /* finds B and Bz value from valueBBz */
            firsthar(B, Bz, mag, OMEGA, BRF, OMEGAMOD, FREQ, TMAX, &rforce,
            &iforce);
            /* find first Fourier harmonic amp of the force */
          }
          fprintf(fp1, "%e\t", sqrt(rforce * rforce + iforce * iforce) * dV);
          /* printing the data to the file */
          fprintf(fp2, "%e\t", atan(iforce/rforce)); /* print the angle to the file */
          fprintf(fp3, "%e\t", rforce * dV); /* print the real force to the file */
          fprintf(fp4, "%e\t", iforce * dV); /* print the imag force to the file */
        }
        fprintf(fp1, "\n");
        fprintf(fp2, "\n");
        fprintf(fp3, "\n");
        fprintf(fp4, "\n");
      }
      fclose(fp1);
      fclose(fp2);
      fclose(fp3);
      fclose(fp4);
      return 0;
}
```

/* function to find out the sample distribution */

```
double sample(double x, double y, double z, double length, double zmax, double msamp,
double step)
{
    double m1, mag, xp, yp, r;
    int m2, m;

    m2 = 0;
    r = 1; /* 0.0938101; Radius of circle on which all three protons lie, in nano. */

    if (z == 0) /* For 2D scan of ammonia. All three protons are in xy plane */
        m1 = msamp;
    else
        m1 = 0.0;

    if ((x < r) && ((x + step) > r) && ((y - step/10) < 0) && ((y + step/10) > 0))
        m2++;
    else if ((x< r * cos(44/21)) && ((x + step) > r * cos(44/21)) &&
            (y < r * sin(44/21)) && ((y+step) > r * sin(44/21)))
        m2++;
    else if ((x < r * cos(88/21)) && ((x + step) > r * cos(88/21)) &&
            (y< r * sin(88/21)) && ((y+step) > r * sin(88/21)))
```

```
        m2++;

    mag = m1 * m2;
    return mag;
}
```

/* Function to find out amplitude of the first Fourier harmonic (ffh) */

```
void firsthar(double b, double bz, double samp, double omega, double brf, double omegamod, double freq, double tmax, double *prf, double *pif)
{
    double dt, h1, h2, hr, hi, t, g;
    int p, pmax;

    dt = 1.0 / (16.0 * 22.0 * freq / 7.0);
    pmax = (int) (tmax/dt);
    hr = hi = 0.0;
    g = 42577000; /* gyromagnetic ration of the nucleus, proton here */

    for (p = 0; p ¡= pmax; p++) {
        t = p * dt;
        h1 = b - omega/g - 44.0 * omegamod * sin(44.0 * freq * t/ 7.0) / (7.0 * g);
        h2 = h1/sqrt(h1 * h1 + brf * brf);

        hr += h2 * cos(44.0 * freq * t / 7.0) * dt / tmax; /* real part of the ffh */
```

```
        hi += h2 * sin(-44.0 * freq * t / 7.0) * dt / tmax; /* imag part of the ffh */
    }
    *prf += hr * samp * bz; /* real part of the force amplitude */
    *pif += hi * samp * bz; /* imag part of the force amplitude */
    return;
}
```

/* Function to find out the value of the magnetic field (B) and field gradient (Bz) at a point */

```
void valueBBz(double x, double y, double z, double xt, double yt, double zt, double b0,
double rtip, double htip, double mtip, double *b, double *bz)
{
    double theta, thetastep, amp; /* integration variable */
    double x1, y1, z1, zh, xy, xyz1, xyz2, xyz3, xyz4; /* intermediate variable */
    double b_x, b_y, b_z, gbz; /* mag field components and Bz */

    thetastep = 0.01;
    b_x = b_y = b_z = gbz = 0;

    amp = rtip * mtip/10000000; /* 10^7 is devided as it is part of mu_0 */
    z1 = zt - z;
    zh = zt + htip - z;
```

```
    for (theta = 0; theta <= 6.285714286; theta += thetastep) {
        x1 = x - xt - rtip * cos(theta);
        y1 = y - yt - rtip * sin(theta);
        xyz1 = sqrt(x1 * x1 + y1 * y1 + zh * zh);
        xyz2 = sqrt(x1 * x1 + y1 * y1 + z1 * z1);
        xyz3 = xyz1 * xyz1 + zh * xyz1;
        xyz4 = xyz2 * xyz2 + z1 * xyz2;
        xy = x1 * cos(theta) + y1 * sin(theta);

        b_x += amp * cos(theta) * ((zh + xyz1)/xyz3 - (z1 + xyz2)/xyz4) * thetastep;
        b_y += amp * sin(theta) * ((zh + xyz1)/xyz3 - (z1 + xyz2)/xyz4) * thetastep;
        b_z += amp * (xy/xyz3 - xy/xyz4) * thetastep;

        gbz += amp * xy * ((xyz3 + zh * zh + zh * xyz1)/(xyz3 * xyz3 * xyz1) -
                (xyz4 + z1 * z1 + z1 * xyz2)/(xyz4 * xyz4 * xyz2)) * thetastep;
    }
    *b = sqrt(b_x * b_x + b_y * b_y + (b_z + b0) * (b_z + b0)); /* mag field (B) */
    *bz = gbz * pow(10,9); /* Bz; 10^9 multiplied to correct dimension (nm here) */
    return;
}
```

Bibliography

[AM01] Neil W. Ashcroft and N. David Mermin. *Solid State Physics*. Harcourt College Publishers, 2001.

[BAAS+05] M. Bolduc, C. Awo-Affouda, A. Stollenwerk, M. B. Huang, F. G. Ramos, G. Agnello, and V. P. LaBella. "Above room temperature ferromagnetism in Mn-ion implanted Si". *Physical Review B*, **71**:033302, 2005.

[Boh01] Arno Bohm. *Quantum Mechanics: Foundations and Applications*. Springer-Verlag, 2001.

[CC03] P. C. Canfield and G. W. Crabtree. "Magnesium Diboride: Better Late than Never". *Physics Today*, March:34, 2003.

[CMM+04] Jae-Hyuk Choi, Utkur M. Mirsaidov, Casey W. Miller, Yong J. Lee, Samaresh Guchhait, Michelle D. Chabot, Wei Lu, and John T. Markert. "Oscillator microfabrication, micromagnets, and magnetic resonance force microscopy". *Proceedings of SPIE*, **5389**:399, 2004.

[Dra01] Gergana Ilieva Drandova. *NMR Investigations in Copper-oxide Chain Compounds and High-T_c Superconductors*. PhD thesis, The University of Texas at Austin, 2001.

[dSF04] Antônio J. R. da Silva and A. Fazzio. "Stabilization of substitutional Mn in silicon-based semiconductors". *Physical Review B*, **70**:193205, 2004.

[DSH+02] S. X. Dou, S. Soltanian, J. Horvat, X. L. Wang, S. H. Zhou, M. Ionescu, and H. K. Liu. "Enhancement of the critical current density and flux pinning of MgB_2 superconductor by nanoparticle SiC doping". *Applied Physics Letters*, **81**:3419, 2002.

[EFJ+05] K. W. Edmonds, N. R. S. Farley, T. K. Johal, G. van der Laan, R. P. Campion, B. L. Gallagher, and C. T. Foxon. "Ferromagnetic moment and antiferromagnetic coupling in (Ga,Mn)As thin films". *Physical Review B*, **71**:064418, 2005.

[GJMB07] Samaresh Guchhait, Mustafa Jamil, John T. Markert, and Sanjay K. Banerjee. "Ferromagnetism in Mn-implanted Ge and epitaxial GeC". American Physics Society - Texas Section, October 2007.

[JBD+06] Matthieu Jamet, André Barski, Thibaut Devillers, Valier Poydenot, Romain Dujardin, Pascale Bayle-Guillemaud, Johan Rothman, Edith Bellet-Amalric, Alain Marty, Joël Cibert, Richard Mattana, and Serge Tatarenko. "High-Curie-temperature ferromagnetism in self-organized $Ge_{1-x}Mn_x$ nanocolumns". *Nature Materials*, **5**:653, 2006.

[JSM+06] T. Jungwirth, Jairo Sinova, J. Mašek, J. Kučera, and A. H. MacDonald. "Theory of ferromagnetic (III,Mn)V semiconductors". *Review of Modern Physics*, **78**:809, 2006.

[KIK+01] H. Kotegawa, K. Ishida, Y. Kitaoka, T. Muranaka, and J. Akimitsu. "Evidence for Strong-Coupling s-Wave Superconductivity in MgB_2: ^{11}B NMR Study". *Physical Review Letters*, **87**(12):127001, 2001.

[Kit04] Charles Kittel. *Inroduction to Soild State Physics.* John Wiley and Sons, Inc, 8th edition, 2004.

[LFH+06] G. Liang, H. Fang, M. Hanna, F. Yen, B. Lv, M. Alessandrini, S. Keith, C. Hoyt, Z. Tang, and K. Salama. "Development of Ti-sheathed MgB2 Wires with High Critical Current Density". *Superconductor Science and Technology*, **19**:1146, 2006.

[LFL+07] G. Liang, H. Fang, Z. P. Luo, C. Hoyt, F. Yen, S. Guchhait, B. Lv, and J. T. Markert. "Negative effects of crystalline-SiC doping on the critical current density in Ti-sheathed $MgB_2(SiC)_y$ superconducting wires". *Superconductor Science and Technology*, **20**:697, 2007.

[Mar00] Michael Marder. *Condensed Matter Physics.* John Wiley and Sons, Inc, 2000.

[Mil03] C. W. Miller. *Nuclear Magnetic Resonance Force Microscopy: Adiabaticity, External Field Effects, and Demonstration of Magnet-on-Oscillator Detection with Sub-Micron Resolution.* PhD thesis, The University of Texas at Austin, 2003.

[MM05] C. W. Miller and J. T. Markert. "Quantitative determination of the adiabatic condition using force-detected nuclear magnetic resonance". *Physical Review B*, **72**:224402, 2005.

[MSN04] Yoshio Miura, Masafumi Shirai, and Kazutaka Nagao. "First-principles design of ferromagnetic nanostructures based on group-IV semiconductors". *Journal of Physics: Condensed Matter*, **16**:S5735, 2004.

[NNM+01] Jun Nagamatsu, Norimasa Nakagawa, Takahiro Muranaka, Yuji Zenitani, and Jun Akimitsu. "Superconductivity at 39 K in magnesium diboride". *Nature*, **410**:63, 2001.

[PAC+04] S. Picozzi, F. Antoniella, A. Continenza, A. MoscaConte, A. Debernardi, and M. Peressi. "Stabilization of half metallicity in Mn-doped silicon upon Ge alloying". *Physical Review B*, **70**:165205, 2004.

[POD+06] M. Passacantando, L. Ottaviano, F. D'Orazio, F. Lucari, M. De Biase, G. Impellizzeri, and F. Priolo. "Growth of ferromagnetic nanoparticles in a diluted magnetic semiconductor obtained by Mn^+ implantation on Ge single crystals". *Physical Review B*, **73**:195207, 2006.

[Sak00] J. J. Sakurai. *Modern Quantum Mechanics*. Addison-Wesley, 2000.

[Sam07] Nitin Samarth. "Ruled by a magnetic-rich minority". *Nature Materials*, **6**:403, 2007.

[Sch68] Leonard I. Schiff. *Quantum Mechanics*. McGraw-Hill, Inc, 3rd edition, 1968.

[Sch70] Robert T. Schumacher. *Introduction to Magnetic Resonance.* W. A. Benjamin, Inc, 1970.

[Sid91] J. A. Sidles. "Noninductive detection of single-proton magnetic resonance". *Applied Physics Letters*, **58**:2854, 1991.

[Sli96] C. P. Slichter. *Principles of Magnetic Resonance.* Springer, 3rd edition, 1996.

[SRM+07] S. Strässle, J. Roos, M. Mali, H. Keller, and J. Karpinski. "^{11}B NMR study of single-crystal MgB_2 in the normal conducting phase". *Physica C*, **466**:168, 2007.

[Tin96] Michael Tinkham. *Introduction to Superconductivity.* Dover, 2nd edition, 1996.

Vita

Samaresh Guchhait was born in 1976 at Erashal, West Bengal, India. He is the eldest son of Kanan and Bidyut Guchhait. He has a younger sister and a younger brother. He completed his secondary education at Kandapasara D.P. High School and his higher secondary education at R.K.M. Vivekananda Centenary College, Rahara, West Bengal. Subsequently, he received his Bachelor of Science degree in physics with Honors from Presidency College, Kolkata (affiliated to the University of Calcutta). He then moved to Bangalore, India, where he completed his Master of Science degree in physics at the Indian Institute of Science. After spending his first twenty two idyllic years in India, he came to the USA for graduate studies. After a brief stint at the University of Oregon, Eugene as a graduate student, Samaresh moved to Austin, Texas and joined the University of Texas as a physics graduate student. Finally he receives his doctorate degree (Ph.D.) in 2007.

Permanent Address: Erashal, P.O. – Math Chandipur

PIN – 721 659, West Bengal, India.

This dissertation was typeset with LaTeX 2_ε[1] by the author.

[1] LaTeX 2_ε is an extension of LaTeX. LaTeX is a collection of macros for TeX. TeX is a trademark of the American Mathematical Society. The macros used in formatting this dissertation were written by Dinesh Das, Department of Computer Sciences, The University of Texas at Austin, and extended by Bert Kay and James A. Bednar.